Shock Compression of Molybdenum Single Crystals to High Stresses

Thesis by
Tomoyuki Oniyama

In Partial Fulfillment of the Requirements for the
Degree of
Doctor of Philosophy

CALIFORNIA INSTITUTE OF TECHNOLOGY
Pasadena, California

2020
Defended February 10, 2020

Tomoyuki Oniyama
ORCID: 0000-0001-6097-9917

ACKNOWLEDGEMENTS

First, I would like to express my sincere gratitude to my advisor, Prof. Guruswami (Ravi) Ravichandran. In every conversation we had about my research, classes, or careers, he gave me the energy to keep rolling with great advice. His insight, support, and smile were invaluable in completing my Ph.D.. Also, I would like to thank Prof. Yogendra Gupta at Institute for Shock Physics (ISP), Washington State University, who hosted me for more than 10 months. During the stay, he always helped me learn rigor in research and an ability to question. The time at ISP was and will be an asset for me. I greatly appreciate Prof. Kaushik Bhattacharya, Prof. Nadia Lapusta, and Prof. Dan Meiron for their willingness and commitment to serve in my committee.

I would also like to acknowledge the Theodore von Kármán Graduate Fellowship which generously supported my graduate studies in 2017 - 2018.

In the experimental campaign at ISP, I had a great help from members at ISP. First, I am sincerely grateful for all members for their understanding, and letting me have the priority in scheduling experiments. I would like to thank Dr. Michael Winey for useful discussions and help with the analysis of the experimental results. I would like to thank the engineering staff: Nate Arganbright for his help in material preparation including machining, Kurt Zimmerman for all of the training and his help in experimental design, and Yoshi Toyoda for his help in analysis and instrumentation. Also, I would like to thank all of the administrative staff, especially Sheila Heyns, Kate Barnes, Chelsea Jendro, and Mary Cody for organizing the travel plans and making ISP my "second home grad school." Lastly, I would like to thank fellow grad students: Dr. Prithachakaran Renganathan (Pritha), Travis Volz, and Jialong Ning for useful discussions and sharing time with me in Pullman.

At Caltech, I had the pleasure of working and learning together with members of the Ravi/Kaushik group. I was fortunate to have discussions with Prof. Laurent Stainier when he was visiting the group. I am thankful for his suggestions and insights for the numerical simulation which helped me at the very early stage. I would like to thank Dr. Zev Lovinger and Dr. Suraj Ravindran for their help in numerical modeling, their help in making my career choice, and the useful and useless discussions we had in Portland downtown. Also, I would like to thank Dr. Christian Kettenbeil for his help in making experimental plans, and our conversation on career path and for

being my "Senpai." Outside the group, I would like to thank fellow grad students: Joaquín García Suárez and Fabien Royer for their help in navigating through and installing Abaqus.

I would also like to thank all of the administrative staff at MCE, especially, Maria L. Cervantes for organizing meetings, and Donna Mojahedi for processing my complicated travel reports. Also, I would like to acknowledge Caltech ISP. My life at Caltech started with an unforgettable, fun time at the international orientation. I would like to thank, especially, Daniel Yoder and Laura Flower Kim for all the great memories at Caltech ISP.

My special thanks goes to Prof. Kenji Oguni at Keio University who recommended me to the opportunity of pursuing Ph.D. at Caltech. I am sincerely thankful for his insights and help which were invaluable for me in navigating my career.

To my Caltech friends: I am sincerely thankful for the journey we shared together, and I feel so blessed to have wonderful friends. We shared great moments in Gates Thomas, Joshua Tree, Chiapas, Sierra Bonita, San Francisco, Yellowstone, Sequoia, Big Bear, Sunnyvale, Naugatuck, Mammoth Lakes, and on the weight bench, and those became precious memories. You made my life at Caltech delightful and meaningful. Here's to our lifelong friendship!

To my close friends in Japan: I would like to extend my sincere gratitude to you. Whenever I visit Japan, I am so grateful that you kindly welcome me, and it is always my pleasure to see you doing well. After I decided to leave Japan for my Ph.D., the shape of our friendships evolved, but they never disappeared. Your stories of life have always been inspiring to me, and they will be for the entire life.

Lastly, most importantly, I would like to thank my family members for continuous support, love, and kindness, especially to my parents. For the past 27 years, your support was the key to every step I have taken.

ABSTRACT

To investigate the role of crystal anisotropy and the impact stress on the shock induced elastic-plastic deformation of BCC single crystals at high stresses, molybdenum single crystals were shock compressed along [100], [111], and [110] orientations. A series of plate impact experiments were conducted with various impact stresses (23 – 190 GPa) along each orientation. Along the [100] and [111] orientations, two-wave structure - an elastic shock wave trailed by a plastic shock wave - was observed to 110 GPa. Along the [110] orientation, the two-wave structure was observed only up to 90 GPa.

Based on the measured quantities, in-material quantities at the elastic limit and at the peak state were calculated. The elastic wave amplitudes were analyzed to determine the crystal anisotropy effects, the impact stress dependence, and the activated slip systems on the elastic limit. The elastic wave amplitude increased linearly with increasing impact stress, and that was significantly larger along the [111] orientation compared to the other orientations. The difference between calculated maximum resolved shear stresses at the elastic limit and corresponding Peierls stress suggested the activation of {110}<111> slip systems.

At the peak state, the Hugoniot relations were calculated along each orientation and compared with polycrystalline molybdenum Hugoniot relations. The Hugoniot relations along three orientations were in agreement within experimental uncertainties, even though the elastic limit showed considerable anisotropy. Also, they agreed reasonably well with the polycrystalline molybdenum data. This implied that the in-material quantities at the peak state do not depend on crystal orientation or the presence of grain boundaries.

In addition to the plate impact experiments, finite element simulations of shock compressed molybdenum single crystals were conducted using Abaqus Explicit in order to gain insight into deformation mechanisms activated during the elastic-plastic deformation. Shear strains on slip systems were explicitly considered by the crystal plasticity model implemented using Abaqus VUMAT subroutine. The results of FEM simulations indicated that {110}<111> systems were likely to be operating at the elastic limit. This observation was consistent with the experimental results from the present study.

PUBLISHED CONTENT AND CONTRIBUTIONS

[1] T. Oniyama, Y.M. Gupta, and G. Ravichandran. "Peak state in molybdenum single crystals shock compressed to high stresses." In: *To be submitted* (2020).
T.O. conducted experiments, analyzed experimental data, and wrote the manuscript.

[2] T. Oniyama, Y.M. Gupta, and G. Ravichandran. "Shock compression of molybdenum single crystals to 110 GPa: elastic-plastic deformation and crystal anisotropy." In: *To be submitted* (2020).
T.O. conducted experiments, analyzed experimental data, and wrote the manuscript.

TABLE OF CONTENTS

LIST OF ILLUSTRATIONS

LIST OF TABLES

Chapter 1

INTRODUCTION

Understanding material behavior under extreme conditions is important for many applications and scientific advances. Some examples of extreme conditions are high pressure, large strain rate, and high temperature, and materials encounter those conditions in many applications. Among the experimental techniques that can subject materials to high stresses, plate impact experiments provide a unique approach to investigate the compressed state of a material at well-characterized, high stresses (~100 GPa) subjected to high strain-rate loading. In a plate impact experiment, the center of the sample is subjected to uniaxial strain loading condition due to inertial confinement until the edge wave arrives. Thus, during a short duration of time, the strain in the material has only one non-zero component, which is beneficial for analysis of stresses. The strain-rate achievable by the plate impact experiment is on the order of $\sim 10^6$ s^{-1}, which cover the range of strain-rates that materials often encounter in engineering applications.

Experiments on single crystals are particularly beneficial for the following reasons: orientation of the loading direction and the slip systems are well-defined, and that permits shear stress calculations on relevant slip systems; and complications arising from wave reflections at grain boundaries are avoided. Because of these benefits, we chose to study single crystals to gain insight into the elastic-plastic deformation mechanisms under Mbar (100 GPa) shock stresses.

To date, shock wave experimental studies on single crystals have focused primarily on the elastic limit at low peak stresses. The anisotropy of the elastic limit was studied for molybdenum [1–3], tantalum [4], lithium fluoride [5–7], sodium chloride [8], magnesium [9, 10], beryllium [11], and copper [12] at impact stresses on the order of ~10 GPa. Specifically, for BCC single crystals, there have been no studies that have investigated the elastic-plastic deformation under shock compression to high stresses (Mbar stresses).

Besides the elastic limit, behavior at the peak state of single crystals under shock compression to high stresses is another area that has been minimally explored. The peak state due to shock compression has been mainly studied for polycrystalline materials. For example, the Los Alamos Shock Compendium [13] from the 1970s

reported Hugoniot relations at the peak state for a wide range of materials, but it did not include studies on single crystals. The peak state in shock compressed single crystal was studied for aluminum [14] and copper [15]. Both of those previous works subjected FCC single crystals to shock compression to ~ 70 GPa peak stresses. In contrast, for BCC single crystals, the peak state during the shock compression to high stresses has not been studied.

Thus, as we have seen above, there is a need to conduct studies at ~100 GPa impact stresses, to fully understand the role of anisotropy and high impact stress on the elastic limit in shock compressed BCC single crystals. Also, a series of experiments with varying impact stress can enable an understanding of the impact stress dependence.

1.1 Objective

The objectives of this study were to investigate the elastic-plastic deformation and the anisotropic response of BCC single crystals shock compressed to high stresses that were more than an order of magnitude larger than the elastic limit. Molybdenum (Mo) was chosen for this study, because it is a good representative of BCC metals and is available in the form of high-purity single crystals. Also, Mo is an important material for engineering applications due to its high resistance against heat and corrosion. Since those applications, especially in the area of aerospace engineering, involve extreme environments such as high pressure and high-rate deformation, understanding of the dynamic behavior is essential. In contrast to shock studies, its elastic-plastic deformation under (quasi-)static loading has been well studied [16–30]. The governing deformation mechanism was found to be dislocation slip on {110}<111> and/or {112}<111> systems [18–25, 27].

Regarding shock compression of Mo single crystals, prior studies provided comprehensive data at lower stress (~10 GPa) range [1–3]. The present work has covered stress range up to significantly high stresses (to 100 GPa and higher) and examined the stress dependence of the elastic limit and the peak state under high stresses. Thus, the present work has examined deformation issues not considered in the previous studies.

Specifically, the objectives of this study were the following:

- Investigate the elastic-plastic deformation of Mo single crystals shock compressed to high stresses. The stresses are significantly higher than the Hugo-

niot elastic limit of Mo, and on the order of 100 GPa and higher.

- Examine the effects of anisotropy and the impact stress on the elastic-plastic deformation of Mo single crystals for a broad range of impact stresses.
- Examine the role of deformation mechanisms at the elastic limit under high impact stress.
- Investigate the peak state, and examine the effect of anisotropy on the Hugoniot relations.
- Implement a crystal plasticity model into finite element method (FEM) scheme and conduct FEM simulations to gain insight into activated deformation mechanisms.

1.2 Approach

To achieve the overall objectives outlined above, a combination of experimental and numerical approaches was employed. For the experimental part, Mo single crystals were characterized by plate impact experiments. Mo single crystals were shock loaded along three crystal orientations: [100], [111], and [110]. Since pure longitudinal wave can exist along those three orientations in a cubic crystal [31], the Mo single crystals were subjected to uniaxial strain loading condition (1-D compression) in the experiments. The projectile velocities in the plate impact experiments were systematically varied to achieve approximately 23, 67, 90, 110, and 190 GPa impact stresses. The thickness of the sample was kept constant nominally at 2 mm for all of the experiments except two experiments along the [111] orientation which used thicker samples. Those two experiments along the [111] orientation were carried out in order to examine the decay of elastic wave amplitude with propagation distance, and the sample thickness was 3.5 mm. The experiments were conducted using a powder gun and a two-stage light gas gun at the Institute for Shock Physics, Washington State University.

In each experiment, particle velocity was measured on the back surface of the Mo single crystal using interferometry (VISAR [32, 33]). The elastic and plastic shock velocities were determined by the time difference of the arrival time on the front and back surface of a Mo single crystal. Based on the measured particle velocity and shock velocities, the in-material quantities at the elastic limit and the peak state were calculated using a method similar to impedance matching procedures and the Rankine-Hugoniot jump conditions used previously [1–3]. Also, maximum

resolved shear stresses (RSS) on slip planes were calculated following the approach used by Johnson *et al.* [31] to gain insight into the slip systems contributing to the deformation mechanisms.

For the numerical part, crystal plasticity model that explicitly accounts for crystallographic slip was implemented using VUMAT subroutine [34]. The FEM simulations were conducted using Abaqus Explicit [35] which was based on the explicit integration rule. The results of the FEM simulations provided insight into the activated deformation mechanisms during the shock compression of Mo single crystals.

1.3 Organization of This Thesis

The layout of the remaining chapters is as follows:

Chapter 2 provides background materials on the plate impact experiments and elastic-plastic deformation of Mo single crystals. This chapter also reviews the relevant shock studies on BCC single crystals, high stress studies on single crystals, and studies on polycrystalline Mo.

Chapter 3 describes the details of the plate impact experiments carried out at the Institute for Shock Physics, Washington State University. Methods used for the preparation of each target component and impactor, measurements under the ambient condition, construction of the target, and setup for laser interferometer (VISAR [32, 33]) are presented.

Chapter 4 presents the results of plate impact experiments in two parts. The first part presents the measured velocity profiles near the elastic limit, and the results for different impact stresses are compared. This part also shows the results for the experiments with thick samples. The second part presents the observation at the peak state, and compares the results between the three orientations.

Chapter 5 analyzes the experimental results presented in Chapter 4. In-material quantities at the elastic limit and the peak state are calculated. Based on elastic wave amplitude, the resolved shear stress (RSS) at the elastic limit on {110}<111> and {112}<111> slip systems are calculated. Based on the in-material quantities at the peak state, Hugoniot relations are calculated, and they are compared with the Hugoniot relations for polycrystalline Mo [36].

Chapter 6 describes the FEM simulation carried out in the present study. The crystal plasticity model implement in using Abaqus VUMAT subroutine [34] is described in detail. The results of the FEM simulation are compared with the experimental

results, and they are analyzed in terms of contributing deformation mechanisms.

Chapter 7 summarizes the findings of the present work, and outlines the directions for future work.

References

[1] A. Mandal and Y. M. Gupta. "Elastic-plastic deformation of molybdenum single crystals shocked along [100]." In: *Journal of Applied Physics* 121.4 (2017), p. 045903.

[2] A. Mandal and Y. M. Gupta. "Elastic-plastic deformation of molybdenum single crystals shocked to 12.5 GPa: Crystal anisotropy effects." In: *Journal of Applied Physics* 125.5 (2019), p. 055903.

[3] A. Mandal. "Elastic-Plastic Deformation of Molybdenum Single Crystals Shocked to 12.5 GPa." PhD thesis. Washington State University, School of Mechanical and Materials Engineering, 2016.

[4] G. Whiteman, S. Case, and J. C. F. Millett. "Planar shock compression of single crystal tantalum from 6-23 GPa." In: *Journal of Physics: Conference Series*. 500. 11. IOP Publishing. 2014, p. 112067.

[5] Y. M. Gupta. "Elastic compression to 30 kbar along <111> in shocked LiF." In: *Applied Physics Letters* 26.2 (1975), p. 38.

[6] Y. M. Gupta. "Effect of crystal orientation on dynamic strength of LiF." In: *Journal of Applied Physics* 48.12 (1977), p. 5067.

[7] J. R. Asay, G. R. Fowles, G. E. Durall, M. H. Miles, and R. F. Tinder. "Effects of point defects on elastic precursor decay in LiF." In: *Journal of Applied Physics* 43.5 (1972), p. 2132.

[8] W. J. Murri and G. D. Anderson. "Hugoniot Elastic Limit of Single-Crystal Sodium Chloride." In: *Journal of Applied Physics* 41.8 (1970), p. 3521.

[9] J. M. Winey, P. Renganathan, and Y. M. Gupta. "Shock wave compression and release of hexagonal-close-packed metal single crystals: Inelastic deformation of c-axis magnesium." In: *Journal of Applied Physics* 117.10 (2015), p. 105903.

[10] P. Renganathan, J. M. Winey, and Y. M. Gupta. "Shock compression and release of a-axis magnesium single crystals: Anisotropy and time dependent inelastic response." In: *Journal of Applied Physics* 121.3 (2017), p. 035901.

[11] L. E. Pope and J. N. Johnson. "Shock- wave compression of single- crystal beryllium." In: *Journal of Applied Physics* 46.2 (1975), p. 720.

[12] O. E. Jones and J. D. Mote. "Shock-Induced Dynamic Yielding in Copper Single Crystals." In: *Journal of Applied Physics* 40.12 (1969), p. 4920.

[13] S. P. Marsh. *LASL shock Hugoniot data.* Vol. 5. Univ. of California Press, 1980.

[14] D. Choudhuri and Y. M. Gupta. "Shock compression of aluminum single crystals to 70 GPa: Role of crystalline anisotropy." In: *Journal of Applied Physics* 114.15 (2013), p. 153504.

[15] R. Chau, J. Stölken, P. Asoka-Kumar, M. Kumar, and N. C. Holmes. "Shock Hugoniot of single crystal copper." In: *Journal of Applied Physics* 107.2 (2010), p. 023506.

[16] N. K. Chen, R. Maddin, and R. B. Pond. "Growth of molybdenum single crystals." In: *Journal of Metals* 3.6 (1951), p. 461.

[17] S. S. Lau and J. E. Dorn. "Interstitial impurity effects on the mechanical properties of molybdenum single crystals." In: *Scripta Metallurgica* 2 (1968), p. 335.

[18] N. K. Chen and R. Maddin. "Plasticity of molybdenum single crystals." In: *Journal of Metals* 3.10 (1951), p. 937.

[19] P. J. Sherwood, F. Guiu, H. C. Kim, and P. L. Pratt. "Plastic anisotropy of tantalum, niobium, and molybdenum." In: *Canadian Journal of Physics* 45.2 (1967), p. 1075.

[20] S. S. Lau, S. Ranji, A. K. Mukherjee, G. Thomas, and J. E. Dorn. "Dislocation mechanisms in single crystals of tantalum and molybdenum at low temperatures." In: *Acta Metallurgica* 15.2 (1967), p. 237.

[21] S. S. Lau and J. E. Dorn. "Asymmetric slip in Mo single crystals." In: *Physica Status Solidi (a)* 2.4 (1970), p. 825.

[22] G. J. Irwin, F. Guiu, and P. L. Pratt. "The influence of orientation on slip and strain hardening of molybdenum single crystals." In: *Physica Status Solidi (a)* 22.2 (1974), p. 685.

[23] D. Veselý. "The Study of Deformation of Thin Foils of Mo under the Electron Microscope." In: *Physica Status Solidi* 29 (1968), p. 675.

[24] D. Veselý. "The Study of Slip Bands on the Surface of Mo Single Crystals." In: *Physica Status Solidi* 29 (1968), p. 685.

[25] L. Hollang, D. Brunner, and A. Seeger. "Work hardening and flow stress of ultrapure molybdenum single crystals." In: *Materials Science and Engineering: A* 319 (2001), p. 233.

[26] A. Seeger. "The flow stress of high-purity refractory body-centred cubic metals and its modification by atomic defects." In: *Le Journal de Physique IV* 5.C7 (1995), pp. C7–45.

[27] A. Seeger and L. Hollang. "The flow-stress asymmetry of ultra-pure molybdenum single crystals." In: *Materials Transactions, JIM* 41.1 (2000), p. 141.

[28] C. R. Weinberger, B. L. Boyce, and C. C. Battaile. “Slip planes in bcc transition metals.” In: *International Materials Reviews* 58.5 (2013), p. 296.

[29] L. H. Yang, M. Tang, and J. A. Moriarty. “Dislocations and plasticity in bcc transition metals at high pressure.” In: *Dislocations in Solids* 16 (2010), p. 1.

[30] F. Guiu. “Slip asymmetry in molybdenum single crystals deformed in direct shear.” In: *Scripta Metallurgica* 3.7 (1969), p. 449.

[31] J. N. Johnson, O. E. Jones, and T. E. Michaels. “Dislocation Dynamics and Single-Crystal Constitutive Relations: Shock-Wave Propagation and Precursor Decay.” In: *Journal of Applied Physics* 41.6 (1970), p. 2330.

[32] L. M. Barker and R. E. Hollenbach. “Laser interferometer for measuring high velocities of any reflecting surface.” In: *Journal of Applied Physics* 43.11 (1972), p. 4669.

[33] L. M. Barker and K. W. Schuler. “Correction to the velocity-per-fringe relationship for the VISAR interferometer.” In: *Journal of Applied Physics* 45.8 (1974), p. 3692.

[34] Dassault Systemés. *Abaqus User Subroutines Reference Guide*. `http://ivt-abaqusdoc.ivt.ntnu.no:2080/v2016/books/sub/default.htm`. [Online; accessed 2019 December 14].

[35] Dassault Systemés. *Abaqus 2016 Documentation.* `ivt-abaqusdoc.ivt.ntnu.no:2080/v2016/`. [Online; accessed 2019 December 14].

[36] R. S. Hixson and J. N. Fritz. “Shock compression of tungsten and molybdenum.” In: *Journal of Applied Physics* 71.4 (1992), p. 1721.

Chapter 2

BACKGROUND

This chapter provides background for this study. Section 2.1 presents the theoretical background for the plate impact experiments and shock jump conditions that describe the relation between the states ahead and behind the shock wave. Section 2.2 provides the crystalline properties of Molybdenum (Mo). The crystal structure and the elastic properties are also summarized. Section 2.3 reviews past studies on the quasi-static deformation of Mo single crystals. Sections 2.4 - 2.6 review relevant past experimental studies on shock compression. Lastly, the motivation for this study is described in Section 2.7. The section also lists the specific research questions to be answered through this study.

2.1 Plate Impact Experiments

In this study, Mo single crystals were characterized experimentally using plate impact experiments. In a plate impact experiment, a plate is accelerated to desired velocity either by compressed air or explosive, and strikes against the target. This plate is referred to as an impactor. In a transmission type of experiment, a material of interest, which we refer to as sample, is initially at rest. When an impactor strikes the target which contains the sample, a plane wave is generated inside the target. Due to the inertial confinement, the region at the center of the sample is subjected to pure one dimensional compression (uniaxial strain condition) until waves generated at the outer edge of the sample arrive at the center. The response of the sample is measured during that time frame. In this work, laser interferometry (VISAR [1, 2]) was used to measure the velocity profile on the back surface of the sample. The well-characterized loading condition is beneficial in analyzing stress and density inside the sample. Because of that, since the 1950s, a wide range of materials have been characterized under shock compression using plate impact experiments [3]. Also, for studies on single crystals, it permits the calculation of the corresponding shear stresses on planes of interest inside sample at the elastic limit [4].

Shock jump conditions

In a plate impact experiment where shocks propagate into the sample, the differential forms of the governing equations are not well defined. Instead, the integral forms of

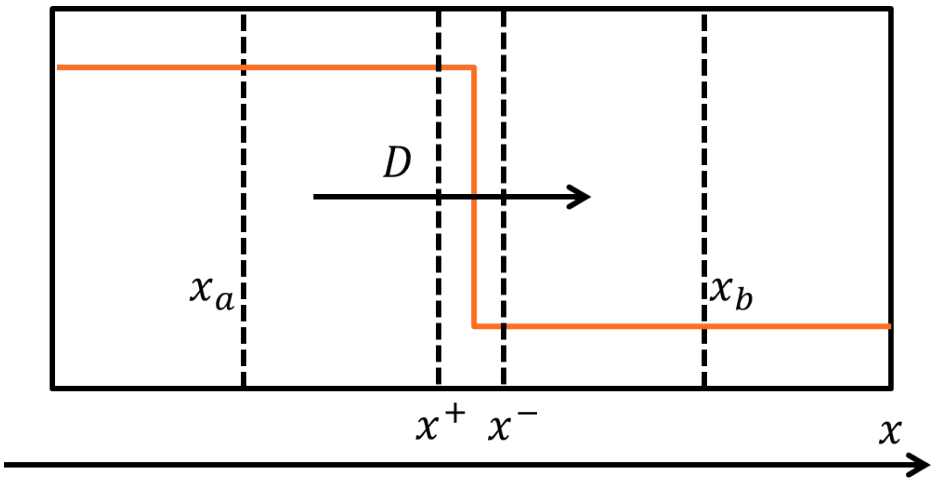

Figure 2.1: One-dimensional (1D) control volume in which a shock wave is propagating to the right with Eulerian velocity D.

the governing equations are used. Taking into account the uniaxial strain condition, the state ahead and behind the shock wave are related by shock jump conditions [5, 6] shown below.

$$\rho(D-u) = \rho_0(D-u_0) \tag{2.1}$$

$$P - P_0 = \rho_0(D-u_0)(u-u_0) \tag{2.2}$$

$$E - E_0 = \frac{1}{2}(P+P_0)(V-V_0) \tag{2.3}$$

where ρ is the density, D is the Eulerian (spatial) shock velocity, u is the particle velocity, P is the longitudinal stress, E is the internal energy per unit volume, and V is the specific volume which is the inverse of the density. In the equations above, the variables with subscript 0 represent the state ahead of (before the arrival of) the shock wave. Equations 2.1, 2.2, and 2.3 are based on conservation of mass, momentum, and energy, respectively.

2.2 Crystal Structure and Elastic Properties

Molybdenum (Mo) is a transition metal that possesses high resistance against heat and corrosion. Mo has a body centered cubic (BCC) crystal structure under ambient condition, and the structure is schematically shown in Fig. 2.2. The lattice parameter is reported to be $a = 3.1474$ Åat 291 K [7]. The atomic weight is reported to be 95.96 [8]. Hence, the theoretical density of Mo is 10.222 g/cc.

Mo single crystals were subjected to shock compression along [100], [111], and [110] orientations in our work. Table 2.1 summarizes the correspondence of those

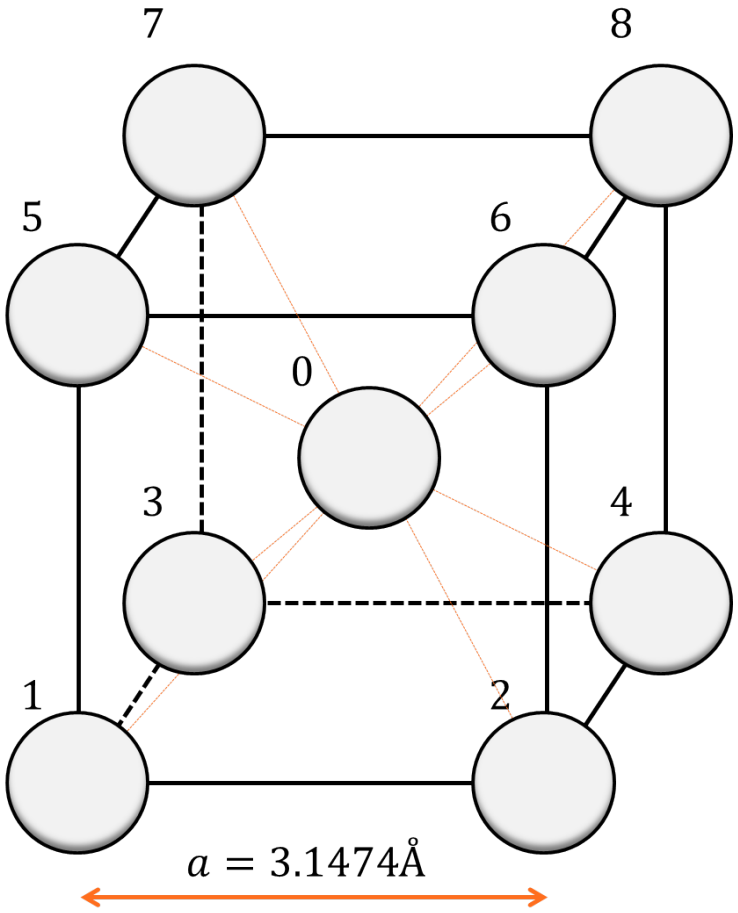

Figure 2.2: A unit cell of Mo single crystal (BCC structure).

Table 2.1: Crystallographic orientations considered in the present work

Orientation	Direction in Fig. 2.2	Atoms at Symmetric Position	Symmetry
[100]	1→3	2,5 and 2 more[1]	4-fold symmetry
[111]	1→8	2, 3 ,5	3-fold symmetry
[110]	1→6	2, 5	2-fold symmetry

orientations to the crystallographic directions in Fig. 2.2. In the second column, one of the vectors in each orientation in terms of the location of atoms shown in Fig. 2.2 is shown. Third column shows an example of a group of atoms located at symmetric positions around the particular vector.

Cubic crystals have three independent second order elastic moduli: C_{11}, C_{12}, and C_{44} in matrix notation [9], and six independent third order elastic moduli: C_{111},

[1]Two remaining atoms at the symmetric position are in adjacent unit cells.

C_{112}, C_{123}, C_{144}, C_{166}, and C_{456} in matrix notation [10]. The second order elastic moduli at the room temperature were measured by Davidson *et al.* [11] using pulse-superposition method, that was similar to the sound speed measurement in the present work. The third order elastic moduli at the room temperature were measured under hydrostatic pressures up to 1 GPa and uniaxial compression up to 0.17 GPa by Voronov *et al.* [12] by acoustic measurements. The elastic moduli are summarized in Table 2.2.

Table 2.2: Elastic moduli of molybdenum single crystals at room temperature

Second order elastic moduli [11]	C_{11}	C_{12}	C_{44}	–	–	–
[GPa]	466.1	162.6	109.5			
Third order elastic moduli [12]	C_{111}	C_{112}	C_{123}	C_{144}	C_{166}	C_{456}
[GPa]	-3557	-1333	-617	-269	-893	-555

2.3 Plastic Deformation of Mo Single Crystals

The elastic-plastic deformation of Mo single crystals under (quasi-)static loading has been well characterized. In this section, the relevant previous studies are summarized.

Slip systems

In BCC crystals, slip occurs in the [111] direction which is the closest packed direction and the corresponding Burgers vector is $\boldsymbol{b} = \frac{a}{2}[111]$ [13]. For Mo single crystals, the governing deformation mechanism was found to be dislocation slip on {110}<111> and {112}<111> systems [14–22].

In the experimental work by Irwin *et al.* [20], Mo single crystals were subjected to quasi-static compression along [100], [111], and [110] orientations. They observed that the slip lines mainly coincide with traces of irrational planes between {110} and {112}. However, they concluded that the slip on the high-index planes were due to cross slip [21] between {110} and {112} planes.

Some studies have also reported the activation of {123}<111> slip systems, but those systems were only observed under small strains on the order of 0.1%, and {110}<111> slip systems became prominent as the strain increased [17, 18].

Therefore, in this study, {110}<111> and {112}<111> slip systems are considered as the candidates for the activated deformation mechanisms in Mo single crystals under shock compression. These slip systems are schematically shown in Fig. 2.3.

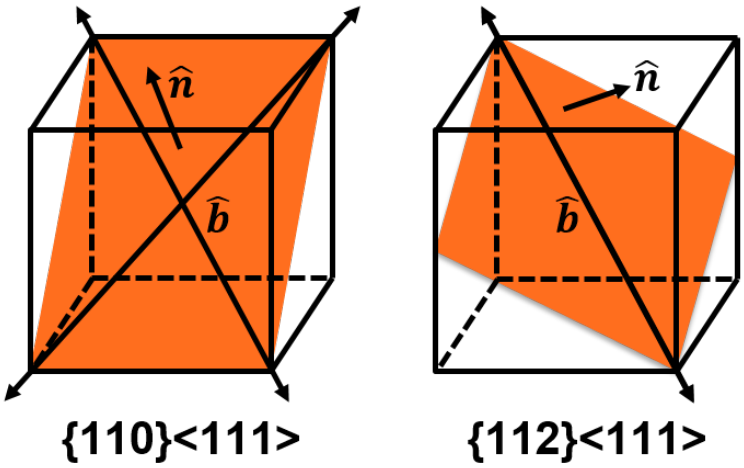

Figure 2.3: Dominant slip systems in Mo single crystals.

Role of screw and edge dislocations

In BCC metals including Mo, due to its non-planer structure, the mobility of screw dislocation is significantly lower than the mobility of edge dislocation. Thus, the threshold for the dislocation motion, Peierls stress, corresponding to the screw dislocation is more than 10 times larger than that of the edge dislocation. Therefore, the plastic deformation of Mo is dominated by the nucleation and the motion of screw dislocations [13, 17, 18, 21–24].

When the resolved shear stress (RSS) is smaller than the Peierls stress, thermally activated kink-pair formation and migration controls the plastic deformation. Above Peierls stress, the mobility of dislocations due to phonon-drag controls the plastic deformation [24]. The temperature dependence and the strain-rate dependence of the yield stress of Mo single crystals under static loading at low temperatures [16, 21, 22] are attributed to the thermally activated kink-pair formation.

The Peierls stress is the RSS required for dislocations to overcome the energy barrier without thermal effects under the ambient pressure. For Mo single crystals, Hollang *et al.* [21] calculated the Peierls stress for screw dislocations based on kink-pair theory [23]. The Peierls stress for screw dislocations was computed to be 870±10 MPa on {110} planes, and 690±10 MPa on {112} planes [21].

Yang *et al.* [24] reported the pressure dependence of the Peierls stress. Based on atomistic calculations, they showed that the ratio between the Peierls stress and the shear modulus stays constant for the pressure up to ~400 GPa, while the shear

modulus increases with pressure.

Twinning-antitwinning asymmetry

Guiu [25] subjected Mo single crystals to shear along [111] orientation in the range 77 - 295 K, and found that the ratio of critical resolved shear stress (critical RSS) for the hard and soft {112}<111> systems was around 1.5. This difference in the critical RSS on {112}<111> systems depending on direction of shear is referred to as twinning-antitwinning asymmetry. In this subsection, the cause of the twinning-antitwinning asymmetry is described below based on models for stacking fault in BCC single crystals [26].

In BCC single crystals, the stacking sequence of {112} planes has 6-layer repetition [26]. Figure 2.4 schematically shows the stacking sequence. The Burgers vector corresponding to unit slip is $\frac{a}{2}[111]$ [13].

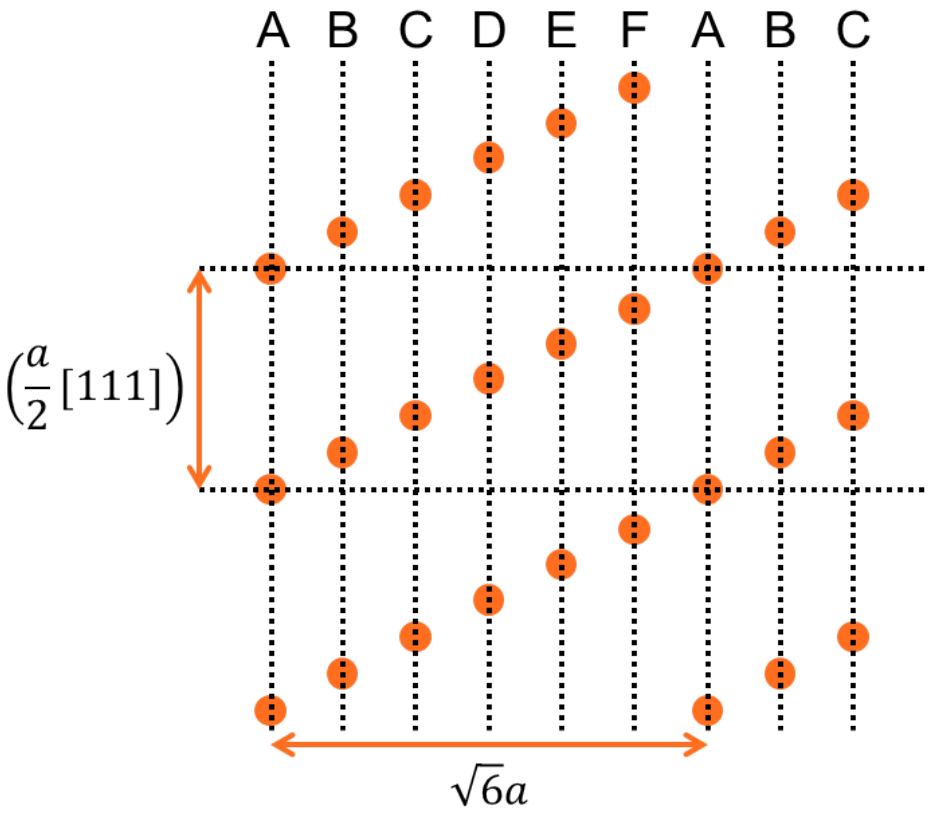

Figure 2.4: Schematic of stacking sequence along [112] direction in BCC single crystals. Each vertical line corresponds to an {112} plane. The distance between two horizontal lines corresponds to a projection of $\frac{a}{2}[111]$ vector onto [112] direction.

In Fig. 2.4, let us assume that the atoms are displaced in a part of the crystal, right of the second vertical lines from the left. Depending on the direction of the displacement, the resulting arrangement of the atoms are different. They are shown in Figs. 2.5 and 2.6. The amplitude of deformation is assumed to be $\frac{a}{6}[111]$.

In Figs. 2.4 - 2.6, the character above each vertical dotted line represents the order in the repetition. In Fig. 2.5, the order is ABABCDEFA. Two layers AB are inserted into the original repetition, and this corresponds to a monolayer twin (twinning only on the third layer from the left). On the other hand, in Fig. 2.6, the order is ABEFABCDE. Four layers EFAB are inserted into the original repetition, which is different from the former case and this does not correspond to a monolayer twin. We can see that those are energetically different, and that is the origin of twinning-antitwinning symmetry. Figure 2.5 corresponds to the deformation in the twinning sense, and Fig. 2.6 corresponds to the deformation in the antitwinning sense. Since the deformation in the twinning sense is energetically favourable, the critical RSS is lower for the {112}<111> slip systems in a twinning sense.

In contrast to the {112}<111> slip systems, for the {110}<111> slip systems, the stacking sequence of {110} planes in BCC single crystals has a two-layer repetition [26]. Therefore, the displacements in both directions along [111] direction result in the equivalent arrangements of the atoms. Therefore, the asymmetry discussed above does not exist for {110}<111> slip systems in BCC single crystals.

2.4 Shock Studies on BCC Single Crystals

In this section, previous experimental studies on BCC single crystals which measured wave profiles using plate impact experiment are summarized.

Molybdenum single crystals

Among previous shock studies on BCC single crystals, studies on molybdenum (Mo) single crystals by Mandal *et al.* [27–29] are the most comprehensive. In their work, Mo single crystals were subjected to shock compression to 12.5 GPa impact stress along [100], [111], and [110] orientations, and the particle velocity was measured at varying propagation distances. The elastic wave amplitude and the decay rate with propagation distance showed clear anisotropic effect. The elastic wave amplitude at sufficiently large thickness was ~5.3 GPa along [111] orientation and ~3.6 GPa along [100] and [110] orientations. The resolved shear stresses (RSS) on {110}<111> and {112}<111> slip systems at the elastic limit for sufficiently large sample thickness were calculated, and the calculation suggested that the RSS attenuates rapidly when

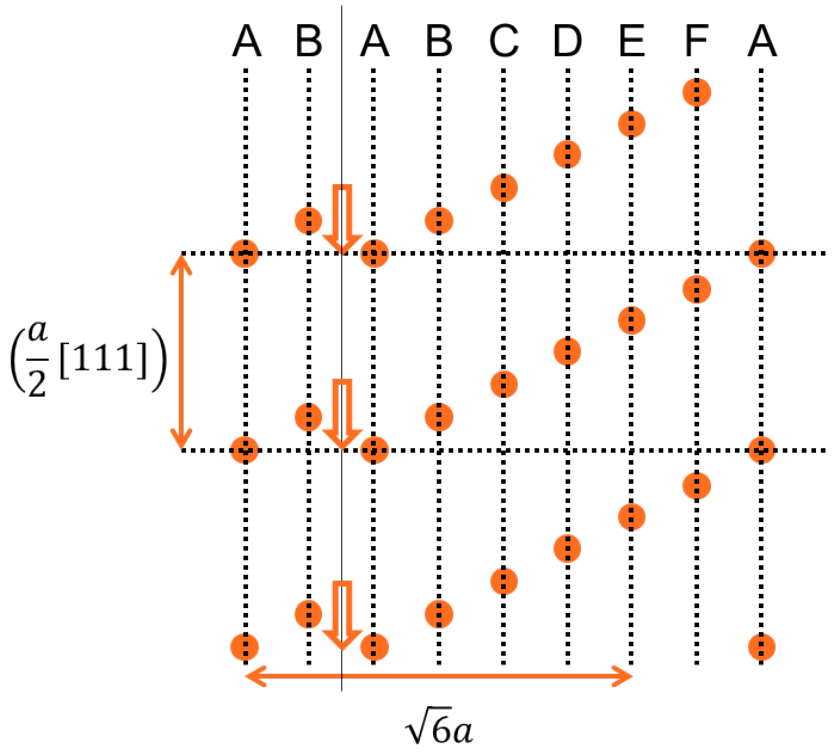

Figure 2.5: Schematic of a resulting arrangement of atoms by a deformation in twinning sense.

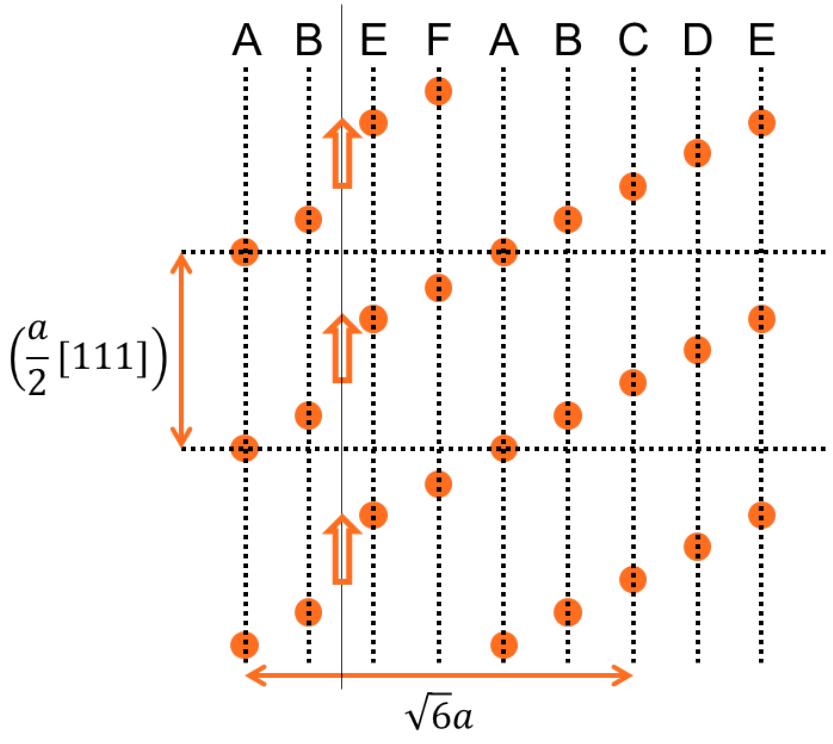

Figure 2.6: Schematic of a resulting arrangement of atoms by a deformation in antitwinning sense.

RSS was greater than the corresponding Peierls stress [21]. They also conducted numerical simulations based on the nonlinear anisotropic framework developed by Winey *et al.* [30]. The results from the numerical simulations showed that the {110}<111> and the {112}<111> slip systems are activated under shock loading. Also, the nucleation term which accounted for an increase in the plastic strain rate above the Peierls stress was essential to obtain reasonable agreement with experiments. In their work, the impact stress was kept constant at a relatively low stress (12.5 GPa). Thus, the impact stress dependence of the elastic limit was not considered. Also, their experimental and numerical work did not conclusively determine which of the two slip systems were activated during the shock induced deformation.

Kanel *et al.* [31] also examined Mo single crystals under shock compression along [100], [111], and [110] orientations. In their experiments, shock waves were generated either by an aluminum (Al) impactor or a high-power proton beam. The range of peak stress was up to ~100 GPa for their plate impact experiments with Al impactors. Since Kanel *et al.* primarily focused on the spall strength of Mo single crystals and porycrystalline Mo, the elastic limit and the peak state were not fully analyzed. The average elastic wave amplitude was reported to be 3.7±0.5 GPa.

Tantalum single crystals

Whiteman *et al.* [32] examined Tantalum (Ta) single crystals along [100], [111], and [110] orientations under shock compression. The thickness of the samples was kept constant at ~4 mm, and the peak stresses ranged from 6 GPa to 23 GPa. The particle velocity was measured on the back surface (free surface) of Ta single crystal samples using frequency shifted heterodyne velocimetry system [33]. At 6.4 GPa peak stress, the measured free surface velocity exhibited time-dependent response and the elastic limit showed anisotropic effect. However, at 23 GPa peak stress, the peak of the elastic limit was not measured accurately due to low return signal strength level in the heterodyne velocimetry system. Hence, the anisotropic effect at the elastic limit at 23 GPa peak stress was not clear. Also, the impact stress dependence was not discussed. Whiteman *et al.* [32] also carried out a finite element simulation incorporating dislocation dynamics-based model, but the model did not capture the anisotropic behavior at the elastic limit.

Pang *et al.* [34] subjected Ta single crystals to shock compression along [100], [111], and [110] orientations to 6 GPa peak stress. In their work, the shocked Ta

single crystals were recovered and investigated using scanning electron microscopy and transmission electron microscopy for shock induced defect evolution. Along all orientations, twinning on the planes of {112} family and voids along the twinning boundaries were observed. The distribution of the twins and the size of the voids were found to be orientation dependent. Since their work was based on sample recovery, the loading history was more complex than the uniaxial strain loading. Their work gives a good starting point for the determination of deformation mechanisms during the shock, however it is not conclusive.

Tungsten single crystals

Michaels *et al.* [35] subjected Tungsten (W) single crystals to shock compression along [100], [111], and [110] orientations. Their work was also mentioned in Johnson *et al.* [4]. At 7.5 GPa impact stress with 3 mm thickness sample, the elastic wave amplitude showed anisotropic effect: the elastic wave amplitude was 2.8, 4.0, and 3.3 GPa along [100], [111], and [110] orientation, respectively. A dislocation-based model was used to simulate the measured wave profile, and their data supported the operation of {110}<111> and {112}<111> slip systems, which was previously found to be activated under quasi-static loading. Since the experimental data at only one impact stress were reported, the impact stress dependence of the elastic wave amplitude is not clear.

Iron single crystals

Jensen *et al.* [36] examined α-phase (BCC) iron single crystals under shock compression to peak stresses above 13 GPa. The α-phase iron single crystal is known to undergo polymorphic phase transition above 13 GPa. Iron single crystals were shock compressed along [100], [110], and [210] orientations, and the sample thickness was nominally 0.7 mm. Liu *et al.* [37] also examined α-phase iron single crystals under shock compression. In their work, iron single crystals were shock compressed along [100], [111], and [110] orientations to $\sim$ 23 GPa peak stress at the propagation distance of 1.15 mm. In both of the works on iron single crystals, the elastic amplitude showed anisotropic effect, and the elastic amplitude was largest along [100] orientation. In the experiments along the other orientations, a release behind the elastic limit was observed [36, 37]. Since their main focus was on the shock-induced phase transition, the impact stress dependence of the elastic wave amplitude was not considered in these works.

2.5 Shock Studies on Single Crystals at High Stresses

For BCC single crystals, there have been no previous studies that investigated the elastic-plastic deformation under shock compression to high stresses. In contrast, there have been some relevant studies on FCC single crystals at high stresses. This section reviews relevant studies on aluminum (Al) single crystals [38] and copper (Cu) single crystals [39] under shock compression to high stresses.

Choudhuri *et al.* [38] examined the deformation of Al single crystals along [100], [111], and [110] orientations at peak stresses ranging from 40 GPa to 70 GPa, and reported that the Hugoniot relations were not distinguishable between three orientations. They also reported that the longitudinal sound speed in the shocked state exhibited anisotropy. Chau *et al.* [39] subjected Cu single crystals to shock compression along [100], [111], and [110] orientations to 9 - 67 GPa peak stresses, and reported that the Hugoniot relations for the three orientations agreed well with polycrystalline data [40]. However, except for the lowest impact velocity in Chau *et al.* [39], these studies reported overdriven, single wave profiles. Hence, these studies on Al and Cu did not consider the effect of elastic limit on the peak state as the preceding state.

2.6 Shock Studies on Polycrystalline Molybdenum

In contrast to single crystals, there is a notable previous work on the peak state of shock compressed polycrystalline Mo. Hixson *et al.* [41] examined shock response of polycrystalline Mo using a two-stage light gas gun. In conjunction with previous experimental data [42], they considered the peak stresses ranging from 180 GPa to 480 GPa. They also utilized data from low stress experiments [43] and provided overall linear fit for $U_s - u_p$ relation,

$$U_s = (5.122 \pm 0.015) + (1.245 \pm 0.007)u_p \tag{2.4}$$

where $0.44 \leq u_p \leq 4.40$ km/s. It is noted that such linear relation is empirical, but it is observed in a wide range of materials. For the wide variety of materials investigated by Swegle *et al.* [44], the tangent of the $U_s - u_p$ relation falls in the range of 1.1-1.5 [45].

2.7 Motivation

From the literature survey, the studies on the BCC single crystals shock compressed to high stress range appear to be minimal. For BCC single crystals, the effect of anisotropy and the impact stress on the elastic limit under high stress has not been

studied. Also, the effect of anisotropy at the peak state in BCC single crystals has remained unexplored.

In view of the areas that have been minimally explored, the present work focused on the elastic-plastic deformation of Mo single crystals shocked to various impact stresses along three crystal orientations: [100], [111], and [110]. In addition to the plate impact experiments, finite element method (FEM) simulations were carried out using Abaqus Explicit [46] in order to gain insight into the contributing deformation mechanisms in Mo single crystals shock compressed to high stresses.

Specifically, the following questions were addressed through the present work. The research questions can be grouped into two categories: regarding elastic limit and regarding peak state.

Regarding elastic limit:

- How does the elastic wave amplitude under high impact stresses compare with the lower stress data from Mandal *et al.* [27–29]?
- Does the elastic wave amplitude show dependence on the impact stress?
- What is the role of anisotropy at high stresses?
- What slip systems contribute to yielding at the elastic limit? Can high stress experiments distinguish between {110}<111> and {112}<111> slip systems?

Regarding peak state:

- How do the in-material quantities at the peak state depend on crystal orientation?
- When two-wave structure is observed, how does the peak state depend on the preceding state (elastic limit)?
- How does the Hugoniot relations compare with the polycrystalline Mo Hugoniot [41]? Is the empirical linear $U_s - u_p$ relation applicable for Mo single crystals?

References

[1] L. M. Barker and R. E. Hollenbach. “Laser interferometer for measuring high velocities of any reflecting surface.” In: *Journal of Applied Physics* 43.11 (1972), p. 4669.

[2] L. M. Barker and K. W. Schuler. “Correction to the velocity-per-fringe relationship for the VISAR interferometer.” In: *Journal of Applied Physics* 45.8 (1974), p. 3692.

[3] S. P. Marsh. *LASL shock Hugoniot data.* Vol. 5. Univ. of California Press, 1980.

[4] J. N. Johnson, O. E. Jones, and T. E. Michaels. “Dislocation Dynamics and Single-Crystal Constitutive Relations: Shock-Wave Propagation and Precursor Decay.” In: *Journal of Applied Physics* 41.6 (1970), p. 2330.

[5] L. Davison. *Fundamentals of shock wave propagation in solids.* Springer Science & Business Media, 2008.

[6] Y. M. Gupta. *Wave Propagation Seminar (Physics 592) Lecture Notes.* Washington State University (2017).

[7] J. W. Edwards, R. Speiser, and H. L. Johnston. “High temperature structure and thermal expansion of some metals as determined by X-ray diffraction data. I. Platinum, tantalum, niobium, and molybdenum.” In: *Journal of Applied Physics* 22.4 (1951), p. 424.

[8] M. E. Wieser et al. “Atomic weights of the elements 2011 (IUPAC Technical Report).” In: *Pure and Applied Chemistry* 85.5 (2013), p. 1047.

[9] J. F. Nye. *Physical properties of crystals: their representation by tensors and matrices.* Oxford University Press, 1985.

[10] J. P. Jarić and D. S. Kuzmanović. “On the Elasticity Tensor of Third Order.” In: *Theoretical and Applied Mechanics* 26 (2001), p. 91.

[11] D. L. Davidson and F. R. Brotzen. “Elastic Constants of Molybdenum-Rich Rhenium Alloys in the Temperature Range -190 °C to +100 °C.” In: *Journal of Applied Physics* 39.12 (1968), p. 5768.

[12] F. F. Voronov, V. M. Prokhorov, E. L. Gromnitskaya, and G. G. Il’ina. “Second- and Third-Order Elasticity Moduli of a Molybdenum Single Crystal.” In: *Phys. Met. Metallogr.* 45.6 (1978), p. 123.

[13] C. R. Weinberger, B. L. Boyce, and C. C. Battaile. “Slip planes in bcc transition metals.” In: *International Materials Reviews* 58.5 (2013), p. 296.

[14] N. K. Chen and R. Maddin. “Plasticity of molybdenum single crystals.” In: *Journal of Metals* 3.10 (1951), p. 937.

[15] P. J. Sherwood, F. Guiu, H. C. Kim, and P. L. Pratt. “Plastic anisotropy of tantalum, niobium, and molybdenum.” In: *Canadian Journal of Physics* 45.2 (1967), p. 1075.

[16] S. S. Lau, S. Ranji, A. K. Mukherjee, G. Thomas, and J. E. Dorn. “Dislocation mechanisms in single crystals of tantalum and molybdenum at low temperatures.” In: *Acta Metallurgica* 15.2 (1967), p. 237.

[17] D. Veselý. “The Study of Deformation of Thin Foils of Mo under the Electron Microscope.” In: *Physica Status Solidi* 29 (1968), p. 675.

[18] D. Veselý. “The Study of Slip Bands on the Surface of Mo Single Crystals.” In: *Physica Status Solidi* 29 (1968), p. 685.

[19] S. S. Lau and J. E. Dorn. “Asymmetric slip in Mo single crystals.” In: *Physica Status Solidi (a)* 2.4 (1970), p. 825.

[20] G. J. Irwin, F. Guiu, and P. L. Pratt. “The influence of orientation on slip and strain hardening of molybdenum single crystals.” In: *Physica Status Solidi (a)* 22.2 (1974), p. 685.

[21] L. Hollang, D. Brunner, and A. Seeger. “Work hardening and flow stress of ultrapure molybdenum single crystals.” In: *Materials Science and Engineering: A* 319 (2001), p. 233.

[22] A. Seeger and L. Hollang. “The flow-stress asymmetry of ultra-pure molybdenum single crystals.” In: *Materials Transactions, JIM* 41.1 (2000), p. 141.

[23] A. Seeger. “The flow stress of high-purity refractory body-centred cubic metals and its modification by atomic defects.” In: *Le Journal de Physique IV* 5.C7 (1995), pp. C7–45.

[24] L. H. Yang, M. Tang, and J. A. Moriarty. “Dislocations and plasticity in bcc transition metals at high pressure.” In: *Dislocations in Solids* 16 (2010), p. 1.

[25] F. Guiu. “Slip asymmetry in molybdenum single crystals deformed in direct shear.” In: *Scripta Metallurgica* 3.7 (1969), p. 449.

[26] V. Vítek. “Theory of the core structures of dislocations in body-centered-cubic metals.” In: *Crystal Lattice Defects* 5 (1974), p. 1.

[27] A. Mandal and Y. M. Gupta. “Elastic-plastic deformation of molybdenum single crystals shocked along [100].” In: *Journal of Applied Physics* 121.4 (2017), p. 045903.

[28] A. Mandal and Y. M. Gupta. “Elastic-plastic deformation of molybdenum single crystals shocked to 12.5 GPa: Crystal anisotropy effects.” In: *Journal of Applied Physics* 125.5 (2019), p. 055903.

[29] A. Mandal. “Elastic-Plastic Deformation of Molybdenum Single Crystals Shocked to 12.5 GPa.” PhD thesis. Washington State University, School of Mechanical and Materials Engineering, 2016.

[30] J. M. Winey and Y. M. Gupta. “Nonlinear anisotropic description for the thermomechanical response of shocked single crystals: inelastic deformation.” In: *Journal of Applied Physics* 99.2 (2006), p. 023510.

[31] G. I. Kanel et al. “Spall strength of molybdenum single crystals.” In: *Journal of Applied Physics* 74.12 (1993), p. 7162.

[32] G. Whiteman, S. Case, and J. C. F. Millett. “Planar shock compression of single crystal tantalum from 6-23 GPa.” In: *Journal of Physics: Conference Series*. 500. 11. IOP Publishing. 2014, p. 112067.

[33] O. T. Strand, D. R. Goosman, C. Martinez, T. L. Whitworth, and W. W. Kuhlow. “Compact system for high-speed velocimetry using heterodyne techniques.” In: *Review of Scientific Instruments* 77.8 (2006), p. 083108.

[34] B. Pang et al. “The defect evolution in shock loaded tantalum single crystals.” In: *Acta Materialia* 148 (2018), p. 482.

[35] T. E. Michaels and G. E. Duvall. “Elastic precursor decay in single crystal tungsten.” In: *Bulletin of the American Physical Society*. Vol. 14. 12. 1969, p. 1170.

[36] B. J. Jensen et al. “Dynamic Compression of Iron Single Crystals.” In: *AIP Conference Proceedings: Shock Compression of Condensed Matter - 2005*. Vol. 845. 2006, p. 232.

[37] X. Liu, T. Mashimo, N. Kawai, T. Sano, and X. Zhou. “Isotropic phase transition of single-crystal iron (Fe) under shock compression.” In: *Journal of Applied Physics* 124.21 (2018), p. 215101.

[38] D. Choudhuri and Y. M. Gupta. “Shock compression of aluminum single crystals to 70 GPa: Role of crystalline anisotropy.” In: *Journal of Applied Physics* 114.15 (2013), p. 153504.

[39] R. Chau, J. Stölken, P. Asoka-Kumar, M. Kumar, and N. C. Holmes. “Shock Hugoniot of single crystal copper.” In: *Journal of Applied Physics* 107.2 (2010), p. 023506.

[40] A. C. Mitchell and W. J. Nellis. “Shock compression of aluminum, copper, and tantalum.” In: *Journal of Applied Physics* 52.5 (1981), p. 3363.

[41] R. S. Hixson and J. N. Fritz. “Shock compression of tungsten and molybdenum.” In: *Journal of Applied Physics* 71.4 (1992), p. 1721.

[42] A. C. Mitchell et al. “Equation of state of Al, Cu, Mo, and Pb at shock pressures up to 2.4 TPa (24 Mbar).” In: *Journal of Applied Physics* 69.5 (1991), p. 2981.

[43] R. G. McQueen, S. P. Marsh, J. W. Taylor, J. N. Fritz, and W. J. Carter. “The equation of state of solids from shock wave studies.” In: *High-Velocity Impact Phenomena*. Ed. by R Kinslow. New York: Academic Press, 1970, pp. 293–417.

[44] J. W. Swegle and D. E. Grady. “Shock viscosity and the prediction of shock wave rise times.” In: *Journal of Applied Physics* 58.2 (1985), p. 692.

[45] A. Molinari and G. Ravichandran. “Fundamental structure of steady plastic shock waves in metals.” In: *Journal of Applied Physics* 95.4 (2004), p. 1718.

[46] Dassault Systemés. *Abaqus 2016 Documentation.* ivt-abaqusdoc.ivt.ntnu.no:2080/v2016/. [Online; accessed 2019 December 14].

Chapter 3

EXPERIMENTAL METHODS

The plate impact experiments described in Section 2.1 provide a unique way to investigate the material behavior at the high stress range. In this chapter, sample preparation, associated ambient measurements, target assembly, and instrumentation are described. All of the experiments in this study has been carried out at the Institute for Shock Physics, Washington State University.

3.1 Sample Preparation

In each plate impact experiment, there were three target components and an impactor. Target assembly consisted of a Mo single crystal, a buffer, and a lithium fluoride (LiF) [100] oriented optical window. For all of the experiments, the impactor and the buffer were chosen to be the same material, either 1050 aluminum alloy (Al) or C101 Copper (Cu), to achieve a symmetric impact. Cu was used for most of the experiments, and Al was used for 23 GPa impact stress experiments. This was to ensure that the shock wave propagating into the buffer was overdriven, single wave, in order to simplify the wave propagating into the Mo single crystal sample. In this section, the preparation of each target component is elaborated.

Mo single crystal sample

Molybdenum single crystals were obtained from Accumet Materials Co. (Ossining, NY) in the form of cylindrical bar with approximately 30 mm diameter. Each of the bar was oriented so that the longitudinal direction aligns with [100], [111], or [110] crystal orientation, respectively.

Molybdenum single crystals were first machined to approximately 13 mm diameter and thickness that was approximately 0.5 mm thicker than the desired sample thickness. This process was done with the help of the materials engineer, Nate Arganbright, at the Institute for Shock Physics, Washington State University.

A bar of Mo single crystal was potted into a thin walled cylinder made of Al using 815 epoxy. This has been done in a way that the normal of the end surfaces of the cylinder aligned with the desired crystal orientation of the Mo single crystal. A slight tilt of the crystal orientation in the Mo single crystal bar was determined using

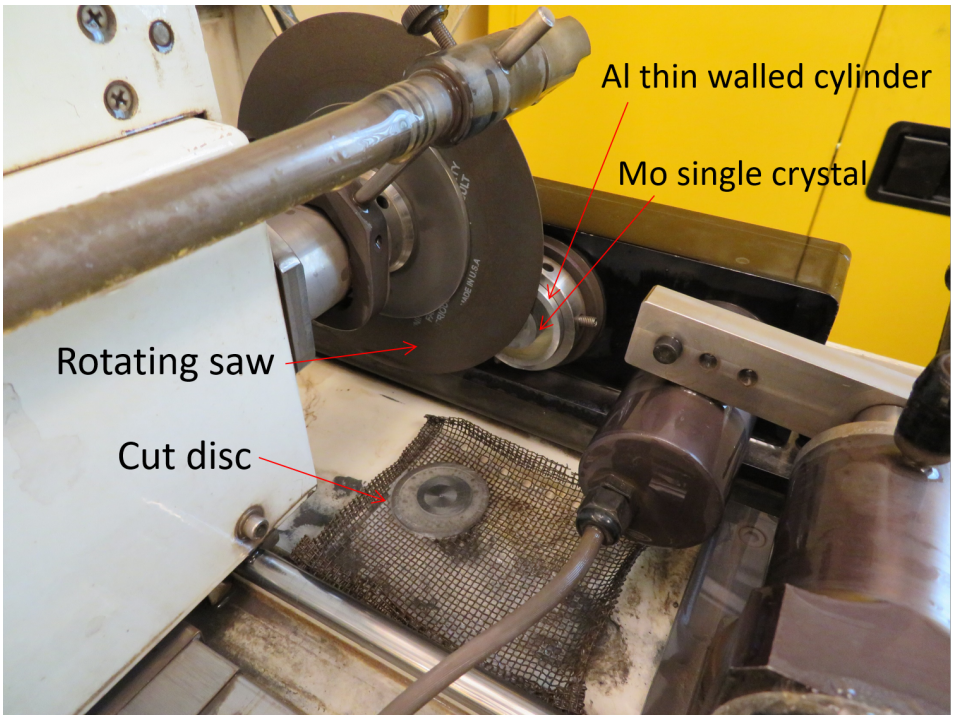

Figure 3.1: ISOMET®4000 linear precision saw and a Mo single crystal disc.

Laue diffraction, and was compensated in this process. This enables us to mount the bar of Mo single crystal in the chuck of an ISOMET®4000 linear precision saw, in a desired orientation. A silicon carbide blade was used to cut a disc of Mo. Figure 3.1 shows a bar of Mo single crystal being mounted in the chuck, and a disc cut by the rotating silicon carbide blade.

After the disc was cut out, the 815 epoxy surrounding the disc of Mo single crystal was removed. The disc of Mo single crystal was lapped in order to make the surfaces flat for the X-ray Laue diffraction measurement. The process for lapping is described in detail later. Then, the orientation of the crystal was checked with Laue diffraction again. The disc of Mo single crystal was screwed onto a square Al block, then secured onto the drill. This is shown in Fig. 3.2. A diamond core drill whose inner diameter was 12.8 mm was used to cut out two samples from the Mo single crystal disc. Silicon carbide grinding compound, which is the grey liquid shown in Fig. 3.2(b), and water were constantly added to suppress the heat and to maintain the abrasiveness for cutting. The drill was pushed gently on the sample, in an intermittent manner, in order to suppress the excess heating of the drill. The cutting rate was kept approximately 1 μm/s. Once the drill had cut entirely through the Mo single crystal disc, the drill was unscrewed from the machine and the Mo single

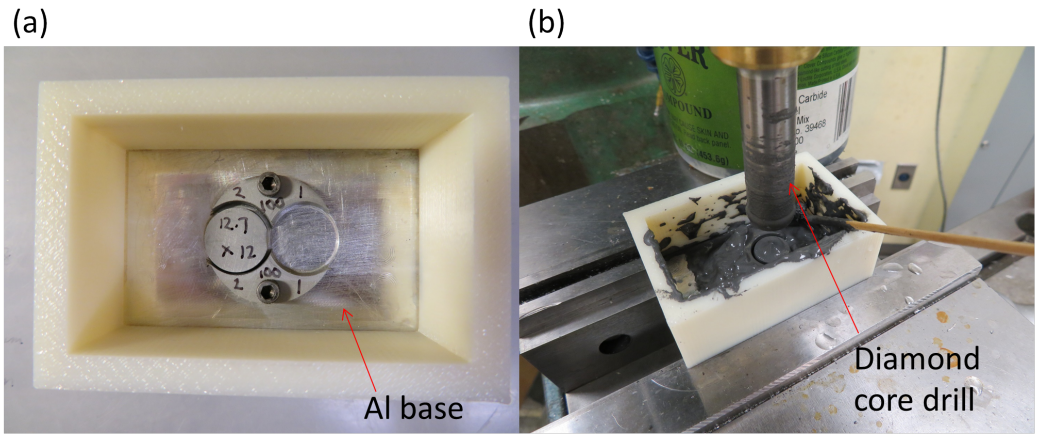

Figure 3.2: Machining process of Mo single crystal sample. (a) A Mo single crystal disc screwed onto an Al block. (b) Two samples being cut out from a disc by diamond core drill.

crystal sample was taken out. Because of the vibration of the drill, the diameter of the cut samples became smaller towards the bottom surface. The difference of the diameter of the two surfaces was not significant. However, in order to ensure longer time window for the velocity profile measurement, the bigger surface of Mo single crystal sample was chosen to be on the impact side in the target assembly.

After two Mo single crystal samples were cut, each sample was lapped using LAPMASTER® lapping machine until the thickness was approximately 20 μm larger than the desired thickness. The sample was put inside a jig that pushes the sample against the rotating plate of the lapping machine. 20 μm aluminum oxide grit was used in the lapping process, and the speed of lapping in terms of the decrease in the thickness was around 6 μm/min. At the beginning of the lapping, the sample was flipped every 10 minutes, and as it approached to the end, the sample was flipped every one minute to achieve flat and parallel surfaces. The parallelism of the sample was inspected by measuring the thickness at five different locations. The difference in the thickness was kept below 5 μm at the end of the lapping process. The picture of the lapping machine is shown in Fig. 3.3(a).

After the lapping, the Mo sample was polished down to the desired thickness. Oil-based diamond polishing compound was applied onto paper that was attached to a rotating table, and the Mo single crystal sample was pushed against the paper by hand. There were four types of polishing compounds, and each of them contained 15, 9, 3, and 1 μm diamond grit, respectively. Polishing was done step-wise to

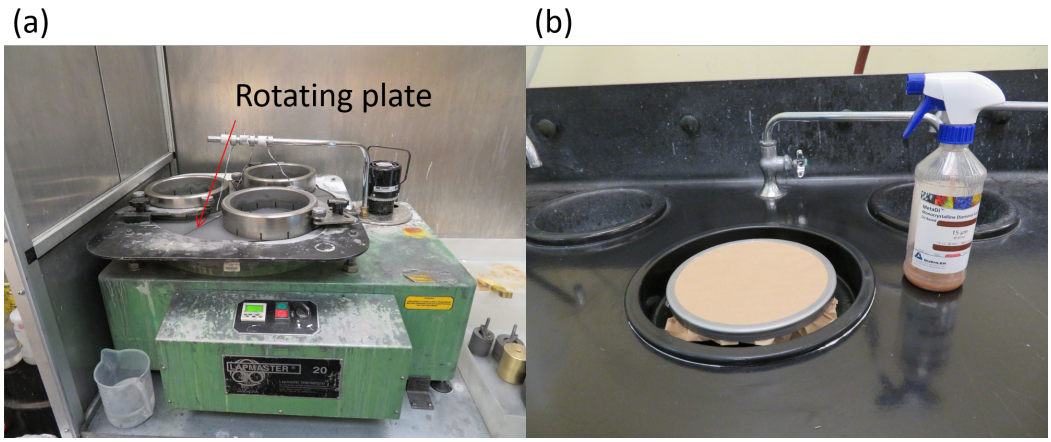

Figure 3.3: Apparatuses for lapping and polishing. (a) LAPMASTER®lapping machine. (b) Polishing table and oil-based diamond polishing compound.

achieve 1 μm surface finish. At the end of each step, the parallelism of the sample was inspected. Good surface finish was needed to get reflective surface for the velocity measurement using VISAR [1, 2]. After polishing, flatness of the sample was checked using Edmund optics optical flats. Figure 3.3(b) shows the apparatuses for polishing.

After the polishing, the Mo single crystal sample was characterized under ambient condition. This process is described in Section 3.2. Once characterized, the Mo sample was polished again with 1 μm diamond grid, in order to remove scratches potentially generated during the characterization.

Impactor

As mentioned earlier in this chapter, the impactor was made either from Al or Cu. There are three types of impactors used in the experiments. The nominal dimensions of each type of impactor are summarized in Table 3.1

Table 3.1: Nominal dimension of impactors

Material	Impact Facility	Impact Stress [GPa]	Diameter of Impact Surface [mm]	Thickness [mm]	Mass [g]
Al	Powder gun	23	25.4	1.8	2.5
Cu	Powder gun	67	25.4	1.7	7.7
Cu	Two-stage light gas gun[1]	90, 110, 190	25.4	1.1[2] 3.0	3.6 9.9

An impactor was first manufactured at a machine shop at the Washington State University. The impactor was then lapped flat and parallel using the corresponding lapping jig. In the lapping process, the impactor was flipped every 30 seconds for the first 2 minutes, every 20 seconds for the subsequent 2 minutes, and every 15 seconds for the last 2 minutes. This process ensured the parallelism. If an impactor was thicker than the desired thickness at this point, the impactor was then lapped further. For the impactors for two-stage light gas gun, the excess thickness was removed only from the smaller diameter surface, in order to preserve the tapered lip on the back side. The parallelism of the impactor was inspected by measuring the thickness at five different locations. The difference in the thickness was kept below 7 μm at the end of the lapping.

After the lapping process, the impactor was polished with 15 and 9 μm oil-based diamond polishing compounds, to obtain 9 μm surface finish. The procedure for polishing was the same as the Mo single crystal sample. After the polishing, the impactor was characterized under ambient condition, which is described in Section 3.2. Once characterized, the impactor for the two-stage light gas gun was molded into a polycarbonate base. The impactor for the powder gun was bonded onto a polycarbonate base using 815 epoxy. Figure 3.4 shows the prepared projectiles of each type.

Buffer

To achieve a symmetric impact, the buffer and the impactor were made from the same material. In our experiments, the dimension of the buffer was the same for all of the experiments. The nominal dimensions were 31.75 mm in diameter and 0.93 mm in thickness.

A buffer was first machined to approximately 0.2 mm thicker than the desired value at a machine shop in the Washington State University. The buffer was then lapped flat and parallel using the corresponding lapping jig. In the lapping process, the buffer was flipped every 5 minutes at the beginning, and as it approached to the end, the buffer was flipped every one minute to achieve flat and parallel surfaces. The parallelism of the buffer was inspected by measuring the thickness at five different

[1]Impactor for two-stage light gas gun has a thin tapered lip on the back side, and the impact side has a smaller diameter.

[2]Those impactors initially had 3.0 mm thickness. Since bowing of impactor was observed in 190 GPa impact stress experiments, the impactor design was later modified to 1.1 mm thickness. The impactor bowing was compensated with corresponding corrections that were determined from separate experiments.

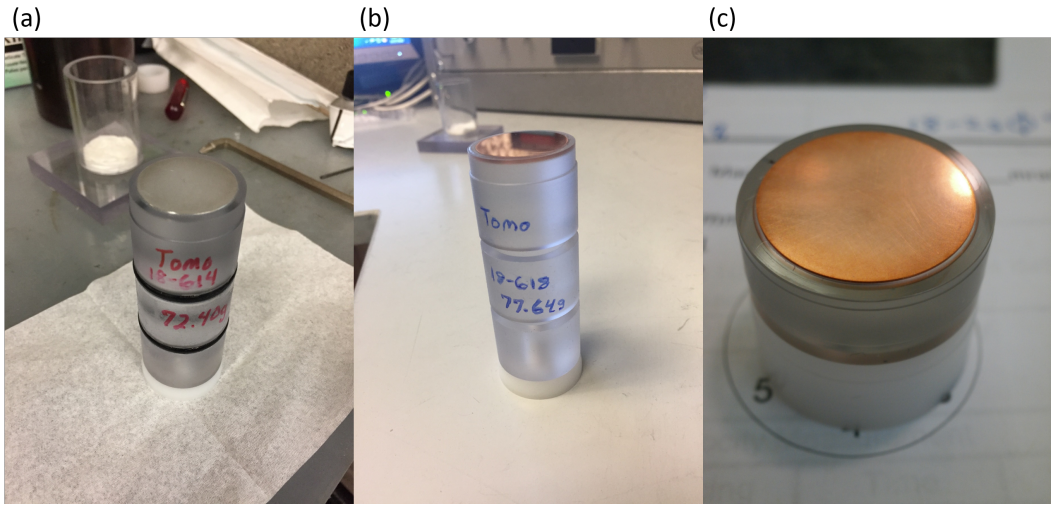

Figure 3.4: Prepared projectiles for (a) powder gun with an Al impactor. (b) powder gun with a Cu impactor. (c) two-stage light gas gun with a Cu impactor.

locations. The difference in the thickness was kept below 7 μm at the end of the lapping.

The polishing process for the buffer had two steps. For the first step, the buffer was polished with 15 and 9 μm oil-based diamond polishing compounds, to obtain 9 μm surface finish. After the first step, the buffer was characterized under ambient condition as in Section 3.2. Then for the second step, one of the surfaces of the buffer was further polished with 3 and 1 μm oil-based diamond polishing compounds, to obtain 1 μm surface finish.

The buffer was prepared this way because both Al and Cu are susceptible to scratches during the characterization process. 1 μm surface finish was needed to obtain good reflective surface for the VISAR measurements.

LiF [100] optical window

LiF [100] crystals were obtained from ASPHERA Inc. (Santa Cruz, CA). The nominal dimensions of the as-received LiF crystals was 12.7 mm in diameter and 6.35 mm in thickness. In our experiments, LiF crystals were used as an optical window. Since LiF crystals dissolve in water, the whole process had to be done with extra care. LiF crystals were first characterized under ambient condition in order to ensure that the dimensions, sound speed and the misorientation of the crystal were consistent between experiments. This process is described in Section 3.2. A few of the LiF crystals had misorientation larger than 2 degrees, and those crystals were

discarded. Since LiF crystals were already optically polished, and reasonably flat and parallel, they were used as received in our experiments.

After the ambient measurements, an Al mirror was vapor deposited onto a surface of the LiF window. This mirror reflected the signal from/to VISAR at the center of the back surface of the Mo single crystal sample.

3.2 Ambient Measurements

Before each experiment, all of the components in the target and the impactor were characterized under the ambient condition to check the consistency of materials between experiments. This included the sound speed measurement which is described below and the density measurement using the Archimedean method. Also, for Mo single crystal and LiF [100] window, the orientation of crystals were checked using X-ray Laue diffraction.

The velocity of infinitesimal disturbance in a crystal is referred to as sound speed. In single crystals, pure longitudinal wave and pure shear wave can propagate only along certain orientations. Such orientations are referred to as specific directions [3]. In a cubic crystal such as Mo and LiF, [100], [111], and [110] are specific directions. In an isotropic material, every orientation is a specific direction, and the buffer and impactor materials, 1050 aluminum alloy (Al) and C101 copper (Cu) can be treated as isotropic materials. Therefore, all of the measurements in this study were along specific directions. For each material along a specific direction, there is one longitudinal sound speed, and one or two shear sound speed depending on the dimensionality of the eigenspace of the acoustic tensor.

Sound speed was measured using ultrasonic transducers and the pulse-echo overlap technique. The transit time was measured, and the velocity was calculated using known thickness.

The results of the sound speed measurement and the density measurement are summarized in two tables below. Table 3.2 shows the ambient properties of Mo single crystals and Table 3.3 shows the results for the other materials. It is noted that the measured density of Mo was consistent with the theoretical density calculated in Section 2.2.

Table 3.2: Ambient properties of Mo single crystals

Orientation	Density [g/cc]	Longitudinal Sound Speed [km/s]	Shear Sound Speed [km/s]
[100]	10.22±0.06	6.746±0.008	3.261±0.005
[111]		6.319±0.005	3.666±0.014
[110][1]		6.432±0.003	3.850±0.004 3.264±0.004

Table 3.3: Ambient properties of other materials

Material	Density [g/cc]	Longitudinal Sound Speed [km/s]	Shear Sound Speed [km/s]
1050 Aluminum Alloy (Al)	2.704±0.013	6.456±0.008	3.141±0.014
C101 Copper (Cu)	8.931±0.038	4.825±0.028	2.257±0.033
Lithium Fluoride (LiF)	2.64[2,3]	6.580±0.028	——[3]

As mentioned earlier, the tilt crystal orientation of Mo single crystals and LiF [100] windows were checked using X-ray Laue diffraction. Figure 3.5 shows the Laue diffraction images taken for Mo single crystals along [100], [111], and [110] orientations.

[1] Acoustic tensor corresponding to the wave propagation in the [110] orientation in a cubic crystal has three distinct eigenvalues.

[2] Theoretical density taken from Ref. [4]

[3] Archimedean method for the density measurement and cleaning process in the shear sound speed measurement involved water. Therefore, these measurements were not carried out for LiF.

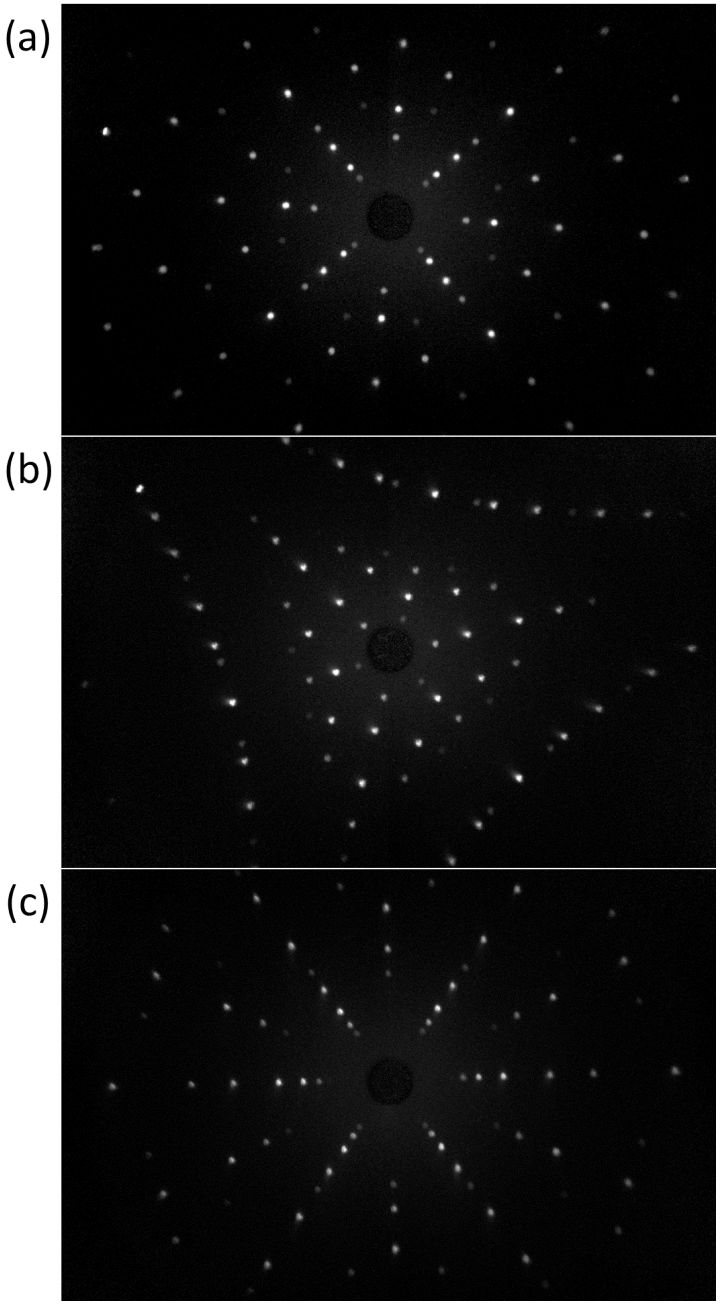

Figure 3.5: X-ray Laue diffraction images for Mo single crystals (a) along [100] orientation, (b) along [111] orientation, and (c) along [110] orientation. It is noted that these orientations are axes of 4-fold, 3-fold, and 2-fold symmetry, respectively.

3.3 Target Construction

A cross-sectional view of the target assembly is shown in Fig. 3.6. The front and back views of the actual target are shown in Fig. 3.7. For each target, a buffer, a Mo single crystal, and a LiF [100] window were prepared as described in Section

3.1. After components were prepared, they were bonded using 815 epoxy. First, the LiF window was bonded onto the Mo sample. The Mo/LiF assembly was pressed for 24 hours to allow the 815 epoxy to cure completely. Then, the assembly was bonded to the center of the buffer using a Teflon centering jig. The buffer/Mo/LiF assembly was pressed for 24 hours again. After each bonding step, the thickness of the epoxy layer was measured. The average of the total bonding thickness was 2.2 μ m. Then, the assembly was bonded onto a sample holder. A small amount of 815 epoxy was applied at the edge of recess of the sample holder. The assembly was slightly pressed in order to hold it in place, and not to bend the buffer.

In parallel to the sample preparation, a target ring, a target plate, and lens tube bracket (cf. Fig. 3.6) were lapped in order to remove marks from machining and to achieve parallel and flat surfaces. After the 815 epoxy cured, the sample assembly was screwed onto the target plate. On the other side of the target plate, the lens tube bracket was mounted using 3 screws 120 degrees apart. At each location of the screws, a brass spacer was placed in between to adjust the distance to the sample. Then, the target plate was mounted to a target ring, using 4 compressible Belleville washers at each location of the screws as the adjustable spacers. After the assembly, the front surface of the buffer was aligned parallel with the front surface of the target ring by adjusting the screws.

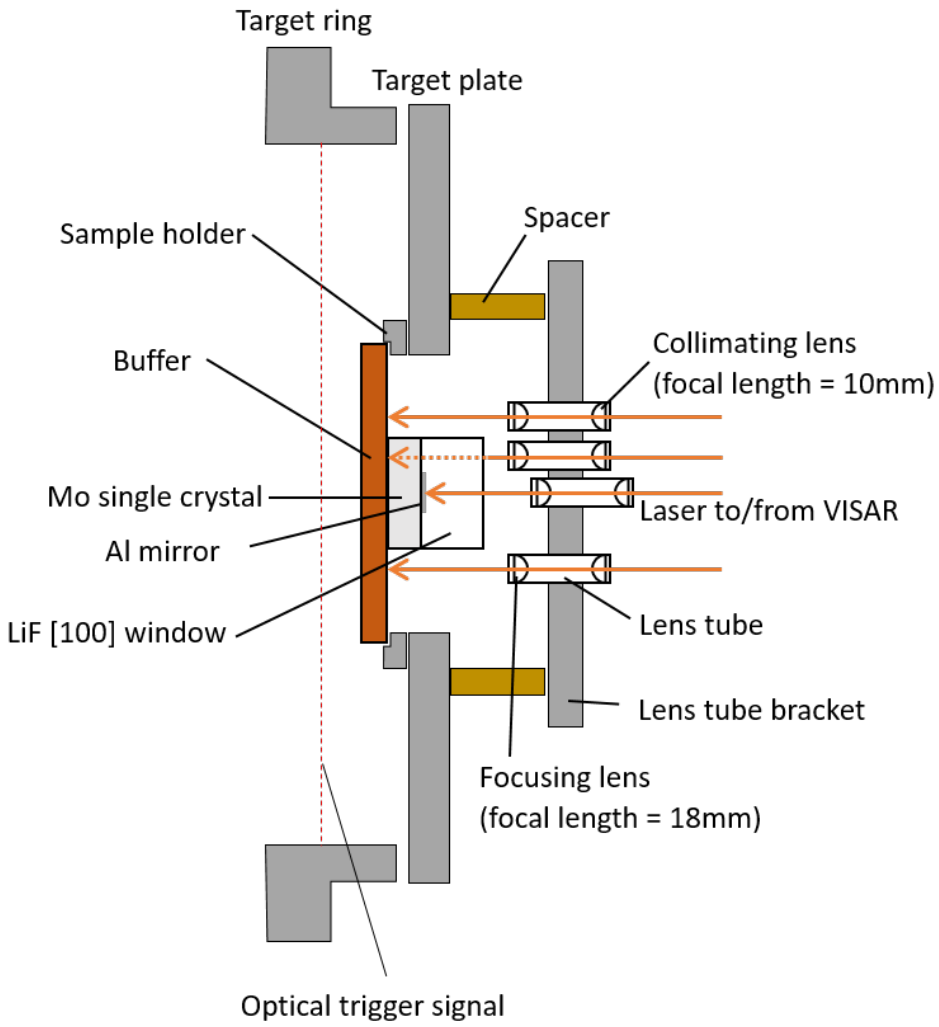

Figure 3.6: Schematic of the cross-section of the target assembly. Most of the experiments used optical trigger right in front of the buffer to detect the arrival of the impactor and to trigger the VISAR measurement. Some of the experiments using two-stage light gas gun utilized the optical signals from the impactor velocity measurement to trigger the VISAR measurement. The later setting was in the barrel of the gun and therefore not shown in this figure.

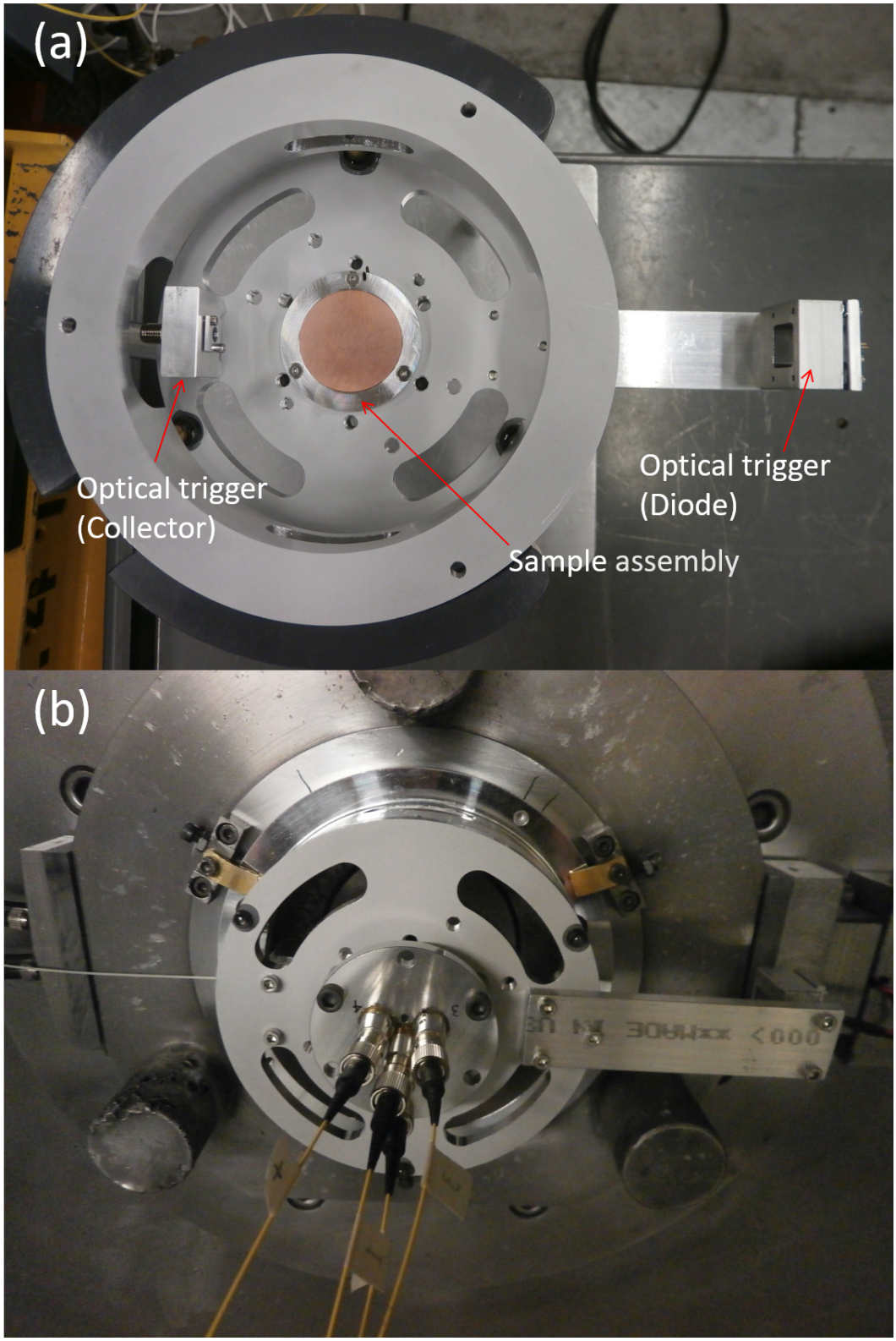

Figure 3.7: View of the target assembly (a) from the front side and (b) in the chamber of the two-stage light gas gun.

Optical Components

Four lens tubes for transmitting laser signals from/to VISAR were mounted to the threaded holes of the lens tube bracket. In each end of a lens tube, a collimating lens of 10 mm focal length and a focusing lens of 18 mm focal length were glued using 815 epoxy as shown in Fig. 3.6. The heights of the 3 outer lens tubes were adjusted so that the beam intensity of the return light was maximized. For the center lens tube, the height was adjusted according to the expected particle velocity of the Mo/LiF interface which corresponded to the impact stress. For the 23 GPa impact stress experiments, the height was adjusted so that the beam intensity of the return light was maximized. For the 190 GPa impact stress experiments, the center lens tube was unscrewed for 1 rotation (~600 μm). For the other experiments, the center lens tube was unscrewed for a half rotation (~300 μm). Once all the lens tubes were adjusted, 815 epoxy was applied to hold them secure in place.

After the 815 epoxy for the lens tubes cured, the locations of 4 VISAR probes were measured. The tilt of the impact and the arrival time of the shock at the center of the front surface of a Mo sample were calculated from the arrival times at three outer probes and their relative locations. The probe locations were measured using a dummy sample which is shown in Fig. 3.8. The dummy sample consisted of a soda-lime glass that had the same diameter as a buffer, an Al disc that had the same diameter as a Mo sample, and white burn paper on the surface. Each component was glued together using double-sided tape, and the assembly was pushed into a sample holder. The thickness of the Al disc was determined so that the thickness became equal to the effective height of the Al mirror due to the refraction in LiF optical window. The effective height was calculated from

$$\text{Effective height} = t_{\text{sample}} + t_{\text{window}}(1 - \frac{1}{n}) \tag{3.1}$$

where $n = 1.39$ is the refractive index of LiF [5], and t represents the thickness of each component. The dummy sample was mounted onto the target plate instead of an actual sample. Then, the laser lights with constant intensity were sent through 4 VISAR probes for 10~15 seconds to produce burn marks on the burn paper. The location of each burn mark was measured under a microscope.

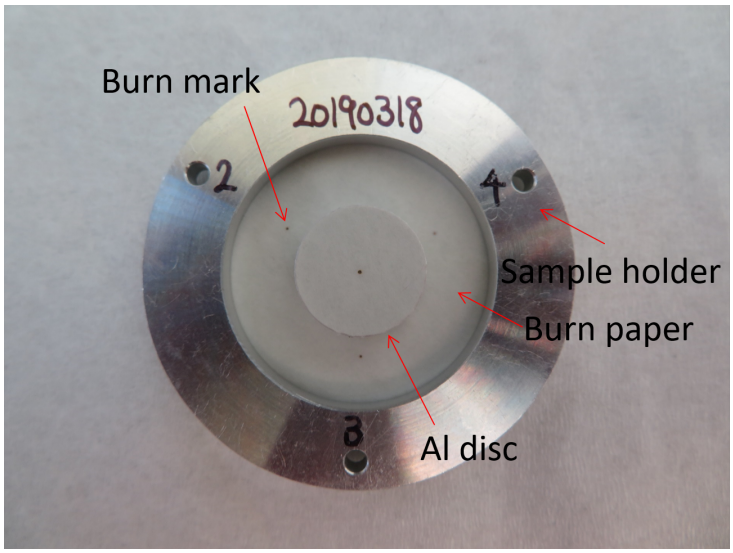

Figure 3.8: Dummy target used for measuring VISAR probe locations.

3.4 Instrumentation

Laser Interferometry

In each experiment, a multi-point VISAR system and a single-point VISAR system were used to record the particle velocity. Light from a 532 nm coherent laser was transmitted to the target, and reflected lights were collected using four custom-made 200 μm core optical fibers connected to each lens tube as shown in Fig. 3.7(b). The return signals from the center probe were split into two and sent to both of the multi-point VISAR system and the single-point VISAR system having different velocity per fringe (VPF) constants. By using this dual-VPF configuration [6], particle velocity measurements avoided complications due to any fringe loss. The etalon length and the VPF constants for the experiments are shown in Table 3.4. The return signals from the 3 outer probes were sent to the multi-point VISAR system. For the multi-point VISAR system, the time of travel for the laser light to the target in each channel was measured. This information was used to synchronise the measured velocity profiles from the 4 probes.

Table 3.4: Etalon length and the velocity per fringe (VPF) constants in each experiment

Impact Stress	Multi-point VISAR		Single-point VISAR	
	Etalon Length	VPF	Etalon Length	VPF
[GPa]	[cm]	[km/s/fringe]	[cm]	[km/s/fringe]
23	16.34	0.1724	10.307	0.2663
67	8.176	0.3298	6.251	0.4225
90	6.251	0.4225	4.133	0.6067
110	4.133	0.6067	2.118	1.036
190	6.251	0.4225	4.113	0.6067

The return signals were recorded using Tektronix DPO 70804 (8 GHz bandwidth, 25×10^9 samples/s) oscilloscope in the multi-point VISAR system, and using Tektronix TDS 6804B (8 GHz bandwidth, 20×10^9 samples/s) oscilloscope in the single-point VISAR system. The outputs from the beam intensity monitor (BIM) were recorded using Tektronix DPO 7254C (2.5 GHz bandwidth, 40×10^9 samples/s) oscilloscope, along with the output from the optical trigger which is described in the following subsection.

Optical Trigger

As shown in Fig. 3.6, except for some experiments using the two-stage light gas gun, optical trigger was used to trigger the VISAR measurement. Optical trigger consisted of two components shown in Fig. 3.7 (a). The diode emitted laser light which was focused at the collector which was on the other side of the target. The laser light from the collector was transmitted to a photo diode amplifier using a custom-made 400 μm core optical fiber. When the impactor arrives at the location of the optical trigger, it blocks the laser light going into the collector. Thus, arrival of the impactor corresponds to the drop in the voltage of the output from the photo diode amplifier. The negative change in the voltage was used to trigger the VISAR measurement. The location of the optical trigger measured from the surface of the buffer was set to be more than ($3\ \mu\text{s} \times v_{\text{projectile}}$) in order to allow time for VISAR to stabilise after triggered.

References

[1] L. M. Barker and R. E. Hollenbach. “Laser interferometer for measuring high velocities of any reflecting surface.” In: *Journal of Applied Physics* 43.11 (1972), p. 4669.

[2] L. M. Barker and K. W. Schuler. “Correction to the velocity-per-fringe relationship for the VISAR interferometer.” In: *Journal of Applied Physics* 45.8 (1974), p. 3692.

[3] J. N. Johnson. “Shock propagation produced by planar impact in linearly elastic anisotropic media.” In: *Journal of Applied Physics* 42.13 (1971), p. 5522.

[4] Kurt J. Lesker Company. *Lithium Fluoride LiF Powder & Pieces Evaporation Materials.* `https://www.lesker.com/newweb/deposition_materials/depositionmaterials_evaporationmaterials_1.cfm?pgid=li2`. [Online; accessed 2019 November 11].

[5] H. H. Li. “Refractive index of alkali halides and its wavelength and temperature derivatives.” In: *Journal of Physical and Chemical Reference Data* 5.2 (1976), p. 329.

[6] D. H. Dolan. “Foundations of VISAR analysis.” In: *Sandia National Laboratories Report* (2006), SAND2006–1950.

Chapter 4

EXPERIMENTAL RESULTS

This chapter presents the results of the plate impact experiments on Mo single crystals along three different orientations. First, the experimental parameters are summarized in Section 4.1. Then, the measured velocity profiles near the elastic limit are presented in Sections 4.2 and 4.3. Lastly, Section 4.4 summarizes the observations at the peak state.

4.1 Experimental Parameters

The experimental configuration is schematically shown in Fig. 4.1. The target construction is shown in Fig. 3.6 in the previous chapter.

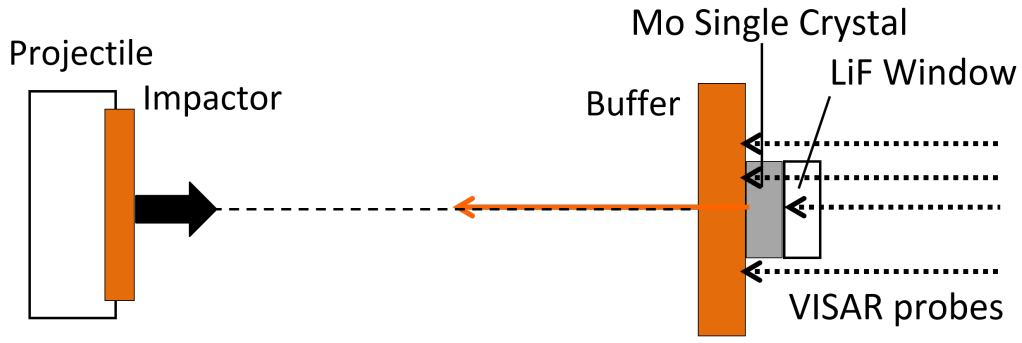

Figure 4.1: Schematic of the plate impact experimental configuration.

Figure 4.2 shows the schematic of time (t) - distance (x) plot. Upon impact, overdriven, single wave propagated into the buffer and the impactor. The impactor and the buffer were chosen to be the same material, either Al or Cu, to achieve a symmetric impact. When the forward propagating shock in the buffer was incident on the buffer - Mo sample interface, either one (overdriven) or two shock waves propagated into the Mo sample, depending on the impact stress. For the case of the overdriven shock wave, the peak state was achieved behind the shock wave. When transmitted plastic shock wave interacted with the Mo sample - LiF window interface, that resulted in a release wave in the Mo sample.

For the case of two shock waves, the elastic limit was achieved behind the leading elastic shock wave, and the peak state was achieved behind the trailing plastic shock

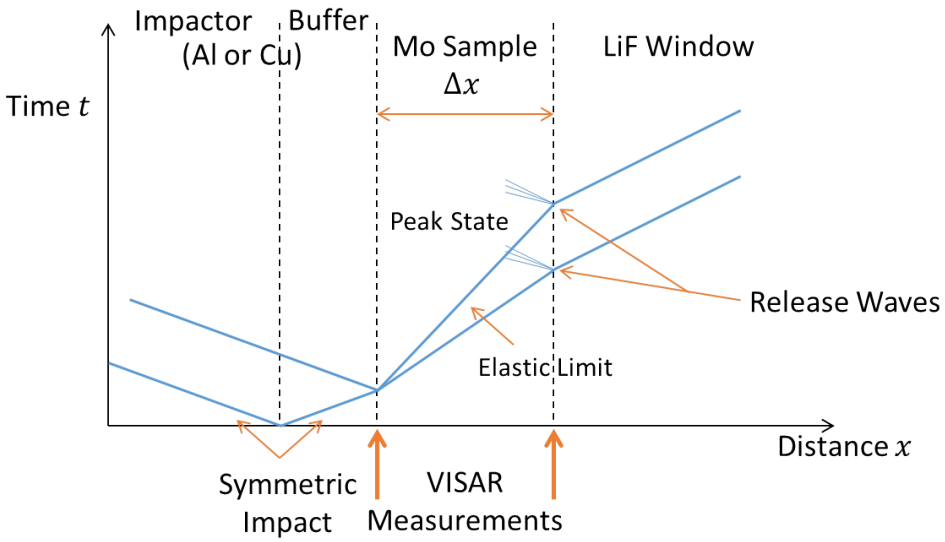

Figure 4.2: Schematic time(t) - distance(x) plot for the plate impact experiments.

wave. The transmitted elastic and plastic shock waves in Mo sample later interacted with the Mo sample - LiF window interface, and each interaction resulted in a release wave propagating back into the Mo sample. The locations of arrows in Fig. 4.2 correspond to the location of velocity measurements using VISAR [1, 2]. The time differences of the arrivals of shock waves were used to determine the shock wave velocities.

As shown in Fig. 4.2, for the case of two shock waves, the reflected release wave resulting from the elastic shock wave interacted with the trailing plastic shock wave. In the analysis, this effect was not directly considered, but the associated error was taken into account when the in-material quantities at the peak state were calculated. This is described later in Section 5.1.

The experimental parameters are shown in Table 4.2. Elastic impact stress in the table corresponds to the amplitude of longitudinal stress, calculated assuming that Mo single crystal stays elastic. Elastic impact stress provides a convenient way to compare results for different crystal orientations. The elastic Hugoniot relation for Mo single crystals [3, 4] constructed based on finite elasticity [5], and known Hugoniot relations [6–8] were used in the elastic impact stress calculations. The principal Hugoniot relations used in the calculation are summarized in Table 4.1.

Table 4.1: Hugoniot relations for each material

Material	Hugoniot Relation	Reference
Mo[100]	$\sigma_x = 69.039u_p + 11.046u_p^2$	[3]
Mo[111]	$\sigma_x = 64.724u_p + 21.319u_p^2$	[4]
Mo[110]	$\sigma_x = 65.829u_p + 17.759u_p^2$	[4]
Al	$U_s = 5.35 + 1.32u_p$	[6]
Cu	$U_s = 3.97 + 1.479u_p$	[7]
LiF[100]	$U_s = 5.15 + 1.35u_p$	[8]

As shown in Table 4.2, a total of 20 experiments were conducted in this study. Projectile velocities were systematically varied to achieve approximately 23, 67, 90, 110, and 190 GPa impact stresses for each orientation. Experiments along [100] orientation are denoted as A1 - A7; experiments along [111] orientation are denoted as B1 - B8; experiments along [110] orientation are denoted as C1 - C5. Experiments (A2,A3), (A5,A6), and (B1,B2) represent pairs of repeat experiments to check reproducibility. The sample thickness was kept constant at nominally 2 mm, except for experiments B7 and B8 which used thicker 3.5 mm samples. As in Table 3.1, the projectiles were launched using a powder gun in experiments A1 - A3, B1 - B3, and C1 - C2. A two-stage light gas gun was used in the remainder of the experiments.

Table 4.2: Experimental parameters for the plate impact experiments

Exp. Number	Loading Direction	Sample Thickness [mm]	Impactor/ Buffer Material	Impactor Thickness [mm]	Buffer Thickness [mm]	Window Thickness [mm]	Impact Velocity [km/s]	Elastic Impact Stress [GPa]	Impact Tilt [mrad]
A1	[100]	2.019	1050Al	1.831	0.956	6.366	1.549	23.2	0.392
A2		2.010	C101Cu	1.717	0.924	6.363	2.099	65.7	2.61
A3		2.011	C101Cu	1.686	0.921	6.363	2.113	66.2	1.27
A4		2.030	C101Cu	3.058	0.921	6.362	2.680	89.1	3.05
A5		2.027	C101Cu	1.094	0.926	6.346	3.126	108.6	2.32
A6		2.030	C101Cu	1.109	0.923	6.397	3.291	116.1	4.80
A7		2.022	C101Cu	3.086	0.932	6.368	4.637	183.9	1.94
B1	[111]	2.027	1050Al	1.842	0.915	6.366	1.595	23.9	0.55
B2		2.029	1050Al	1.803	0.916	6.342	1.599	24.0	0.30
B3		2.009	C101Cu	1.704	0.928	6.364	2.106	67.4	0.97
B4		2.043	C101Cu	3.052	0.925	6.055	2.710	93.7	4.99
B5		2.027	C101Cu	1.101	0.927	6.344	3.149	114.6	3.18
B6		2.034	C101Cu	3.049	0.931	6.117	4.634	197.5	3.07
B7		3.499	C101Cu	1.102	0.921	6.362	2.806	98.1	8.76
B8		3.497	C101Cu	1.111	0.922	6.399	3.122	113.3	1.89
C1	[110]	2.021	1050Al	1.778	0.909	6.365	1.571	23.5	0.61
C2		2.018	C101Cu	1.708	0.934	6.360	2.110	67.0	1.28
C3		2.032	C101Cu	3.047	0.944	6.053	2.676	90.9	3.91
C4		2.029	C101Cu	1.097	0.920	6.054	3.151	112.9	4.33
C5		2.040	C101Cu	3.013	0.940	6.117	4.639	193.1	3.30

4.2 Measured Velocity Profiles near the Elastic Limit

In this section, the measured velocity profiles near the elastic limit at different impact stresses are compared, and the findings for each orientation are summarized.

The measured velocity profiles near the elastic limit for 2 mm thick samples along [100], [111], and [110] orientations are shown in Figs. 4.3, 4.4, and 4.5, respectively. In each plot, the time is divided by the sample thickness to compensate for slight differences in sample thicknesses, to enable elastic shock velocity comparisons between experiments. Since this section focuses on the observations at the elastic limit, results from experiments with overdriven, single shock waves are not shown in Figs. 4.3 - 4.5. This section presents the results for 2 mm thick sample experiments, and the results for the 3.5 mm thick samples (B7,B8) are presented in Section 4.3.

The elastic shock velocity and the measured particle velocity at the elastic limit are summarized in Table 4.3 along with the measurement at the peak state.

Table 4.3: Measured quantities in plate impact experiments

Exp. Number	Loading Direction	Sample Thickness [mm]	Elastic Impact Stress [GPa]	Elastic Limit		Peak State	
				Elastic Shock Velocity [km/s]	Measured Particle Velocity [km/s]	Plastic Shock Velocity [km/s]	Measured Particle Velocity [km/s]
A1	[100]	2.019	23.2	6.79±0.17	0.0954±0.001	5.38±0.11	0.588±0.006
A2		2.010	65.7	6.76±0.14[1]	0.0877±0.001	6.15±0.12[1]	1.40±0.02
A3		2.011	66.2	6.82±0.14[1]	0.0975±0.001	6.20±0.12[1]	1.41±0.02
A4		2.030	89.1	6.87±0.07	0.103±0.002	6.57±0.07	1.80±0.02
A5		2.027	108.6	6.99±0.13[2]	0.119±0.002	6.85±0.12[2]	2.10±0.03
A6		2.030	116.1	7.01±0.13[2]	0.0963±0.001	6.96±0.12[2]	2.22±0.03
A7		2.022	183.9	(Overdriven)		7.75±0.15[3]	3.16±0.04
B1	[111]	2.027	23.9	6.52±0.15	0.172±0.002	5.39±0.10	0.602±0.007
B2		2.029	24.0	6.58±0.15	0.167±0.002	5.42±0.11	0.605±0.007
B3		2.009	67.4	6.59±0.13[1]	0.187±0.002	6.17±0.12[1]	1.40±0.02
B4		2.043	93.7	6.73±0.07	0.198±0.002	6.63±0.07	1.81±0.02
B5		2.027	114.6	6.96±0.12[2]	0.214±0.003	6.89±0.12[2]	2.12±0.03
B6		2.034	197.5	(Overdriven)		7.84±0.16[3]	3.16±0.04
B7		3.499	98.1	6.79±0.04	0.199±0.002	6.68±0.04	1.88±0.02
B8		3.497	113.3	6.98±0.07[2]	0.200±0.002	6.91±0.07[2]	2.11±0.03
C1	[110]	2.021	23.5	6.48±0.15	0.0999±0.001	5.51±0.11	0.592±0.006
C2		2.018	67.0	6.42±0.13[1]	0.104±0.002	6.17±0.12[1]	1.41±0.02
C3		2.032	90.9	6.63±0.07	0.106±0.002	6.59±0.07	1.78±0.02
C4		2.029	112.9	(Overdriven)		6.91±0.12[2]	2.12±0.03
C5		2.040	193.1	(Overdriven)		7.88±0.16[3]	3.16±0.04

[100] orientation

Figure 4.3 shows that in experiments A1 - A6, the two-wave structure – an elastic wave trailed by a plastic wave - were observed. In all of the velocity profiles shown in Fig. 4.3, a relaxation behind the elastic wave was observed. This is an indication of the time dependence of deformation [9]. Except for A2, the elastic shock velocity increased with increasing impact stress. Also, the measured particle velocity at the elastic limit followed the same trend.

In experiment A2, the measured particle velocity at the elastic limit and the corresponding in-material quantities which are discussed in Chapter 5 were not consistent with the other [100] experiments and the difference between the repeat experiment A3 was beyond the experimental uncertainties. Experiment A2 is therefore not included in further discussions.

In experiment A5, during the unloading behind the elastic wave, an abrupt drop in the particle velocity was observed. This abrupt drop was not observed in the repeat experiment A6, nor in other experiments. Therefore, this anomalous experiment is not included in the detailed discussion.

Those inconsistencies might be attributed to the scatter between samples, but we cannot conclusively determine the cause. It is noted that larger scatter between [100] oriented samples was also reported for the case of shock compression to lower stresses [3, 10].

---

[1] Impactor bowing correction of 4.1± 2 ns is applied.
[2] Impactor bowing correction of 2.0± 2 ns is applied.
[3] Impactor bowing correction of 29± 2 ns is applied.

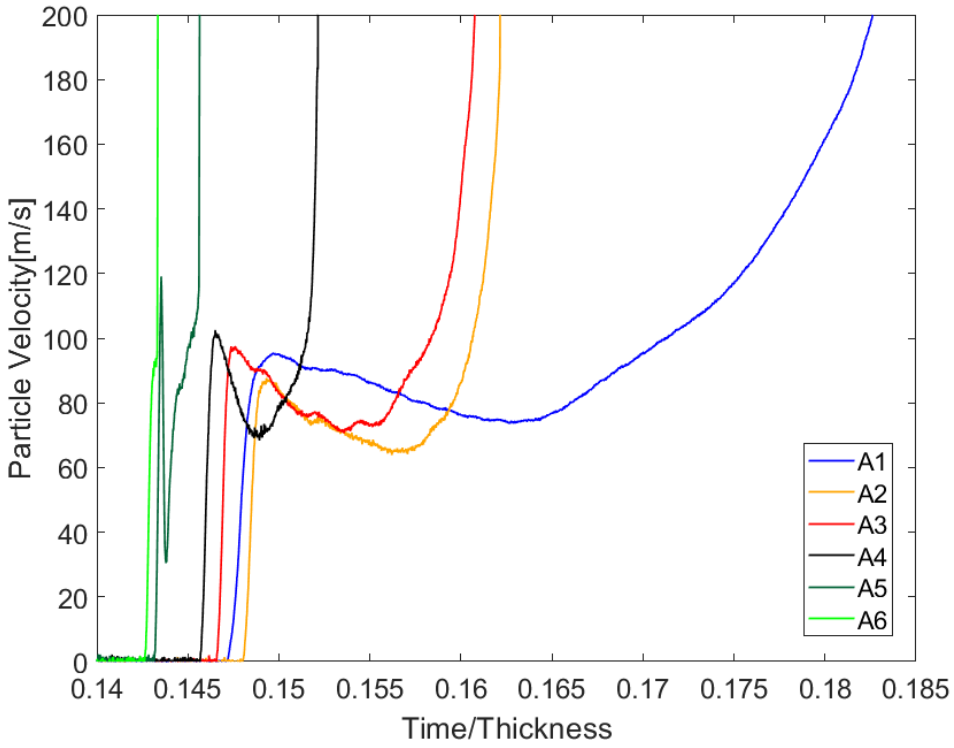

Figure 4.3: Measured particle velocity near the elastic limit for the [100] orientation.

[111] orientation

Figure 4.4 shows that in experiments B1 - B5, a two-wave structure was observed. Similar to the [100] orientation, the particle velocity at the elastic limit increased as the elastic impact stress increased. Also, the relaxation behind the elastic wave was observed, which was an indication of the time dependence. Regarding experiment B1 and the corresponding repeat experiment B2, the results were well reproduced. In these two experiments at 23 GPa impact stress, considerable kinks were observed between the elastic and plastic shock waves around time/thickness = 0.18, apart from the relaxation. There were some differences observed in the features between the elastic and the plastic shock wave, but the elastic shock velocities and the particle velocity at the elastic limit were within the experimental uncertainties.

Compared to the [100] and [110] orientations, the measured particle velocity at the elastic limit was significantly higher along the [111] orientation. This observation was consistent with the lower stress shock studies on Mo single crystals [3, 4, 10].

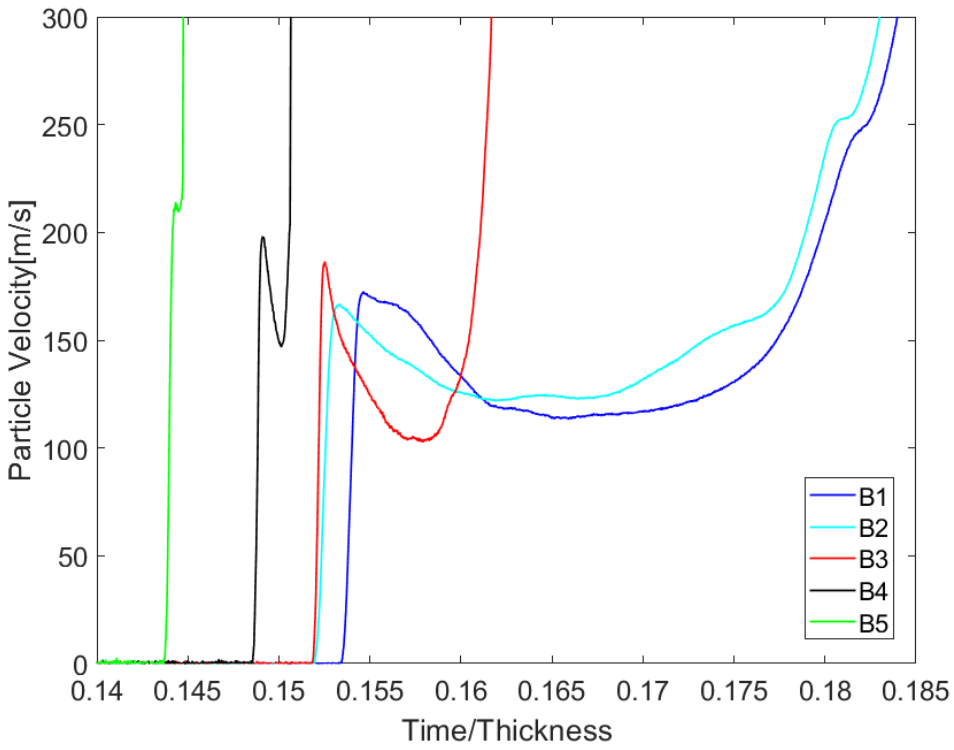

Figure 4.4: Measured particle velocity near the elastic limit for the [111] orientation.

[110] orientation

Figure 4.5 shows that in experiments C1 - C3, a two-wave structure was again observed. Along the [110] orientation, the two-wave structure was only observed up to 90 GPa impact stress. This observation is different from the other orientations. In all of the velocity profiles shown in Fig. 4.5, the relaxation behind the elastic limit was observed, but in experiment C3, there was only a slight relaxation due to the small time separation between the elastic and the plastic shock waves. In experiment C1, a kink was observed during the rise of the plastic shock wave, around time/thickness = 0.175. The measured particle velocity at the elastic limit slightly increased with increasing impact stress. The dependence on the impact stress was smaller along the [110] orientation.

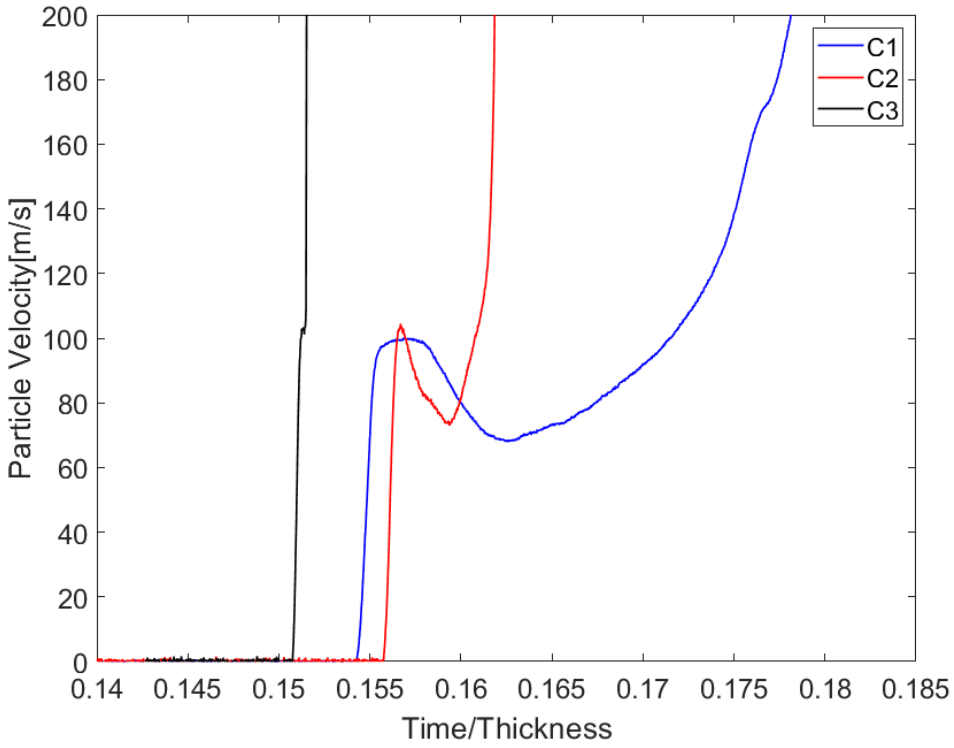

Figure 4.5: Measured particle velocity near the elastic limit for the [110] orientation.

4.3 3.5 mm Thick Sample Experiments along [111] Orientation

The measured wave profiles for 3.5 mm thick sample experiments along the [111] orientation (experiments B7 and B8), are shown in Fig. 4.6. For comparison, the measured velocity profiles for the 2 mm thick sample experiments (B4,B5) with nominally the same impact stresses are shown in Fig. 4.7. Note that time units are in μs.

By comparing Figs. 4.6 and 4.7, one can observe the difference in the profiles during the release behind the elastic wave. This is an effect of the time separation between the two waves (elastic and plastic shock waves) due to the difference in the thicknesses of the samples. The measured particle velocity at the elastic limit was comparable in the 90 GPa impact stress experiments (B4 and B7). However, for 110 GPa impact stress experiments (B5 and B8), the measured particle velocity at the elastic limit was lower in the 3.5 mm thick sample experiment B8.

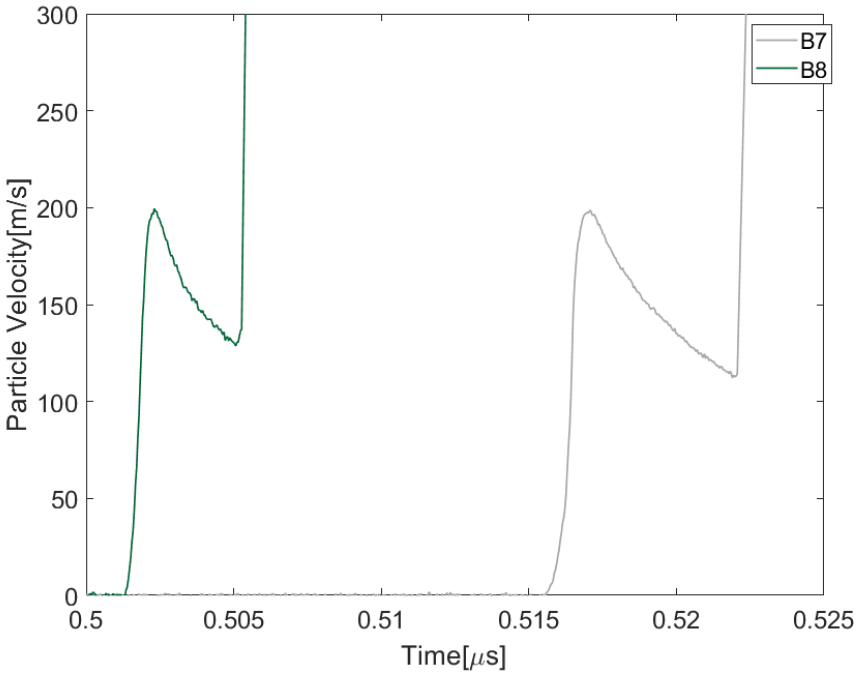

Figure 4.6: Measured particle velocity in 3.5 mm thick sample experiments along the [111] orientation.

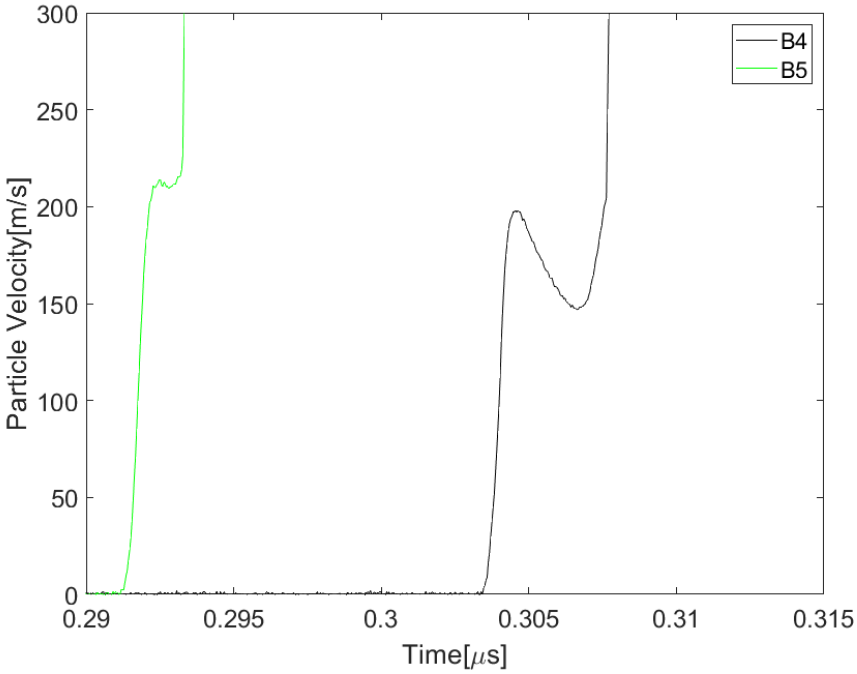

Figure 4.7: Comparison of 3.5 mm thick sample experiments with corresponding 2 mm thick sample experiments.

4.4 Observation at the Peak State

In this section, the full view of the measured velocity profiles for 2 mm thick samples are compared between different impact stresses. As in Figs. 4.3 - 4.5, the time is divided by the sample thickness. The measured velocity profiles along [100], [111], and [110] orientations are shown in Fig. 4.8, 4.9, and 4.10, respectively.

The plastic shock velocity (Lagrangian) and the measured particle velocity behind the plastic shock wave are summarized in Table 4.3.

[100] orientation

Figure 4.8 shows that in experiments A1 - A6, the two-wave structure – an elastic wave trailed by a plastic shock wave - was observed. The single wave structure was observed only in A7. As mentioned in Section 4.2, experiments A2 and A5 are excluded from the further discussion due to the anomalous behavior observed at the elastic limit. In Fig. 4.8, one can observe that the particle velocity behind the plastic shock wave and the plastic shock velocity increased with the increasing impact stress.

[111] orientation

Figure 4.9 shows that in experiments B1 - B5, the two-wave structure was observed. The single wave structure was observed only in B6. As seen in the experiments along the [100] orientation, the particle velocity behind the plastic shock wave and the plastic shock velocity increased with the increasing impact stress. Regarding experiment B1 and the corresponding repeat experiment B2, the results were well reproduced.

[110] orientation

Figure 4.10 shows that in experiments C1 - C3, the two-wave structure was observed. The single wave structure was observed in C4 and C5. This observation differs from the experiments along the other orientations. However, the particle velocity behind the plastic shock wave and the plastic shock velocity followed the same trend as in the other orientations; they increased with increasing impact stress.

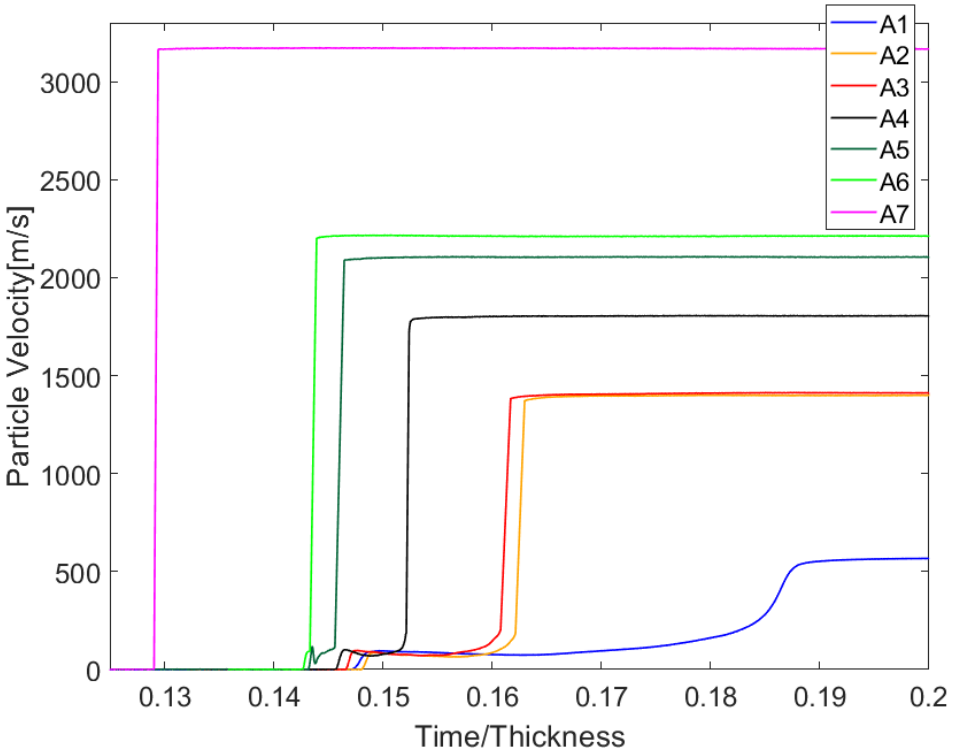

Figure 4.8: Measured particle velocity along the [100] orientation.

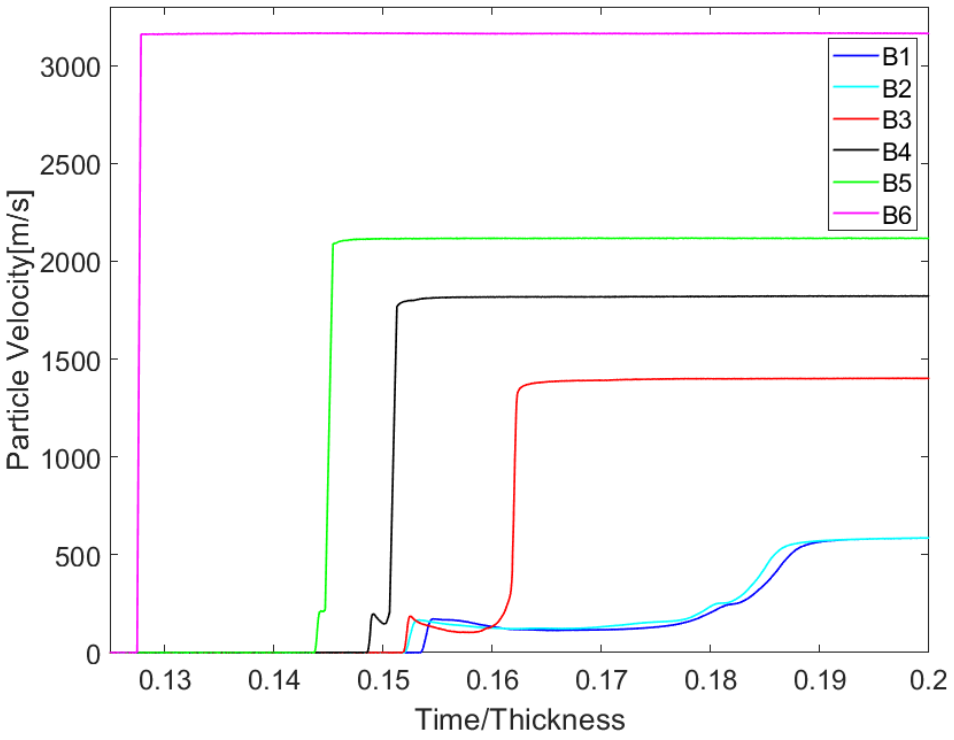

Figure 4.9: Measured particle velocity along the [111] orientation.

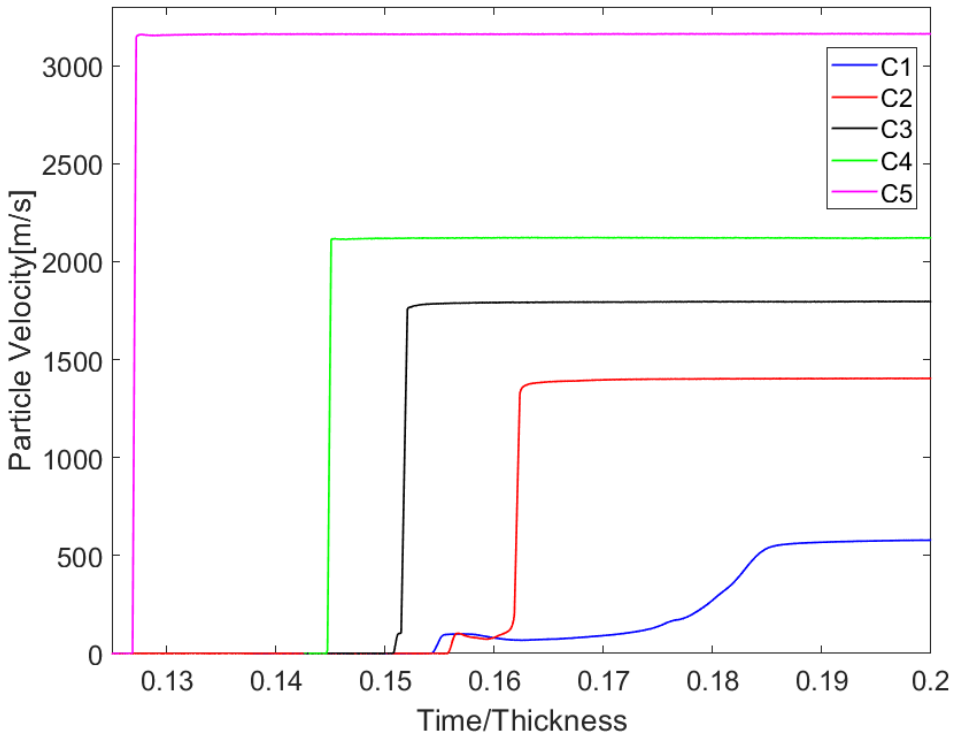

Figure 4.10: Measured particle velocity along the [110] orientation.

Comparison between three orientations

The plastic shock velocity and the measured particle velocity behind the plastic shock wave for the three orientations are shown in Table 4.3. One can see that, for each impact stress, the plastic shock velocities and the measured particle velocities along three orientations agree within experimental uncertainties. For the 23 GPa impact stress experiments (A1, B1, B2, and C2), if one compares experiments A1 and C1, the measured values at the peak state differ by the maxima of experimental uncertainties. For the 66 GPa - 190 GPa impact stress experiments, measured values at the peak state along three orientations agree well within the experimental uncertainties, except for the measured particle velocity for experiment A6. This might be attributed to the scatter between samples similar to the observation at the elastic limit, but we cannot conclusively determine the cause.

4.5 Reproducibility of Experiments

In two experiments along [111] orientation at 23 GPa impact stress, B1 and B2, the shock velocities and the measured particle velocity at each state were within experimental uncertainties. In Fig. 4.11, the whole velocity profiles were compared

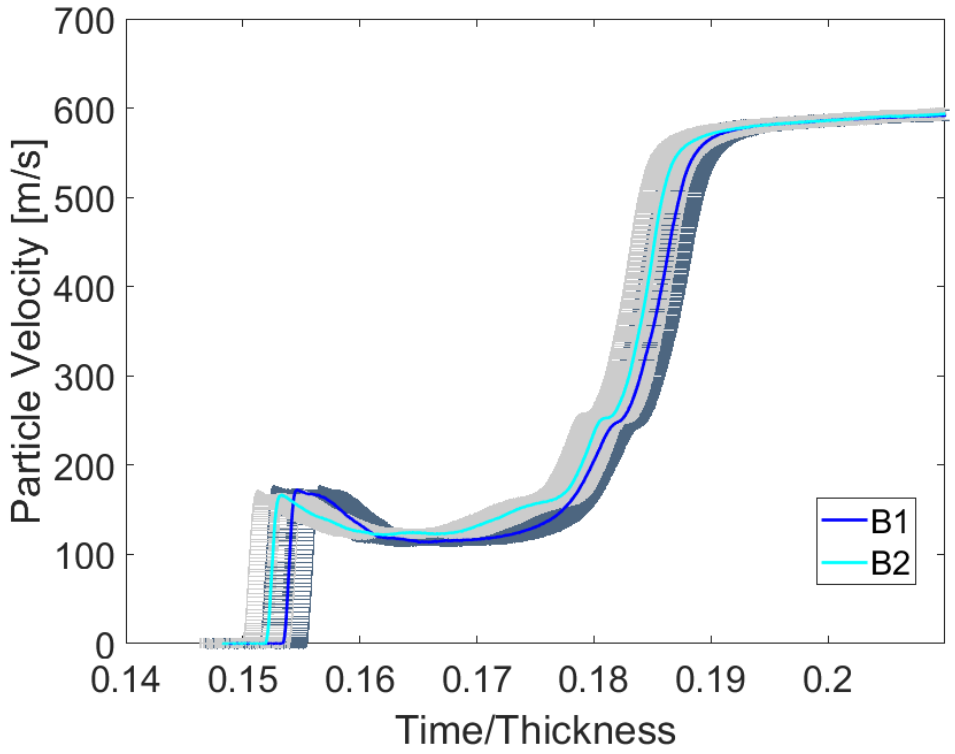

Figure 4.11: Comparison of velocity profiles in experiments B1 and B2. Error bars are superposed to each measured value.

between experiments B1 and B2. The main source of uncertainty in time is the time resolution of VISAR (~3 ns in these experiments) and the time of travel of laser signal in VISAR (~1 ns). The main source of uncertainty in the particle velocity is the uncertainty in the calibration of VPF constant of VISAR (±1%). These uncertainties are superposed to the measured velocity profiles in Fig. 4.11. The figure shows that, for experiments B1 and B2, the velocity profiles until the elastic limit and after the arrival of plastic shock wave agreed within experimental uncertainties. There was a slight difference in the velocity profiles during the relaxation behind the elastic shock wave. This is the scatter between experiments, and is attributed to difference in the condition of samples such as slight variation in surface roughness and dislocation density due to sample preparation.

4.6 Summary

The significant findings from the experiments on Mo single crystals along the three orientations are summarized below.

Observations at the elastic limit:

- Along the [100] and [111] orientations, the two-wave structure was observed up to 110 GPa impact stress. Along the [110] orientation, the two-wave structure was observed only up to 90 GPa impact stress. When the two-wave structure was observed, the relaxation behind the elastic wave was observed, which is an indication of time dependence.
- Along all three orientations, elastic shock velocity increased with increasing impact stress. The measured particle velocity at the elastic limit followed the same trend.
- The measured particle velocity at the elastic limit was significantly larger along the [111] orientation than the other orientations.
- Larger scatter between samples was observed in the experiments along the [100] orientation.
- For the 3.5 mm thick sample experiments along the [111] orientation, the measured particle velocity at the elastic limit was lower than that for the 2 mm thick sample experiment at 110 GPa impact stress.

Observations at the peak state:

- Along all three orientations, the particle velocity behind the plastic shock wave and the plastic shock velocity increased with the increasing impact stress.
- The difference between three orientations in measured values at the peak state were within experimental uncertainties, except for the measured particle velocity for experiment A6.
- The anisotropic effect did not manifest in terms of the plastic shock velocity and the measured particle velocity.

References

[1] L. M. Barker and R. E. Hollenbach. “Laser interferometer for measuring high velocities of any reflecting surface.” In: *Journal of Applied Physics* 43.11 (1972), p. 4669.

[2] L. M. Barker and K. W. Schuler. “Correction to the velocity-per-fringe relationship for the VISAR interferometer.” In: *Journal of Applied Physics* 45.8 (1974), p. 3692.

[3] A. Mandal and Y. M. Gupta. “Elastic-plastic deformation of molybdenum single crystals shocked along [100].” In: *Journal of Applied Physics* 121.4 (2017), p. 045903.

[4] A. Mandal and Y. M. Gupta. “Elastic-plastic deformation of molybdenum single crystals shocked to 12.5 GPa: Crystal anisotropy effects.” In: *Journal of Applied Physics* 125.5 (2019), p. 055903.

[5] Y. M. Gupta. “Effect of crystal orientation on dynamic strength of LiF.” In: *Journal of Applied Physics* 48.12 (1977), p. 5067.

[6] D. Choudhuri and Y. M. Gupta. “Shock compression and unloading response of 1050 aluminum to 70 GPa.” In: *AIP Conference Proceedings*. Vol. 1426. 1. AIP. 2012, p. 755.

[7] M. D. Knudson and M. P. Desjarlais. “Adiabatic release measurements in α-quartz between 300 and 1200 GPa: Characterization of α-quartz as a shock standard in the multimegabar regime.” In: *Physical Review B* 88.18 (2013), p. 184107.

[8] W. J. Carter. “Hugoniot equation of state of some alkali halides.” In: *High Temperatures - High Pressures* 5 (1973), p. 313.

[9] L. Davison. *Fundamentals of shock wave propagation in solids.* Springer Science & Business Media, 2008.

[10] A. Mandal. “Elastic-Plastic Deformation of Molybdenum Single Crystals Shocked to 12.5 GPa.” PhD thesis. Washington State University, School of Mechanical and Materials Engineering, 2016.

Chapter 5

ANALYSIS AND DISCUSSION

In this chapter, the results from the plate impact experiments presented in Chapter 4 are analyzed. For each experiment, in-material particle velocity, longitudinal stress, and density were calculated at the elastic limit and the peak state based on an approach similar to impedance matching procedures and the Rankine-Hugoniot jump conditions used previously [1–3]. In-material particle velocity, longitudinal stress, and density are referred to as the in-material quantities. Section 5.1 describes the method used to calculate the in-material quantities. Based on the calculated in-material quantities, the analysis at the elastic limit in the 2 mm thick sample experiments is presented in Sections 5.2 - 5.3. The results from the 3.5 mm thick sample experiments are compared with the corresponding 2 mm thick sample experiments in Section 5.4. The analysis of the peak state is presented in Sections 5.6 - 5.8. Section 5.7 also compares the results with polycrystalline Mo Hugoniot relations [4].

5.1 Calculation of In-material Quantities

In order to calculate the in-material quantities at the elastic limit and the peak state, the measured velocity profiles were idealized as a one-step function or a two-step function as shown in Fig. 5.1. Because of this assumption, the time dependence was not considered in the calculation of the in-material quantities. In the analysis in this section, the internal energy appearing in Eq. 2.3 was not of particular interest.

For the case of overdriven wave

When the overdriven, single wave is observed, based on Eqs. 2.1 and 2.2, the shock jump conditions for the states in Mo single crystal can be written as follows:

$$\rho^{pl}(U_{Eu}^{pl} - u^{pl}) = \rho_0 U_{Eu}^{pl} \tag{5.1}$$

$$\sigma_x^{pl} = \rho_0 U_{Eu}^{pl} u^{pl} \tag{5.2}$$

where U_{Eu} is the Eulerian shock velocity. Since there is only one shock wave, the Eulerian velocity is the same as the Lagrangian velocity, and is given by the transit

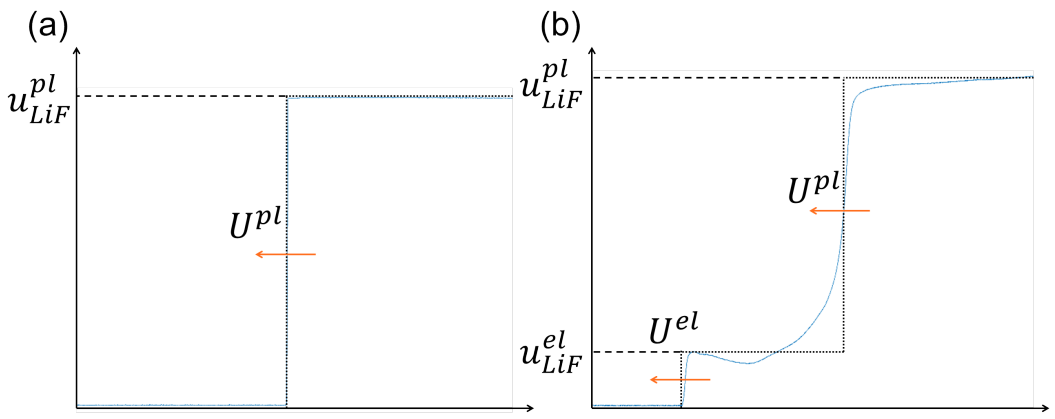

Figure 5.1: Idealization of the velocity profiles for (a) overdriven, single-shock wave and (b) two-wave structure.

time divided by the thickness. The superscript *pl* corresponds to the quantities at the peak state.

Figure 5.2 shows the P (longitudinal stress) - u (particle velocity) diagram for an experiment in which overdriven, single wave is observed. In the figure, the elastic part of Hugoniot relations are omitted for simplicity. Longitudinal stress at the peak state σ_x^{pl} is referred to as peak stress.

After the symmetric impact between the Cu impactor and the Cu buffer, the forward propagating shock interacted with the Cu buffer - Mo sample interface. The Cu buffer underwent reshock, and the peak state was achieved at the interface. Nellis *et al.* [5] showed that the reshock Hugoniot of Cu agrees well with the states represented an mirror image of the principal Hugoniot, within uncertainties of ~ 3%. In the calculation that follows, the following assumption was made.

- Reshock of Cu follows the mirror image of the principal Hugoniot around the first shocked state (State 1).

Also, the longitudinal stress at state in Cu (State 1) was closer to σ_x^{pl} than the state at Mo sample - LiF window interface (State 2). Therefore, the potential error introduced by the assumptions on reshock or release would be smaller when one calculates the peak state based on the State 1.

Based on the known Hugoniot relation for Cu shown in Table 4.1, the peak stress can be written as,

$$\sigma_x^{pl} = \rho_{Cu}(3.97 + 1.32(u_{Proj} - u^{pl}))(u_{Proj} - u^{pl}) \tag{5.3}$$

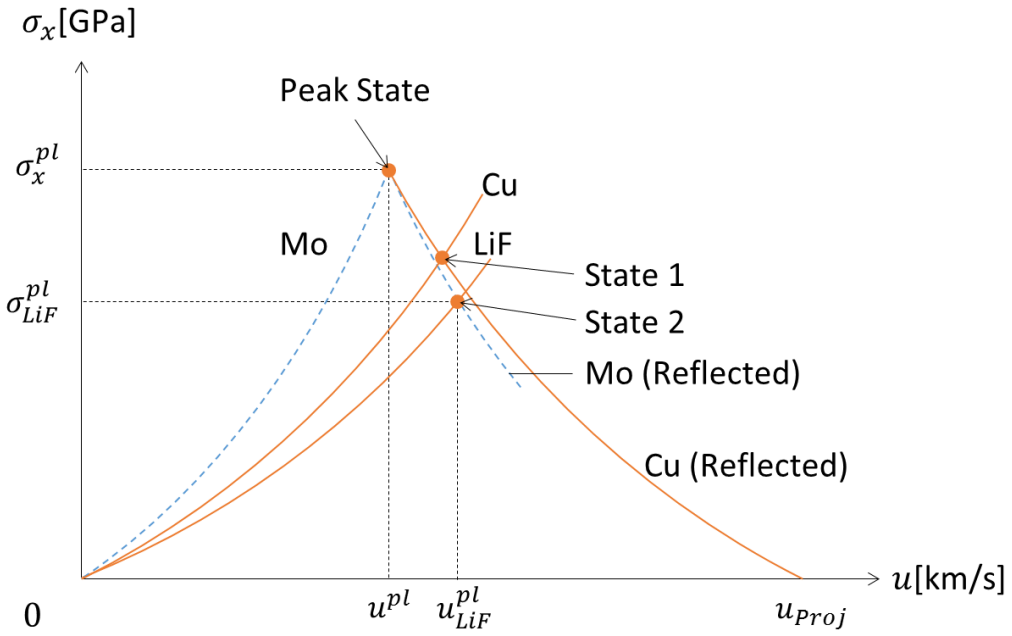

Figure 5.2: P - u diagram in a plate impact experiment with overdriven shock wave. For materials in which an overdriven shock wave is propagated, the corresponding elastic Hugoniot relations are omitted for simplicity. Orange solid line represents known Hugoniot relation, and blue dashed line represents unknown Hugoniot of the material of interest.

where ρ_{Cu} is the ambient density of Cu and u_{Proj} is the projectile velocity.

Alternately, based on Eq. 5.2, the peak stress can be written as,

$$\sigma_x^{pl} = \rho_0 U_{Eu}^{pl} u^{pl}. \tag{5.4}$$

In Eqs. 5.3 and 5.4, there are two unknowns: σ_x^{pl} and u^{pl}. By numerically solving Eqs. 5.3 and 5.4 simultaneously, the particle velocity at the peak state and the peak stress were determined. The density at the peak state was then calculated from Eq. 5.1.

For the case of two-wave structure

When the two-wave structure is observed, the shock jump conditions apply across the elastic shock and the plastic shock, and they relate three states in Mo single crystal sample. The shock jump conditions that hold across the elastic shock can be derived in the same manner as Eqs. 5.1 and 5.2.

$$\rho^{el}(U^{el}_{Eu} - u^{el}) = \rho_0 U^{el}_{Eu} \tag{5.5}$$

$$\sigma^{el}_x = \rho_0 U^{el}_{Eu} u^{el}. \tag{5.6}$$

In the equations above, the superscript *el* corresponds to the quantities at the elastic limit. Since the state ahead of the elastic shock wave is at rest, the Eulerian elastic shock velocity is the same as the Lagrangian velocity.

For the shock jump conditions across the plastic shock wave, Eqs. 2.1 and 2.2 are rearranged taking into account that the state ahead of a shock is the elastic limit. The rearranged equations are shown below.

$$\rho^{pl}(U^{pl}_{Eu} - u^{pl}) = \rho^{el}(U^{pl}_{Eu} - u^{el}) \tag{5.7}$$

$$\sigma^{pl}_x - \sigma^{el}_x = \rho^{el}(U^{pl}_{Eu} - u^{el})(u^{pl} - u^{el}). \tag{5.8}$$

In this case, the Eulerian plastic shock velocity is given by:

$$U^{pl}_{Eu} = \frac{\rho_0}{\rho^{el}} U^{pl} + u^{el} \tag{5.9}$$

where U^{pl} is the Lagrangian (measured) plastic shock velocity. Using Eq. 5.9 in Eq. 5.6, the expression for the peak stress is simplified as follows.

$$\begin{aligned} \sigma^{pl}_x &= \sigma^{el}_x + \rho^{el}(u^{pl} - u^{el})U^{pl}_{Eu} - \rho^{el}(u^{pl} - u^{el})u^{el} \\ &= \sigma^{el}_x + \rho^{el}(u^{pl} - u^{el})\left(\frac{\rho_0}{\rho^{el}} U^{pl} + u^{el}\right) - \rho^{el}(u^{pl} - u^{el})u^{el} \\ &= \sigma^{el}_x + \rho_0 U^{pl}(u^{pl} - u^{el}). \end{aligned} \tag{5.10}$$

Figure 5.3 shows the P - u diagram for an experiment in which the two-wave structure is observed. Longitudinal stress at the elastic limit σ^{el}_x is referred to as the elastic wave amplitude.

After Mo reached the elastic limit, the forward propagating elastic wave interacted with the Mo sample - LiF window interface, and the Mo released to State 3. In a similar manner, after Mo reached the peak state, Mo released to State 4. In the calculation here, the following assumptions were made.

- Release in Mo from the elastic limit follows the reflected elastic Hugoniot (the amplitudes of the tangent are the same).

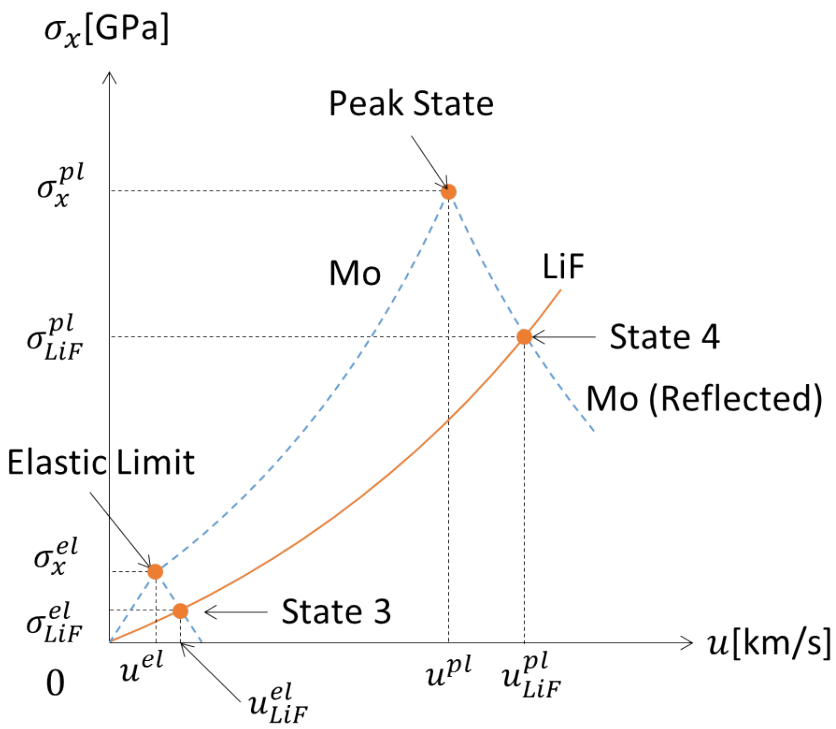

Figure 5.3: P - u diagram in a plate impact experiment with a two-wave structure. Orange solid line represents known Hugoniot relation, and blue dashed line represents unknown Hugoniot relation. Even though Table 4.1 lists constructed elastic Hugoniot relations for Mo, they are treated as unknowns because those relations were not used in the calculation here.

- Release in Mo occurs along a reflected Hugoniot whose tangent is between ρU^{el} and ρU^{pl}.
- Reshock in LiF occurs along the principal Hugoniot.

The peak stress was calculated based on both elastic and plastic shock velocities, and those two values were treated as upper and lower bound for the peak stress. For the experiments with a two-wave structure, this method gives a reasonable estimate for the experimental uncertainties, rather than calculating based on the assumption on the reshock of buffer as in the case of an overdriven wave.

Based on the known Hugoniot relation for LiF shown in Table 4.1, the longitudinal stress at state 3, σ_{LiF}^{el} can be written as

$$\sigma_{LiF}^{el} = \rho_{LiF}(5.15 + 1.35u_{LiF}^{el})u_{LiF}^{el} \tag{5.11}$$

where ρ_{LiF} is the ambient density of LiF.

Also, based on the first assumption above, the longitudinal stress at state 3 is given by,

$$\sigma_{LiF}^{el} = \rho_0 U^{el}(2u^{el} - u_{LiF}^{el}). \tag{5.12}$$

In Eqs. 5.11 and 5.12, there are two unknowns: σ_{LiF}^{el} and u^{el}. By numerically solving these two equations simultaneously, the in-material particle velocity at the elastic limit was determined. The elastic wave amplitude and the density at the elastic limit were calculated using Eqs. 5.5 and 5.6.

For the peak state, the peak stress can be calculated based on Eq. 5.10,

$$\sigma_x^{pl} = \sigma_x^{el} + \rho_0 U^{pl}(u^{pl} - u^{el}). \tag{5.13}$$

Also, based on the second assumption above, the peak stress can be written as either of the following equations:

$$\sigma_x^{pl} = \sigma_{LiF}^{pl} + \rho_0 U^{el}(u_{LiF}^{pl} - u^{pl}), \tag{5.14}$$

$$\sigma_x^{pl} = \sigma_{LiF}^{pl} + \rho_0 U^{pl}(u_{LiF}^{pl} - u^{pl}), \tag{5.15}$$

where

$$\sigma_{LiF}^{pl} = \rho_{LiF}(5.15 + 1.35u_{LiF}^{pl})u_{LiF}^{pl}. \tag{5.16}$$

Since the in-material quantities at the elastic limit are already calculated, the unknown variables in Eqs. 5.13 - 5.15. are σ_x^{pl} and u^{pl}. By numerically solving Eqs. 5.13 and 5.14 or Eqs. 5.13 and 5.15, the in-material particle velocity at the peak state was calculated. Then, the average of the calculated particle velocities was used in further analysis. Based on the calculated in-material particle velocity, the density and the peak stress were calculated at the peak state.

5.2 In-Material Quantities at the Elastic Limit

In-material quantities at the elastic limit calculated by the method described above are summarized in Table 5.1 along with the elastic shock velocity and the measured particle velocity (Mo sample - LiF interface) at the elastic limit.

Table 5.1: Calculated in-material quantities at the elastic limit

Exp. Number	Loading Direction	Sample Thickness [mm]	Elastic Impact Stress [GPa]	Elastic Shock Velocity [km/s]	Measured Particle Velocity [km/s]	In-material Quantities		
						Particle Velocity [km/s]	Longitudinal Stress [GPa]	Density [g/cc]
A1	[100]	2.019	23.2	6.79±0.17	0.0954±0.001	0.057±0.001	3.98±0.11	10.307±0.003
A2[1]		2.010	65.7	6.76±0.14[2]	0.0877±0.001	0.053±0.001	3.64±0.09	10.300±0.002
A3		2.011	66.2	6.82±0.14[2]	0.0975±0.001	0.059±0.001	4.08±0.10	10.308±0.003
A4		2.030	89.1	6.87±0.07	0.103±0.002	0.061±0.001	4.31±0.07	10.312±0.002
A5[1]		2.027	108.6	6.99±0.13[3]	0.119±0.002	0.071±0.001	5.08±0.11	10.325±0.003
A6		2.030	116.1	7.01±0.13[3]	0.0963±0.001	0.058±0.001	4.12±0.09	10.305±0.002
A7		2.022	183.9	(Overdriven)				
B1	[111]	2.027	23.9	6.52±0.15	0.172±0.002	0.105±0.002	6.96±0.19	10.387±0.005
B2		2.029	24.0	6.58±0.15	0.167±0.002	0.101±0.002	6.78±0.19	10.379±0.005
B3		2.009	67.4	6.59±0.13[2]	0.187±0.002	0.113±0.002	7.60±0.19	10.398±0.005
B4		2.043	93.7	6.73±0.07	0.198±0.002	0.120±0.002	8.23±0.13	10.405±0.003
B5		2.027	114.6	6.96±0.12[3]	0.214±0.003	0.128±0.002	9.13±0.20	10.412±0.005
B6		2.034	197.5	(Overdriven)				
B7		3.499	98.1	6.79±0.04	0.199±0.002	0.120±0.002	8.31±0.11	10.404±0.003
B8		3.497	113.3	6.98±0.07[3]	0.200±0.002	0.120±0.002	8.54±0.14	10.399±0.003
C1	[110]	2.021	23.5	6.48±0.15	0.0999±0.001	0.060±0.001	4.00±0.11	10.316±0.003
C2		2.018	67.0	6.42±0.13[2]	0.104±0.002	0.063±0.001	4.15±0.10	10.322±0.003
C3		2.032	90.9	6.63±0.07	0.106±0.002	0.064±0.001	4.32±0.07	10.319±0.002
C4		2.029	112.9	(Overdriven)				
C5		2.040	193.1	(Overdriven)				

By comparing the results from 2 mm thick sample experiments in Table 5.1, a positive correlation between the elastic wave amplitude and the impact stress is observed, except for experiment A2. The inconsistency in experiment A2 was discussed in Section 4.2.

Figure 5.4 shows the plot of the elastic wave amplitude against the impact stress along each orientation for 2 mm thick sample experiments. The data from lower stress impact experiments with comparable thickness (2.3 mm) samples [1–3] are also shown for comparison. A linear fit - only for the present work - is superposed onto the results along each orientation.

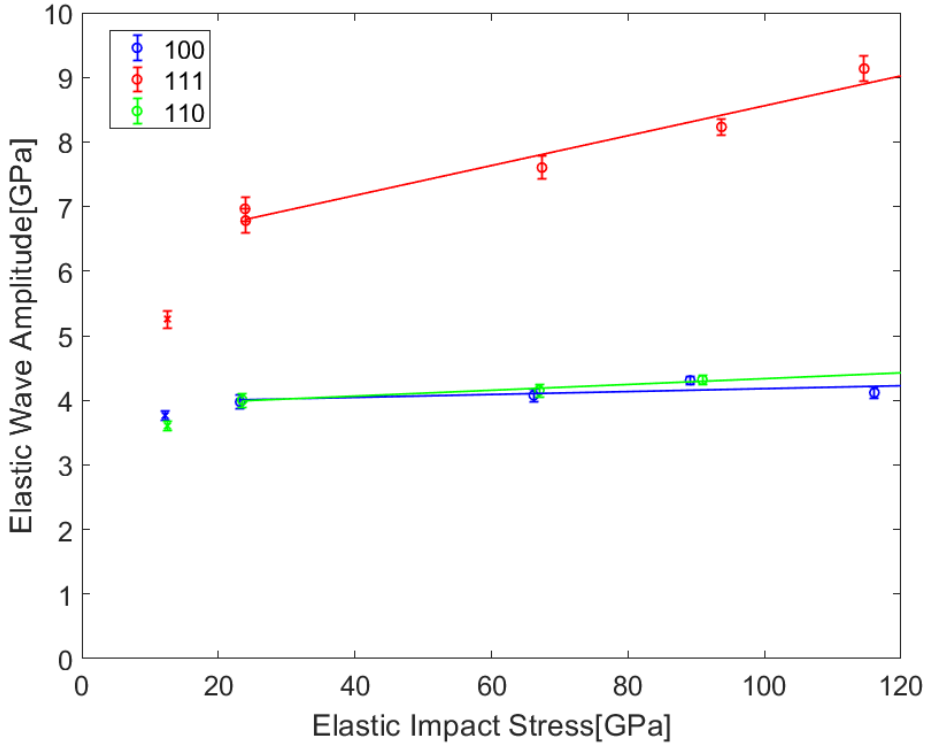

Figure 5.4: Elastic wave amplitude vs. impact stress for the three different orientations. The data from lower stress impact experiments [1–3] at a comparable sample thickness of 2.3 mm are shown with markers "x".

Figure 5.4 shows that the elastic wave amplitude increases linearly with the elastic impact stress. The elastic wave amplitude is significantly larger along the [111]

[1]These experiments are excluded from further discussions due to the inconsistencies mentioned in Section 4.2.

[2]Impactor bowing correction of 4.1± 2 ns is applied.

[3]Impactor bowing correction of 2.0± 2 ns is applied.

orientation compared to the other orientations, and the dependence on the elastic impact stress is also larger along the [111] orientation. Along the [100] and [110] orientations, the elastic wave amplitude shows a slight increase, but the dependence on the elastic impact stress is minimal. The equation for the linear fit along [111] orientation is:

$$\text{Above 23 GPa: } \sigma_x^{el} = 0.023\sigma^{imp} + 6.25 \text{ [GPa]}. \tag{5.17}$$

The elastic wave amplitudes at the lowest impact stress [1–3] do not match well with the extrapolations from the present results. This difference is most pronounced for the [111] orientation and is well beyond the combined experimental scatter from the previous work and the present work. At present, it is not possible to explain the rapid increase in the elastic wave amplitude - between the two lowest impact stresses - in Fig. 5.4.

Since all of the experiments in Fig. 5.4 form the present work were conducted with a constant sample thickness, the differences in the elastic wave amplitudes imply that the decay of the elastic wave amplitude with the propagation distance depends on the crystal orientation. Also, the larger elastic wave amplitude along the [111] orientation means that the decay rate is smaller along the [111] orientation. These observations are consistent with the observation at the lower impact stress [1–3].

The anisotropic response is manifested in terms of the elastic shock velocity as well. In Table 5.1, for 23, 66, and 90 GPa impact experiments, one can observe that the elastic shock velocity was higher along the [100] orientation compared to the [111] and [110] orientations, which were comparable.

5.3 Resolved Shear Stresses at the Elastic Limit

To better understand the anisotropy effects seen in Fig. 5.4 and to gain insight into the slip systems governing elastic-plastic deformation in Mo single crystals, the maximum resolved shear stresses (RSS) on {110}<111> and {112}<111> slip systems - at the elastic limit - were calculated following the approach by Johnson *et al.* [6]. The results are shown in Figs. 5.5 and 5.6. As in Fig. 5.4, the data from the lower impact stress experiments [1–3] (for comparable thickness samples) are shown for comparison. A linear fit to the present data is shown for each orientation. The black horizontal line in both figures represents the corresponding Peierls stress of screw dislocations on each family of planes [7].

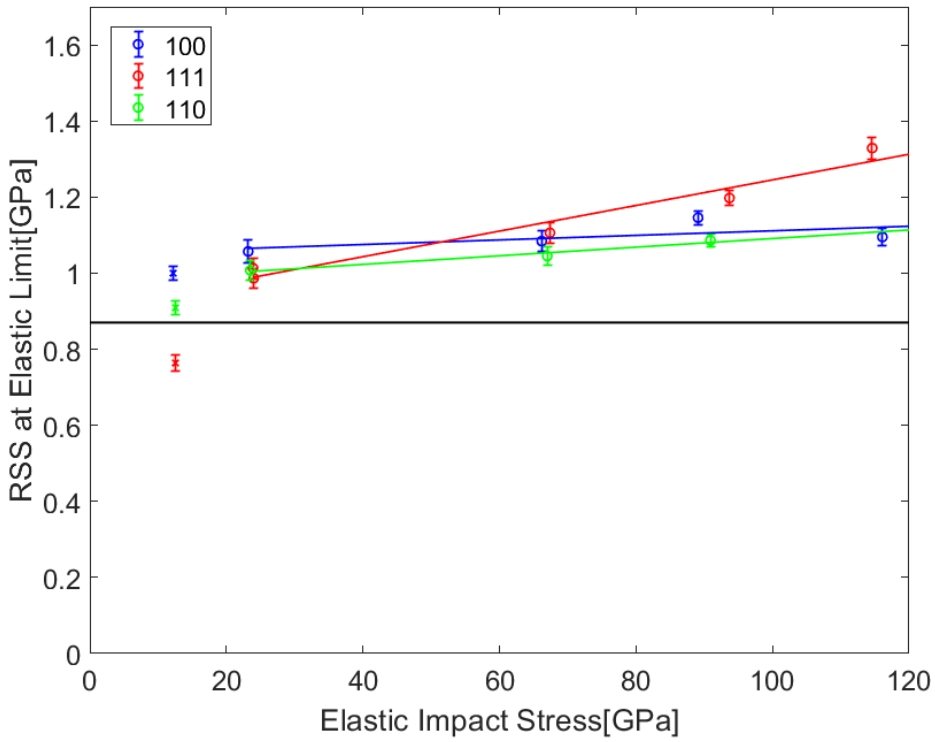

Figure 5.5: Resolved shear stress (RSS) at the elastic limit on {110}<111> slip system (data from 2 mm thick sample experiments). The data from lower stress impact experiments [1–3] at a comparable sample thickness of 2.3 mm are shown with markers "x".

In Figs. 5.5 and 5.6, one can observe the same trend as in Fig. 5.4: RSS at the elastic limit increases linearly with increasing elastic impact stress. Along the [111] orientation, RSS showed a strong increase, while only a slight increase was observed along the [100] and [110] orientations. This is expected because the RSS is proportional to the longitudinal stress. However, the differences in the RSS at the elastic limit among different orientations are smaller compared to the differences in the corresponding longitudinal stress (elastic wave amplitude) in Fig. 5.4. The difference between the RSS and the corresponding Peierls stress reported in earlier work [7] is smaller for the {110}<111> slip system than for the {112}<111> slip system.

When the RSS is greater than the Peierls stress, phonon-drag controls the plastic deformation [8]. Figs. 5.5 and 5.6 shows that the RSS was larger than the Peierls stress. Thus, the temperature dependence that arises in the thermally activated pair-kink formation will not be considered. Yang *et al.* [8] also reported on the pressure

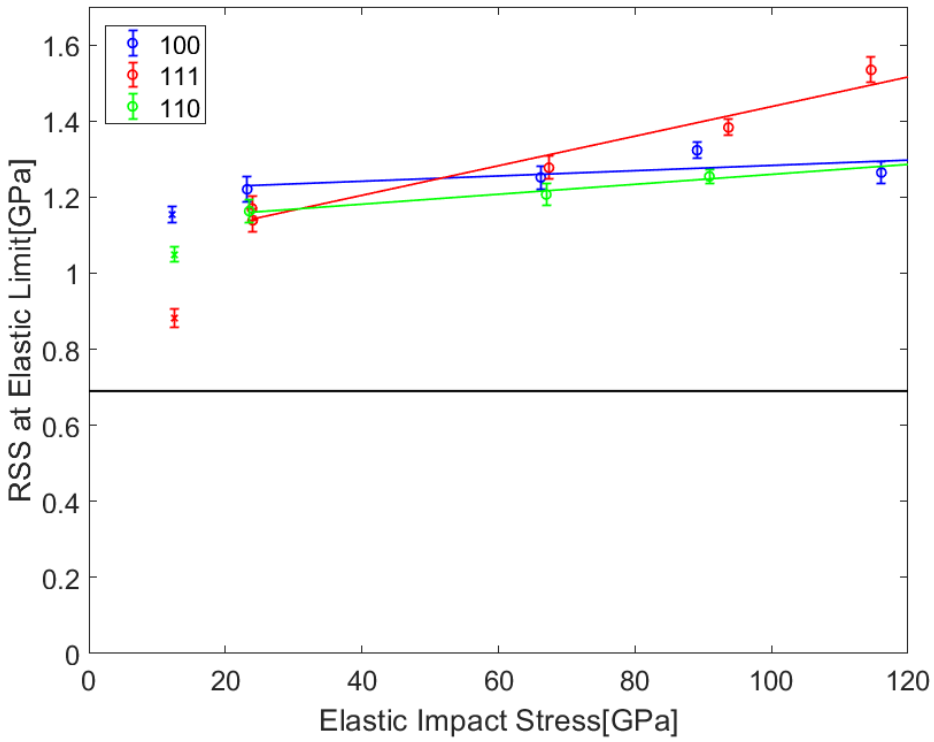

Figure 5.6: Resolved shear stress (RSS) at the elastic limit on {112}<111> slip system (data from 2mm thick sample experiments). The data from lower stress impact experiments [1–3] at a comparable sample thickness of 2.3mm are shown with markers "x".

dependence of the Peierls stress. The pressure (or mean stress) at the elastic limit can be calculated from the elastic constants [9] and the elastic wave amplitude by considering the uniaxial strain loading condition. The pressure is given by:

$$\begin{aligned} P &= \frac{1}{3}(\widetilde{C}_{1111}\epsilon_{11} + \widetilde{C}_{2211}\epsilon_{11} + \widetilde{C}_{3311}\epsilon_{11}) \\ &= \frac{\widetilde{C}_{1111} + \widetilde{C}_{2211} + \widetilde{C}_{3311}}{3\widetilde{C}_{1111}}\sigma^{el} \end{aligned} \tag{5.18}$$

where

$$\widetilde{C}_{ijkl} = R_{im}R_{jn}R_{ko}R_{lp}C_{mnop}. \tag{5.19}$$

In Eq. 5.19, R_{ij} is a rotation tensor corresponding to each loading orientation.

The maximum pressure at the elastic limit, achieved in experiment B5, was 5.9 GPa. Based on the second order polynomial fit to the pressure dependence reported in Yang *et al.* [8], the Peierls stress at a pressure of 5.9 GPa is only 5% larger than

that at ambient pressure. Thus, for the discussion regarding the elastic limit, the pressure dependence of Peierls stress is not a significant factor.

The RSS plots in Figs. 5.5 and 5.6 suggest the activation of the {110}<111> slip system at the elastic limit. This inference assumes that the RSS value falls in the vicinity of the threshold for activating deformation mechanism. In the lower stress study [1–3], it was not possible to distinguish between the two possible slip systems. However in the present work, the considerable difference between the RSS and the Peierls stress on the {112}<111> slip system points to the activation of the {110}<111> slip system.

The Peierls stress for edge dislocations in Mo obtained using Finnis-Sinclair potential is 25 MPa [10], which is significantly smaller than the RSS shown in Figs. 5.5 and 5.6. This supports the view that the plasticity in BCC crystals at high impact stresses are governed by the motion of screw dislocations. This inference is consistent with the past studies under quasi static loading [7, 8, 11–15].

5.4 Comparison with 3.5 mm Thick Sample Experiments

As discussed in Section 5.2, the elastic wave amplitude along the [111] orientation showed significant dependence on the impact stress. Since time-dependent behavior was observed in the velocity profiles (Figs. 4.3 - 4.10), this dependence cannot be attributed entirely to the impact stress; the effect of propagation distance on the elastic wave amplitude needs to be considered. Toward this end, the results for the 3.5 mm thick samples (experiments B7 and B8) are compared with the corresponding 2 mm thick samples (experiments B4 and B5).

As shown in Table 5.1, for ~90 GPa impact stress experiments (B4 and B7), measurable decay was not observed in the elastic wave amplitude with propagation distance. For ~110 GPa impact stress experiments (B5 and B8), the elastic wave amplitude at a propagation distance of 3.5 mm was 7% lower than at 2 mm. This difference indicated that the elastic wave amplitude at ~110 GPa impact stress had not fully decayed at a propagation distance of 2 mm.

5.5 Comparison with Elastic Hugoniot Relations

The elastic wave amplitude calculated using elastic Hugoniot relations [1, 2] shown in Table 4.1 is compared with the value based on the experiments and analysis. In the calculation using elastic Hugoniot relations, the in-material particle velocity at the elastic limit in Table 5.1 is used. The results are compared in Table 5.2.

Table 5.2: Comparison with elastic Hugoniot relations

Exp. Number		Elastic Impact Stress [GPa]	In-material Particle Velocity [km/s]	Elastic Wave Amplitude: From Analysis [GPa]	Elastic Wave Amplitude: Elastic Hugoniot Relations [GPa]
A1	[100]	23.2	0.057±0.001	3.98±0.11	3.99±0.06
A3		66.2	0.059±0.001	4.08±0.10	4.08±0.06
A4		89.1	0.061±0.001	4.31±0.07	4.28±0.06
A6		116.1	0.058±0.001	4.12±0.09	4.01±0.06
B1	[111]	23.9	0.105±0.002	6.96±0.19	7.00±0.11
B2		24.0	0.101±0.002	6.78±0.19	6.74±0.10
B3		67.4	0.113±0.002	7.60±0.19	7.58±0.11
B4		93.7	0.120±0.002	8.23±0.13	8.05±0.10
B5		114.6	0.128±0.002	9.13±0.20	8.66±0.12
B7		98.1	0.120±0.002	8.31±0.11	8.06±0.10
B8		113.3	0.120±0.002	8.54±0.14	8.05±0.11
C1	[110]	23.5	0.060±0.001	4.00±0.11	4.04±0.06
C2		67.0	0.063±0.001	4.15±0.10	4.24±0.06
C3		90.9	0.064±0.001	4.32±0.07	4.26±0.06

Table 5.2 shows that the elastic wave amplitude based on the elastic Hugoniot relations [1, 2] agrees with our analysis within the experimental uncertainties except for experiments B5, B6, and B8 along the [111] orientation. For these experiments, the elastic Hugoniot relations underestimate the elastic wave amplitude by 5.4%, 3.1%, and 6.1%, respectively.

In the present work, the elastic Hugoniot relations were only used to calculate the elastic impact stress, but one can see that, overall, they agree reasonably well with the experimentally obtained elastic wave amplitude.

5.6 In-Material Quantities at the Peak State

Table 5.3 summarizes the calculated in-material quantities at the peak state along with the plastic shock velocity and the measured particle velocity at the Mo sample - LiF window interface behind the plastic shock wave. The plastic shock velocity shown in the table is the Eulerian (spatial) velocity U_{Eu}^{pl} which is given by Eq. 5.9.

Table 5.3 shows that the difference at the peak state between orientations in terms of the calculated in-material quantities were within experimental uncertainties. This is consistent with the observation for the measured quantities in Section 4.4.

Table 5.3: Calculated in-material quantities at the peak state

Exp. Number	Loading Direction	Sample Thickness [mm]	Elastic Impact Stress [GPa]	Plastic[1] Shock Velocity [km/s]	Measured Particle Velocity [km/s]	In-material Quantities		
						Particle Velocity [km/s]	Peak Stress [GPa]	Density [g/cc]
A1	[100]	2.019	23.2	5.39±0.10	0.588±0.006	0.383±0.024	21.9±1.4	10.977±0.053
A2[2]		2.010	65.7	6.16±0.12[3]	1.40±0.02	0.916±0.036	57.9±2.5	11.996±0.089
A3		2.011	66.2	6.21±0.12[3]	1.41±0.02	0.921±0.036	58.8±2.5	11.991±0.089
A4		2.030	89.1	6.57±0.07	1.80±0.02	1.18±0.03	79.1±2.1	12.442±0.072
A5[2]		2.027	108.6	6.85±0.12[4]	2.10±0.03	1.37±0.04	96.0±3.1	12.775±0.101
A6		2.030	116.1	6.96±0.12[4]	2.22±0.03	1.44±0.04	102.7±3.2	12.889±0.103
A7		2.022	183.9	7.75±0.15[5]	3.16±0.04	2.15±0.02	170.1±3.6	14.139±0.114
B1	[111]	2.027	23.9	5.41±0.10	0.602±0.007	0.387±0.023	22.5±1.3	10.971±0.051
B2		2.029	24.0	5.44±0.11	0.605±0.007	0.388±0.023	22.7±1.3	10.969±0.051
B3		2.009	67.4	6.18±0.12[3]	1.40±0.02	0.913±0.033	58.1±2.3	11.978±0.081
B4		2.043	93.7	6.63±0.07	1.81±0.02	1.17±0.03	79.7±1.9	12.418±0.063
B5		2.027	114.6	6.89±0.12[4]	2.12±0.03	1.38±0.04	97.0±3.0	12.765±0.097
B6		2.034	197.5	7.84±0.16[5]	3.16±0.04	2.13±0.02	171.1±3.7	14.043±0.111
C1	[110]	2.021	23.5	5.51±0.11	0.592±0.006	0.382±0.020	22.1±1.2	10.963±0.045
C2		2.018	67.0	6.17±0.12[3]	1.41±0.02	0.913±0.029	57.7±2.1	11.990±0.074
C3		2.032	90.9	6.59±0.07	1.78±0.02	1.16±0.03	77.9±1.7	12.394±0.058
C4		2.029	112.9	6.91±0.12[4]	2.12±0.03	1.42±0.02	100.6±1.9	12.871±0.063
C5		2.040	193.1	7.88±0.16[5]	3.16±0.04	2.13±0.02	171.8±3.7	14.014±0.111

5.7 Hugoniot Relations at the Peak State

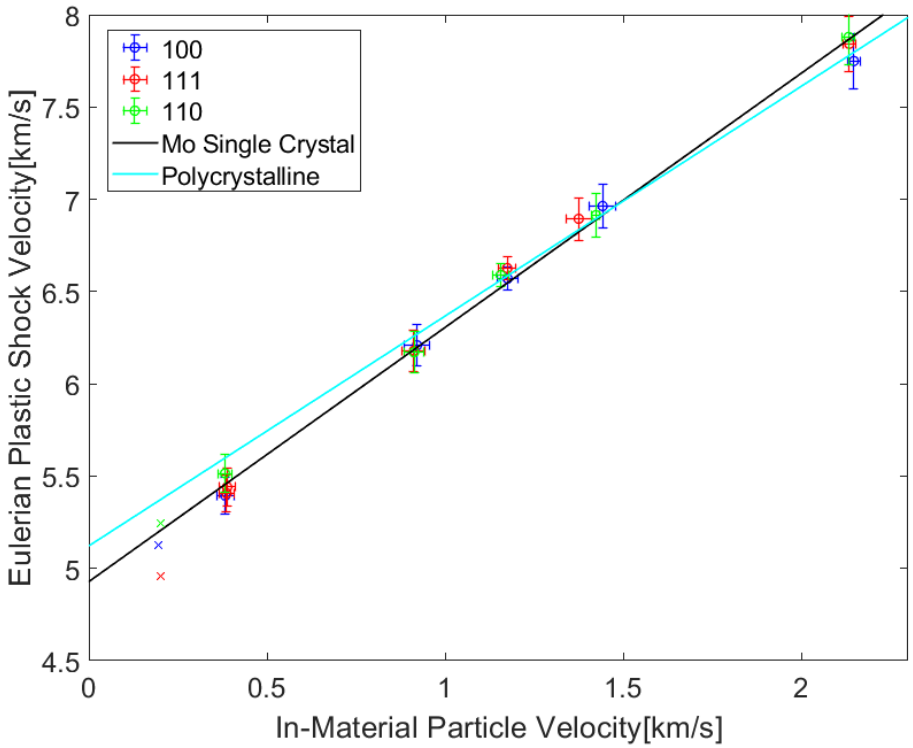

Figure 5.7: Eulerian shock velocity vs. in-material particle velocity ($U_s - u_p$) plot at the peak state.

In this section, Hugoniot relations for Mo single crystals are calculated based on Table 5.3, and compared with the Hugoniot relation for polycrystalline Mo [4]. Figure 5.7 shows the plot of Eulerian plastic shock velocity against the in-material particle velocity at the peak state ($U_s - u_p$ plot). Figure 5.8 is the plot of peak stress against the specific volume at the peak state ($P - v$ plot). Each point in those figures corresponds to one of the experiments. In these figures, the data from lower stress impact experiments with comparable thickness (2.3 mm) sample [3] are shown with markers "x".

In Figs. 5.7 and 5.8, one can see that the difference between the three orientations is within the experimental uncertainties. Therefore, we applied single fit for all of

[1]Eulerian velocity.

[2]These experiments are excluded from further discussions due to the inconsistencies mentioned in Section 4.2.

[3]Impactor bowing correction of 4.1± 2 ns is applied.

[4]Impactor bowing correction of 2.0± 2 ns is applied.

[5]Impactor bowing correction of 29± 2 ns is applied.

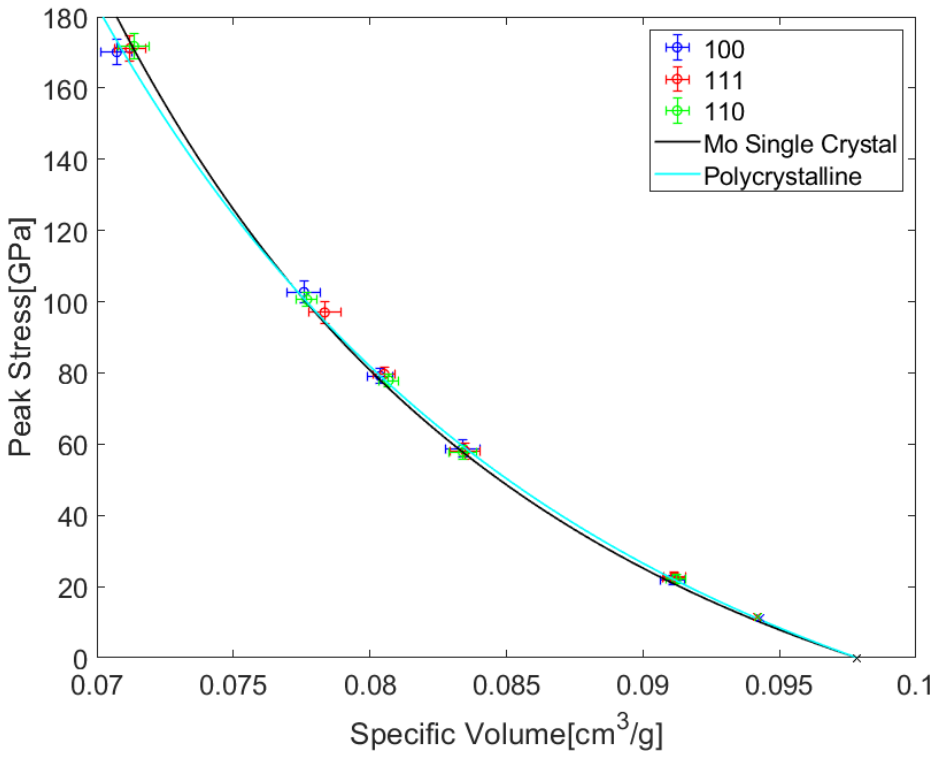

Figure 5.8: Peak stress vs. specific volume ($P - v$) plot at the peak state.

the experimental data. In the $U_s - u_p$ plot, the points can be fitted reasonably with a straight line, which is shown as a black line. The equation for the linear fit for Mo single crystals is

$$U_s = 4.928 + 1.377u_p. \tag{5.20}$$

The unit in the equation above is km/s. In Figs. 5.7 and 5.8, the Hugoniot relation for polycrystalline Mo [4] is shown as the light blue line. Figure 5.7 shows that those two lines agree reasonably well. The straight lines in $U_s - u_p$ plot correspond to the convex curves in the $P - v$ plot. In Fig. 5.8, one can see that those two lines agree reasonably well also in the $P - v$ plane.

As mentioned above, the empirical linear $U_s - u_p$ relation applies to Mo single crystals, and the difference between three crystal orientations was not significant. This means that, in terms of macroscopic behavior, the peak state is independent of loading orientation for the stress range examined in this study. It is noted that the tangent of the $U_s - u_p$ relation for Mo single crystals falls within the empirical range of 1.1-1.5 [16, 17]. Also, the Hugoniot relation for Mo single crystals obtained in this study agrees well with polycrystalline Mo. This implies that the peak state is

not affected by the presence of grain boundaries.

5.8 Orientation-Independence at the Peak State

In Sections 5.6 and 5.7, it was noted that the macroscopic behavior at the peak state is independent of crystal orientation. This is consistent with the experimental observation in Section 4.4 that the plastic shock velocity and the particle velocity behind the plastic shock wave were independent of orientation within experimental uncertainties. However, as seen in Section 4.2, the anisotropy was observed at the elastic limit.

In this section, the following question is addressed: in the stress range that the two-wave structure was observed in the present study, why are the in-material quantities at the peak state independent of crystal orientation while the elastic limit exhibits anisotropic behavior?

As described in Section 5.1, when the shock wave is overdriven, the peak stress is calculated using Eq. 5.2.

$$\sigma_x^{pl} = \rho_0 U^{pl} u^{pl}. \tag{5.21}$$

The subscript "Eu" is omitted here since the Lagrangian and Eulerian shock velocities are the same in the case of overdriven shock wave.

When the two-wave structure is observed, the peak stress is calculated by Eq. 5.10,

$$\sigma_x^{pl} = \sigma_x^{el} + \rho_0 U^{pl}(u^{pl} - u^{el}).$$

This can be rearranged as:

$$\sigma_x^{pl} = (\rho_0 U^{pl} u^{pl}) + (\sigma_x^{el} - \rho_0 U^{pl} u^{el}). \tag{5.22}$$

In Eq. 5.22, the first part ($\rho_0 U^{pl} u^{pl}$) can be thought as the contribution to the peak stress from the peak state, and the second part ($\sigma_x^{el} - \rho_0 U^{pl} u^{el}$) can be thought as the contribution from the elastic limit. In order to compare the contributions from those two terms, the values for the two terms are calculated for each experiment. The results are shown in Table 5.4.

In Table 5.4, one can see that the contribution from the elastic limit is smaller than the uncertainties in the peak stress. Also, the difference in the contribution from the peak state among three orientations agree within the experimental uncertainties. This means that, even if the peak stress was calculated ignoring the elastic state, the value would have been still within the experimental uncertainties.

Table 5.4: Contribution from each state to the peak stress

Exp. Number	Peak Stress [GPa]	Contribution from Peak State $\rho_0 U^{pl} u^{pl}$ [GPa]	Elastic Limit $\sigma_x^{el} - \rho_0 U^{pl} u^{el}$ [GPa]
A1	21.9±1.4	21.1±1.4	0.83±0.14
A3	58.8±2.5	58.4±2.6	0.37±0.14
A4	79.1±2.1	78.9±2.2	0.19±0.10
A6	102.7±3.2	102.6±3.2	0.03±0.13
A7	170.1±3.6	170.1±3.6	—
B1	22.5±1.3	21.3±1.3	1.21±0.23
B2	22.7±1.3	21.5±1.4	1.19±0.23
B3	58.1±2.3	57.6±2.3	0.48±0.25
B4	79.7±1.9	79.5±1.9	0.13±0.18
B5	97.0±3.0	96.9±3.1	0.09±0.28
B6	171.1±3.7	171.1±3.7	—
C1	22.1±1.2	21.5±1.2	0.60±0.14
C2	57.7±2.1	57.6±2.1	0.16±0.14
C3	77.9±1.7	77.8±1.8	0.03±0.10
C4	100.6±1.9	100.6±1.9	—
C5	171.8±3.7	171.8±3.7	—

For the range of stress examined in the present study, the effect from the elastic limit is considerably small. Also, as discussed in Section 4.4, the plastic shock velocity and the particle velocity behind the plastic shock wave are independent of the crystal orientation. Therefore, the anisotropic behavior at the elastic limit does not manifest at the peak state.

The observation that macroscopic behavior at the peak state does not depend on the crystal orientation at high impact stresses is consistent with what have been observed in the cases of Al [18] and Cu [19]. This implies that the deformation at the peak state in a macroscopic sense is dominated by the amplitude of the loading. However, we also have to note that this does not necessarily mean that the peak state is isotropic. Crystals under extreme compression might still maintain some structure that gives rise to an anisotropic behavior in a microscopic sense. This aspect of shock-induced deformation in Mo single crystals needs further investigation.

5.9 Summary

The significant findings from the analysis are summarized below.

At the elastic limit:

- The elastic wave amplitude increases with the elastic impact stress. The elastic wave amplitude is significantly larger along the [111] orientation compared to the other orientations, and the dependence on the impact stress is most pronounced along the [111] orientation.

- In the high stress range, the decay rate of the elastic wave amplitude depends on the crystal orientation and is smaller along [111] orientation. This is consistent with the observations at lower stress [1–3].

- Compared to the lower stress data [1–3], the elastic wave amplitudes in the present work are higher. The increase from the lower stress data is maximum for the [111] orientation. However, there is no adequate explanation for this large increase.

- At the elastic limit, the difference between RSS and the corresponding Peierls stress is smaller on the {110}<111> slip system than on the {112}<111> slip system. This suggests the activation of the {110}<111> slip system at the elastic limit.

At the peak state:

- In terms of the $U_s - u_p$ and the $P - v$ plots, the difference between [100], [111], and [110] orientations is within the experimental uncertainties.

- The Hugoniot relations obtained for Mo single crystals in the present work agree reasonably well with the Hugoniot relation for polycrystalline Mo [4]. This implies that the in-material quantities at the peak state does not depend on the presence of grain boundaries.

- The anisotropic behavior at the elastic limit does not manifest at the peak state. This is because the contribution to the peak stress from the elastic state is considerably small and the plastic shock velocity and the particle velocity at the peak state are independent of the crystal orientation.

- The observation, that the in-material quantities at the peak state is independent of the crystal orientation, implies that the deformation at the peak state in a macroscopic sense is dominated by the amplitude of the loading.

References

[1] A. Mandal and Y. M. Gupta. “Elastic-plastic deformation of molybdenum single crystals shocked along [100].” In: *Journal of Applied Physics* 121.4 (2017), p. 045903.

[2] A. Mandal and Y. M. Gupta. “Elastic-plastic deformation of molybdenum single crystals shocked to 12.5 GPa: Crystal anisotropy effects.” In: *Journal of Applied Physics* 125.5 (2019), p. 055903.

[3] A. Mandal. “Elastic-Plastic Deformation of Molybdenum Single Crystals Shocked to 12.5 GPa.” PhD thesis. Washington State University, School of Mechanical and Materials Engineering, 2016.

[4] R. S. Hixson and J. N. Fritz. “Shock compression of tungsten and molybdenum.” In: *Journal of Applied Physics* 71.4 (1992), p. 1721.

[5] W. J. Nellis, A. C. Mitchell, and D. A. Young. “Equation-of-state measurements for aluminum, copper, and tantalum in the pressure range 80–440 GPa (0.8–4.4 Mbar).” In: *Journal of Applied Physics* 93.1 (2003), p. 304.

[6] J. N. Johnson, O. E. Jones, and T. E. Michaels. “Dislocation Dynamics and Single-Crystal Constitutive Relations: Shock-Wave Propagation and Precursor Decay.” In: *Journal of Applied Physics* 41.6 (1970), p. 2330.

[7] L. Hollang, D. Brunner, and A. Seeger. “Work hardening and flow stress of ultrapure molybdenum single crystals.” In: *Materials Science and Engineering: A* 319 (2001), p. 233.

[8] L. H. Yang, M. Tang, and J. A. Moriarty. “Dislocations and plasticity in bcc transition metals at high pressure.” In: *Dislocations in Solids* 16 (2010), p. 1.

[9] D. L. Davidson and F. R. Brotzen. “Elastic Constants of Molybdenum-Rich Rhenium Alloys in the Temperature Range -190 °C to +100 °C.” In: *Journal of Applied Physics* 39.12 (1968), p. 5768.

[10] W. Cai, V. V. Bulatov, J. Chang, J. Li, and S. Yip. “Dislocation core effects on mobility.” In: *Dislocations in Solids* 12 (2004), p. 1.

[11] D. Veselý. “The Study of Deformation of Thin Foils of Mo under the Electron Microscope.” In: *Physica Status Solidi* 29 (1968), p. 675.

[12] D. Veselý. “The Study of Slip Bands on the Surface of Mo Single Crystals.” In: *Physica Status Solidi* 29 (1968), p. 685.

[13] C. R. Weinberger, B. L. Boyce, and C. C. Battaile. “Slip planes in bcc transition metals.” In: *International Materials Reviews* 58.5 (2013), p. 296.

[14] A. Seeger. “The flow stress of high-purity refractory body-centred cubic metals and its modification by atomic defects.” In: *Le Journal de Physique IV* 5.C7 (1995), pp. C7–45.

[15] A. Seeger and L. Hollang. “The flow-stress asymmetry of ultra-pure molybdenum single crystals.” In: *Materials Transactions, JIM* 41.1 (2000), p. 141.

[16] J. W. Swegle and D. E. Grady. “Shock viscosity and the prediction of shock wave rise times.” In: *Journal of Applied Physics* 58.2 (1985), p. 692.

[17] A. Molinari and G. Ravichandran. “Fundamental structure of steady plastic shock waves in metals.” In: *Journal of Applied Physics* 95.4 (2004), p. 1718.

[18] D. Choudhuri and Y. M. Gupta. “Shock compression of aluminum single crystals to 70 GPa: Role of crystalline anisotropy.” In: *Journal of Applied Physics* 114.15 (2013), p. 153504.

[19] R. Chau, J. Stölken, P. Asoka-Kumar, M. Kumar, and N. C. Holmes. “Shock Hugoniot of single crystal copper.” In: *Journal of Applied Physics* 107.2 (2010), p. 023506.

Chapter 6

NUMERICAL MODELING OF SHOCK COMPRESSED MOLYBDENUM SINGLE CRYSTALS

To gain insight into deformation mechanisms activated during the shock-induced elastic-plastic deformation, finite element method (FEM) simulations using Abaqus Explicit [1] were carried out for shock compression of Mo single crystals along [100], [111], and [110] orientations. For the material model, a crystal plasticity model was implemented using VUMAT subroutine [2] as a FORTRAN code.

6.1 Motivation

The plate impact experiments with continuum measurements provide shock velocities and particle velocity profiles. However, these experiments do not provide direct information about the evolution of the micro structure such as activated deformation mechanisms and the amount of plastic deformation. In this regard, numerical simulations shed light on deformation mechanisms, since the amount of plastic deformation can be computed in the form of internal variables. The results from the experiments can be compared with predictions from the numerical simulations to help validate the crystal plasticity models. Also, in terms of engineering applications, accurate numerical simulations of shock induced phenomena can significantly reduce the need for experimental testing of materials and products.

FEM simulations were conducted using Abaqus Explicit incorporating a crystal plasticity model. Quantitative description of the plastic deformation of single crystals by slip was first considered in the experimental work by Taylor *et al.* [3] and Taylor [4]. The framework for the elastic-plastic deformation of single crystals due to slip was later developed by Hill [5]. FEM simulations of elastic-plastic deformation of single crystals was first carried out by Peirce *et al.* [6]. The constitutive description employed in their work was based on the model by Asaro *et al.* [7]. Since the model explicitly accounts for crystallographic slip process, it is also referred to as the physical theory of plasticity [8]. In our simulation, the crystal plasticity model described in Lee *et al.* [9] was modified and implemented in Abaqus using VUMAT subroutine.

Lee *et al.* [9] developed a crystal plasticity constitutive model for BCC single

crystals taking into account the twinning-antitwinning asymmetry [10, 11] which is described in Section 2.3. The formulation was based on the previous work by Peirce *et al.* [6], and they employed a different hardening matrix for modeling the latent hardening behavior. They applied the BCC single crystal constitutive model to investigate the behavior of polycrystalline tungsten by means of an averaging scheme [12].

6.2 FEM Formulation for Simulating Plate Impact Experiments

In this section, FEM formulation in the present work is described in detail. First, central difference integration scheme used in Abaqus Explicit is presented. Then, the reminder of this section describes the crystal plasticity model implemented using VUMAT subroutine. For the quantities described in this section, the superscripts in parenthesis correspond to the time step.

Framework in Abaqus Explicit

The material that is presented in this subsection is based on the Abaqus 2016 Documentation [1]. In Abaqus Explicit, the explicit integration scheme is used together with lumped element mass matrices. The equations of motion for the continuum body are integrated using the central difference integration scheme:

$$\dot{\boldsymbol{u}}^{(n+\frac{1}{2})} = \dot{\boldsymbol{u}}^{(n-\frac{1}{2})} + \Delta t \ddot{\boldsymbol{u}}^{(n)} \tag{6.1}$$

$$\boldsymbol{u}^{(n+1)} = \boldsymbol{u}^{(n)} + \Delta t \dot{\boldsymbol{u}}^{(n+\frac{1}{2})} \tag{6.2}$$

where $\boldsymbol{u}$ is displacement and the dot represents the time derivative. The time increment Δt was kept constant in the present simulations. The acceleration at each time step is calculated from,

$$\ddot{\boldsymbol{u}}^{(n)} = \mathbf{M}^{-1}(\tilde{\boldsymbol{F}}^{(n)} - \tilde{\boldsymbol{I}}^{(n)}) \tag{6.3}$$

where $\mathbf{M}$ is the lumped (diagonal) mass matrix, $\tilde{\boldsymbol{F}}$ and $\tilde{\boldsymbol{I}}$ are the external and the internal force vector, respectively. Since $\mathbf{M}$ is diagonal, the update of the acceleration is computationally efficient.

In the central difference integration scheme, the initial condition needs extra care since $\dot{\boldsymbol{u}}^{(-\frac{1}{2})}$ appears in Eq. 6.1 when $n = 0$ and is defined as,

$$\dot{\boldsymbol{u}}^{(-\frac{1}{2})} = \dot{\boldsymbol{u}}^{(0)} - \frac{\Delta t}{2}\ddot{\boldsymbol{u}}^{(0)}. \tag{6.4}$$

In Abaqus Explicit, the initial velocity and acceleration are set to zero unless otherwise specified by the boundary conditions.

Unlike the implicit integration scheme, the explicit integration scheme is conditionally stable. The stability condition is given by

$$\Delta t \leq \frac{2}{\omega_{\max}} \tag{6.5}$$

where $\omega_{\max}$ is the largest eigenvalue of the system, which is approximated by

$$\Delta t \leq \frac{2}{\omega_{\max}} \cong \frac{l}{v} \tag{6.6}$$

where l is the characteristic length of an element and v is the characteristic wave speed.

In each time step of a simulation (n-th time step), the following quantities are passed onto the material model.

$$\boldsymbol{\sigma}^{(n-1)}, \Delta\boldsymbol{\epsilon}^{(n-1)}, \mathbf{F}^{(n-1)}, \mathbf{F}^{(n)}$$

where $\mathbf{F}$ represents the deformation gradient tensor, and $\boldsymbol{\epsilon}$ is the strain tensor at each time step. Based on those quantities, the material model returns the stress tensor $\boldsymbol{\sigma}^{(n)}$ which is then used to calculate the internal force vector $\tilde{\boldsymbol{I}}^{(n)}$ in Eq. 6.3.

Crystal Plasticity Model

In the FEM simulation of the present work, a crystal plasticity model [9] was implemented using the VUMAT subroutine as the material model. The VUMAT implementation is described below. The main assumptions in the crystal plasticity model are the following.

- The plastic deformation is governed by motion of dislocation slip.
- The plastic deformation does not affect the elastic constants.

The second assumption is reasonable because the resulting crystal following the dislocation slip is identical to the undeformed crystal, even though individual atoms are displaced. This is schematically shown in the Fig. 6.1.

Each slip system was defined by its Burgers vector (direction of slip) $\hat{\boldsymbol{b}}$ and the normal to the slip plane $\hat{\boldsymbol{n}}$. The deformation of Mo single crystals are governed by two slip systems: {110}<111> and {112}<111>. These are shown schematically in Fig. 6.2. There are 12 independent slip systems for each type, therefore 24 slip systems were considered in the FEM simulation. The slip systems are summarized

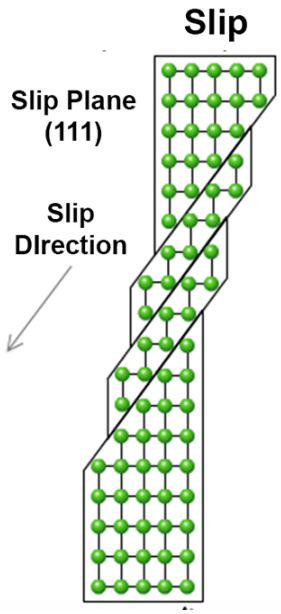

Figure 6.1: Schematic of slip in a crystal. (From [13])

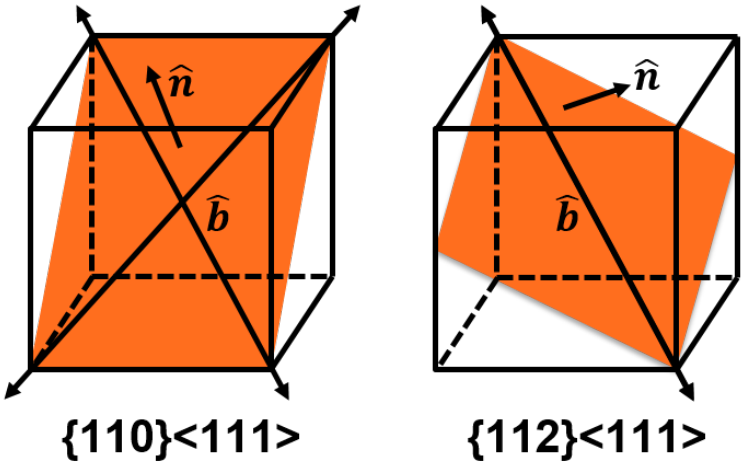

Figure 6.2: Slip systems considered in the FEM simulations. $\hat{\boldsymbol{b}}$ is the Burgers vector and $\hat{\boldsymbol{n}}$ is the plane normal.

Table 6.1: Slip systems considered in the FEM simulations

Index (k)	$\hat{\boldsymbol{n}}$	$\hat{\boldsymbol{b}}$	Index (k)	$\hat{\boldsymbol{n}}$	$\hat{\boldsymbol{b}}$
1	$\{0\bar{1}1\}$	<111>	13	$\{011\}$	$<\bar{1}\bar{1}1>$
2	$\{1\bar{2}1\}$	<111>	14	$\{\bar{1}21\}$	$<\bar{1}\bar{1}1>$
3	$\{1\bar{1}0\}$	<111>	15	$\{\bar{1}10\}$	$<\bar{1}\bar{1}1>$
4	$\{\bar{2}11\}$	<111>	16	$\{2\bar{1}1\}$	$<\bar{1}\bar{1}1>$
5	$\{10\bar{1}\}$	<111>	17	$\{\bar{1}0\bar{1}\}$	$<\bar{1}\bar{1}1>$
6	$\{11\bar{2}\}$	<111>	18	$\{\bar{1}\bar{1}\bar{2}\}$	$<\bar{1}\bar{1}1>$
7	$\{01\bar{1}\}$	$<\bar{1}11>$	19	$\{0\bar{1}\bar{1}\}$	$<1\bar{1}1>$
8	$\{\bar{1}1\bar{2}\}$	$<\bar{1}11>$	20	$\{1\bar{1}\bar{2}\}$	$<1\bar{1}1>$
9	$\{\bar{1}0\bar{1}\}$	$<\bar{1}11>$	21	$\{10\bar{1}\}$	$<1\bar{1}1>$
10	$\{211\}$	$<\bar{1}11>$	22	$\{\bar{2}\bar{1}1\}$	$<1\bar{1}1>$
11	$\{\bar{1}\bar{1}0\}$	$<\bar{1}11>$	23	$\{110\}$	$<1\bar{1}1>$
12	$\{\bar{1}\bar{2}1\}$	$<\bar{1}11>$	24	$\{121\}$	$<1\bar{1}1>$

in Table 6.1. We note that {112}<111> slip systems were defined such that positive value of shear strain corresponds to slip in the antitwinning sense.

When the Cauchy stress tensor $\boldsymbol{\sigma}$ is given, the resolved shear stress (RSS) on the k-th slip system is calculated using vectors in Table 6.1.

$$\tau = \hat{\boldsymbol{n}}_k \cdot \boldsymbol{\sigma} \hat{\boldsymbol{b}}_k \text{ (No sum on } k) \tag{6.7}$$

This is analogous to calculating the Schmid factor [8] in the case of uniaxial stress.

Figure 6.3 illustrates the incremental kinematic formulation. The deformation tensors $\mathbf{F}^{n-1}$ and $\mathbf{F}^n$ correspond to the beginning and the end of each (n-th) time step, respectively. In each time step, the single crystal deforms by the shear on slip systems, which gives rise to the plastic part of deformation gradient $\Delta\mathbf{F_p}$. Subsequently, the single crystal with embedded lattice undergoes elastic deformation which is represented by the elastic counterpart $\Delta\mathbf{F_e}$. We have that

$$\Delta\mathbf{F} = \Delta\mathbf{F_e}\Delta\mathbf{F_p} \tag{6.8}$$

which is analogous the multiplicative decomposition of the deformation gradient tensor.

The following quantities are passed onto the VUMAT subroutine in each time step.

$$\boldsymbol{\sigma}^{(n-1)}, \Delta\boldsymbol{\epsilon}^{(n-1)}, \mathbf{F}^{(n-1)}, \mathbf{F}^{(n)}$$

In VUMAT subroutine, RSS on 24 slip systems $\tau_k^{(n-1)}$ are calculated by substituting $\boldsymbol{\sigma}^{(n-1)}$ into Eq. 6.7. Then, based on the flow rule f_{flow}, the shear velocity on each

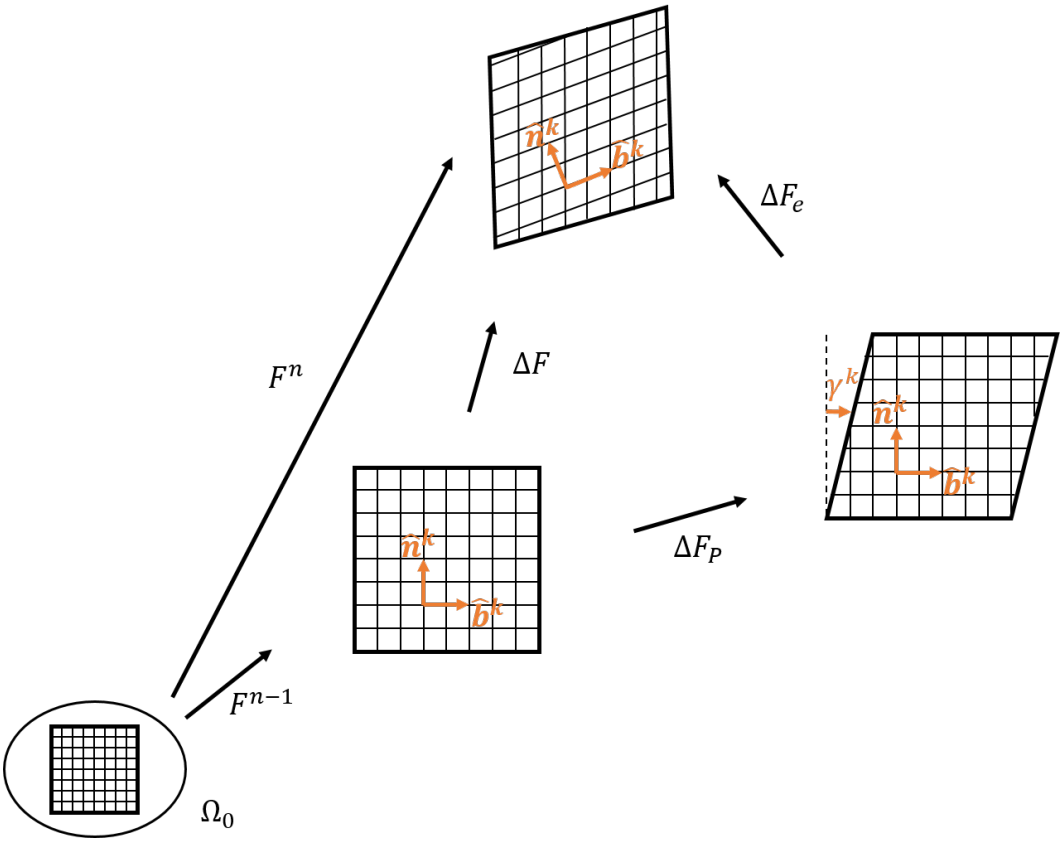

Figure 6.3: Incremental formulation in FEM simulation using Abaqus Explicit. Ω_0 corresponds to the undeformed configuration. Abaqus Explicit performs coordinate transformations after each step, and the tensorial quantities are defined in the coordinate corresponding to $\mathbf{F}^{n-1}$.

slip system $\dot{\gamma}_k^{(n-1)}$ is determined. The shear strain on each of the 24 slip systems γ_k is updated, and based on the hardening law f_{h}, the instantaneous value of the critical RSS $\tau_{c,k}$ is updated.

$$\dot{\gamma}_k^{(n-1)} = f_{\text{flow}}(\tau_k^{(n-1)}, \tau_{c,k}^{(n-1)}, \Phi) \tag{6.9}$$

$$\gamma_k^{(n)} = \gamma_k^{(n-1)} + \dot{\gamma}_k^{(n-1)} \Delta t \tag{6.10}$$

$$\tau_{c,k}^{(n)} = \tau_{c,k}^{(n-1)} + f_{\text{h}}(\gamma^{(n-1)}, \dot{\gamma}^{(n-1)}, \Phi)\Delta t. \tag{6.11}$$

In the equations above, Φ represents a set of other parameters. The flow rule and the hardening law are described in detail in subsequent sections. Temperature (T) is initially set to 300 K and updated using the following equation.

$$T^{(n)} = T^{(n-1)} + \frac{\beta \Delta t}{\rho^{(n-1)} C_p} \sum_{k=1}^{24} |\tau_k^{(n-1)} \dot{\gamma}_k^{(n-1)}| \tag{6.12}$$

where β is a Taylor-Quinney constant which is the ratio of the plastic work converted to heat [9].

The shear strain, the critical RSS, and the instantaneous value of shear stress on each slip system, as well as the temperature are stored as internal variables at each material point. Based on the evolution of shear, the macroscopic tensorial quantities are updated as follows.

The plastic part of deformation tensor can be calculated using the shear strain γ_k, Burgers vector $\hat{\boldsymbol{b}}$, and the normal to the slip plane $\hat{\boldsymbol{n}}$ for the 24 slip systems.

$$\mathbf{F_p}^{(n)} = \sum_{k=1}^{24} \gamma_k^{(n)} \hat{\boldsymbol{b}}_k \otimes \hat{\boldsymbol{n}}_k. \tag{6.13}$$

Then, the elastic part of the Green strain tensor is given by

$$\mathbf{F_e}^{(n)} = \mathbf{F}^{(n)} (\mathbf{F_p}^{(n)})^{-1} \tag{6.14}$$

$$\mathbf{E_e}^{(n)} = \frac{1}{2}((\mathbf{F_e}^{(n)})^T \mathbf{F_e}^{(n)} - \mathbf{I}). \tag{6.15}$$

Rate of deformation tensor $\mathbf{D}$ and rate of spin tensor $\boldsymbol{\Omega}$ are decomposed into elastic and plastic parts.

$$\mathbf{D} = \mathbf{D_e} + \mathbf{D_p} \tag{6.16}$$

$$\boldsymbol{\Omega} = \boldsymbol{\Omega_e} + \boldsymbol{\Omega_p}. \tag{6.17}$$

The rate of deformation tensor $\mathbf{D}$ is given by

$$\mathbf{D}^{(n-1)} = \frac{1}{2\Delta t}(\mathbf{I} - (\mathbf{F}^{(n)})^{-T} (\mathbf{F}^{(n-1)})^T \mathbf{F}^{(n-1)} (\mathbf{F}^{(n)})^{-1}). \tag{6.18}$$

The plastic part of the rate of deformation tensor is calculated from

$$\mathbf{D_p}^{(n-1)} = \sum_{k=1}^{24} \frac{1}{2}(\hat{\boldsymbol{b}}_k \otimes \hat{\boldsymbol{n}}_k + \hat{\boldsymbol{n}}_k \otimes \hat{\boldsymbol{b}}_k) \dot{\gamma}_k^{(n-1)}. \tag{6.19}$$

Then, the corresponding elastic part $\mathbf{D_e}^{(n-1)}$ is calculated from Eqs. 6.16, 6.18, and 6.19. Similar to Eq. 6.19, the plastic part of the rate of spin tensor can be calculated from

$$\boldsymbol{\Omega_p}^{(n-1)} = \sum_{k=1}^{24} \frac{1}{2}(\hat{\boldsymbol{b}}_k \otimes \hat{\boldsymbol{n}}_k - \hat{\boldsymbol{n}}_k \otimes \hat{\boldsymbol{b}}_k) \dot{\gamma}_k^{(n-1)}. \tag{6.20}$$

The update of the stress is defined through Kirchhoff stress $\boldsymbol{\tau}$. In Abaqus Explicit, Green-Naghdi stress rate is used as the objective stress rates. However in the present

work, the Jaumann rate was used due to the ease of implementation. Since the rotation is not significant in our simulation, this does not affect our simulation.

Two Jaumann rates of Kirchhoff stress are defined: ${}^{\Delta}\boldsymbol{\tau}$ is based in the coordinate that rotates with the material and ${}^{\Delta e}\boldsymbol{\tau}$ is based in the coordinate that rotates with the embedded lattice (rotates with the elastic deformation $\Delta\mathbf{F}_e$). Then,

$$
\begin{aligned}
{}^{\Delta}\boldsymbol{\tau} &= \dot{\boldsymbol{\tau}} - \boldsymbol{\Omega}\boldsymbol{\tau} + \boldsymbol{\tau}\boldsymbol{\Omega} && (6.21)\\
{}^{\Delta e}\boldsymbol{\tau} &= \dot{\boldsymbol{\tau}} - \boldsymbol{\Omega}_{\mathbf{e}}\boldsymbol{\tau} + \boldsymbol{\tau}\boldsymbol{\Omega}_{\mathbf{e}}. && (6.22)
\end{aligned}
$$

One can relate the Jaumann rate to the kinematic variables using the constitutive relation.

$$
{}^{\Delta e}\boldsymbol{\tau} = \mathbb{C}(T) : \mathbf{D}_{\mathbf{e}} + \tilde{\mathbb{C}}(T) : \mathbf{E}_{\mathbf{e}} : \mathbf{D}_{\mathbf{e}}. \tag{6.23}
$$

In Eq. 6.23, second and third order elastic moduli are employed for the constitutive relation, and these moduli are temperature dependent. The temperature dependence of the elastic moduli is described in detail in the subsequent section. From the equations above,

$$
\begin{aligned}
{}^{\Delta}\boldsymbol{\tau} &= {}^{\Delta e}\dot{\boldsymbol{\tau}} + \boldsymbol{\Omega}_{\mathbf{e}}\boldsymbol{\tau} - \boldsymbol{\Omega}\boldsymbol{\tau} - \boldsymbol{\tau}\boldsymbol{\Omega}_{\mathbf{e}} + \boldsymbol{\tau}\boldsymbol{\Omega}\\
&= \mathbb{C}(T) : \mathbf{D}_{\mathbf{e}} + \tilde{\mathbb{C}}(T) : \mathbf{E}_{\mathbf{e}} : \mathbf{D}_{\mathbf{e}} - \boldsymbol{\Omega}_{\mathbf{p}}\boldsymbol{\tau} + \boldsymbol{\tau}\boldsymbol{\Omega}_{\mathbf{p}}. && (6.24)
\end{aligned}
$$

The stress tensor at next time step is calculated using Eq. 6.24.

$$
\boldsymbol{\sigma}^{(n)} = \frac{1}{\det\mathbf{F}^{(n)}}(\det\mathbf{F}^{(n-1)}\boldsymbol{\sigma}^{(n-1)} + {}^{\Delta}\boldsymbol{\tau}^{(n-1)}\Delta t). \tag{6.25}
$$

Flow rule

For the flow rule in Eq. 6.9, an exponential form was implemented in an ad hoc manner, which is shown below.

$$
\dot{\gamma}_k^{(n-1)} = f_{\text{flow}} = \begin{cases} \dot{\gamma}_0 \exp\left[\dfrac{\tau_k^{(n-1)}}{\tau_{d,k}^{(n-1)}} - 1\right] & (\tau_k^{(n-1)} \geq \tau_{d,k}^{(n-1)}) \\ -\dot{\gamma}_0 \exp\left[\dfrac{\tau_k^{(n-1)}}{\tau_{d,k}^{(n-1)}} - 1\right] & (\tau_k^{(n-1)} \leq -\tau_{d,k}^{(n-1)}) \\ 0 & (\text{Otherwise}) \end{cases} \tag{6.26}
$$

where $\tau_{d,k}^{(n-1)}$ is the threshold for the activation of the slip, and was calculated taking into account the strain-rate dependent behavior. The exponential form for the flow rule was essential to simulate the rapid drop in particle velocity behind the elastic limit in plate impact experiments on Mo single crystals.

The threshold $\tau_{d,k}^{(n-1)}$ was defined based on the Cowper-Symonds (overstress power law) strain-hardening model. The Cowper-Symonds strain hardening law is usually defined as [1, 14, 15]

$$\frac{Y_{dynamic}}{Y_{static}} = 1 + \left(\frac{\dot{\epsilon}}{D}\right)^{\frac{1}{p}} \tag{6.27}$$

where p is the strain-rate sensitivity. Based on Eq. 6.27, the following form in terms of the critical RSS was adopted,

$$\frac{\tau_{d,k}}{\tau_{c,k}} = 1 + \left(\frac{\dot{\epsilon}}{D}\right)^{\frac{1}{p}} \tag{6.28}$$

where $\tau_{c,k}$ is the critical RSS without the strain-rate effect which is updated using the hardening law described below.

The strain-rate sensitivity was chosen to be $p = 2$ based on the relation reported in Molinari *et al.* [16]. In their work, shock structure of a plastic shock wave in aluminum with stress up to 10 GPa was simulated. They calculated the Swegle and Grady power law exponent [17] as a function of the strain-rate sensitivity p, and showed that $p \approx 1.8$ corresponds to the power law exponent reported. Swegle and Grady [17] showed that the maximum strain rate $\dot{\epsilon}_{max}$ and the change in longitudinal stress $\Delta\sigma$ in the plastic shock wave were related by the following:

$$\dot{\epsilon}_{max} = a(\Delta\sigma)^4 \tag{6.29}$$

where a is a constant.

Hardening law

The following latent hardening model proposed by Lee *et al.* [9] was employed in the simulations.

$$f_h = \sum_{l=1}^{24} h_{kl} \left|\dot{\gamma}_l^{(n-1)}\right| \tag{6.30}$$

$$h_{kl} = h_k^i \operatorname{sech}\left(\frac{h_k^i \sum_{m=1}^{24} |\gamma_m^{n-1}|}{g_k^s - g_k^i}\right) Q_{kl} \tag{6.31}$$

where h_k^i is the hardening rate, and g_k^i and g_k^s are the initial and saturation yield stresses, respectively. The initial yield stress corresponds to the Peierls stress [18]. The subscript k corresponds to the index of a slip system. Q_{kl} is the hardening matrix which is provided in Lee *et al.* [9].

The effect from hardening turned out to be insignificant in simulating the behavior of shock compressed Mo single crystals, which is discussed further in Section 6.7.

Temperature dependence of elastic moduli

A temperature dependent constitutive model motivated by a formulation by Steinberg *et al.* [19] was employed in the simulations. In their work, a model for the shear modulus and yield strength applicable at high-strain rate $\dot{\epsilon} \geq 10^5$ s^{-1} was presented. They represented the shear modulus G as a function of strain, pressure, and temperature as follows:

$$G = G_0 \left[1 + \left(\frac{G'_p}{G_0} \right) \frac{P}{\eta^{1/3}} + \left(\frac{G'_T}{G_0} \right) (T - 300) \right] \tag{6.32}$$

where G_0 is the shear modulus in the reference state ($T = 300$ K, $P = 0, \epsilon = 0$), η is the compression ratio defined as the reference specific volume divided by the specific volume. G'_p and G'_T correspond to the derivatives of G with respect to pressure and temperature at the reference state.

Shear modulus G is only applicable to isotropic solid and hence, one cannot directly use Eq. 6.32 in the simulation for anisotropic single crystals. Instead, the following form which was inspired by Eq. 6.32 was used. Since the pressure dependence of the elastic limit was not significant in the simulations, a simplified form shown below was adapted.

$$\mathbb{C}_{ijkl}(T) = \mathbb{C}_{ijkl,0} - G'_T(T - 300) \tag{6.33}$$

$$\tilde{\mathbb{C}}_{ijklmn}(T) = \tilde{\mathbb{C}}_{ijklmn,0} + G'_T(T - 300). \tag{6.34}$$

The sign in front of the parameter G'_T was chosen so that the absolute value of the elastic constants decrease with increasing temperature. As shown in Table 2.2, the third order elastic constants of Mo have negative values. In our simulations, the parameter G'_T was fitted.

6.3 Simulation Settings

Figure 6.4 shows the configuration used in the simulation of Mo single crystal subjected to shock compression.

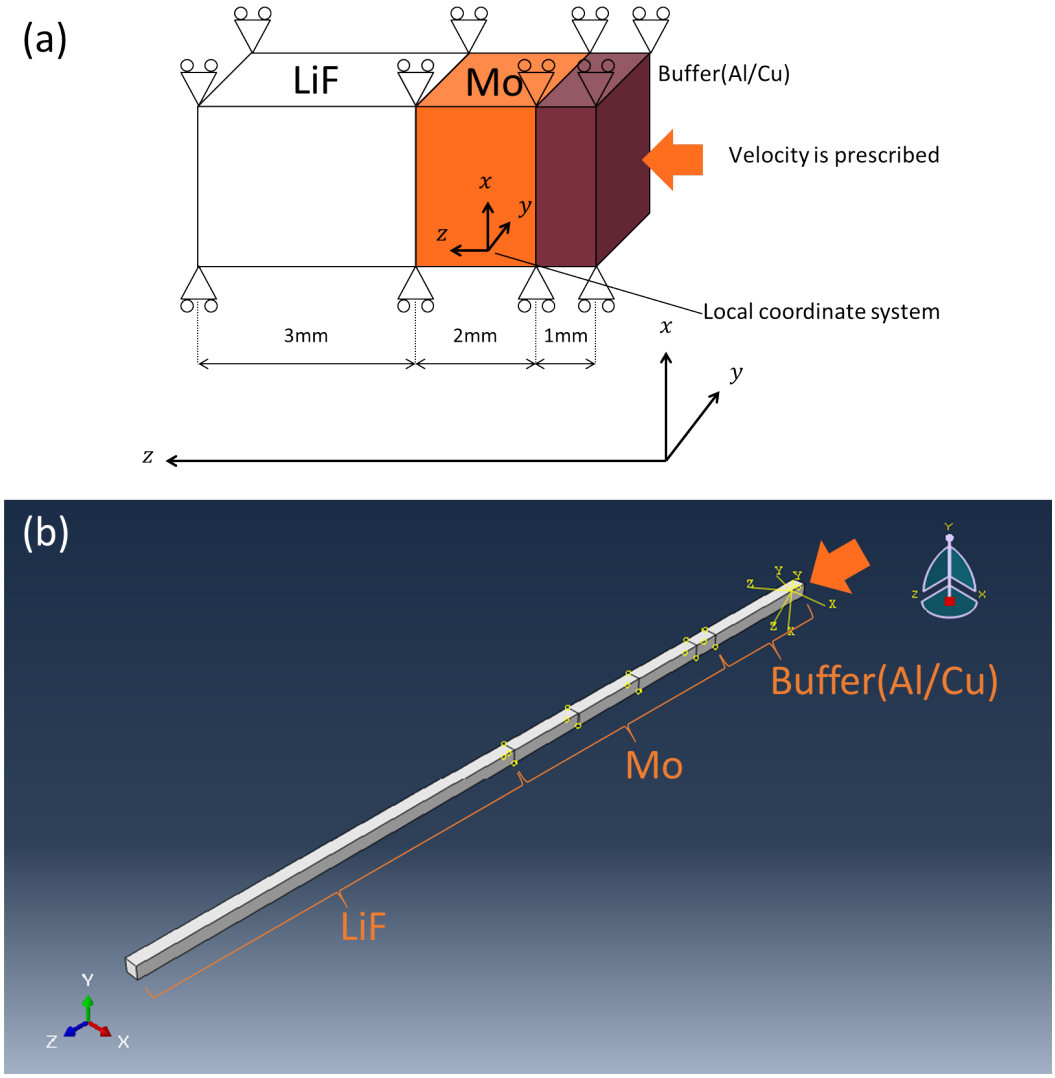

Figure 6.4: Simulation setting. (a)Schematic of the simulation domain and the boundary conditions. (b)A view in Abaqus Explicit. Orange arrow shows the end at which the velocity boundary condition was imposed.

As shown in Fig. 6.4, the boundary conditions for simulating uniaxial strain in the z-direction, which is the direction of shock propagation are the following.

- Four edges move only in z-direction. ($u_x = u_y = 0$)
- The surface $z = 0$ moves with a velocity corresponding to the half of the projectile velocity. The velocity was imposed as a smooth ramp function with rise time of 0.1 ns.

The boundary conditions reproduced the uniaxial strain condition in the plate impact experiment, until the edge wave arrives at the center of the Mo sample. Because of the 1-D deformation, the meshing was only applied along the longitudinal direction (z-direction). The sizes (thicknesses) of the mesh were 1 μm for Mo single crystal and 25 μm for the remainder of the simulation domain. The size of the time step was chosen to be $\Delta t = 10^{-12}$ s = 1 ps. The duration of the simulation was 6.5×10^{-7} s = 0.65 μs

The response of Al, Cu and LiF were input into Abaqus in the form of $U_s - u_p$ relations. These Hugoniot relations are shown in Table 4.1. Parameters appeared in the crystal plasticity model were either taken from previous works or fitted in order to match the resulting simulated velocity profile. These parameters are summarized in Table 6.2. The effect of twinning-antitwinning asymmetry [10, 11] was not considered in the setting shown in this section.

Table 6.2: Values of parameters for molybdenum single crystals used in the FEM simulations

Description		Value	Reference
Second order elastic constants	$\mathbb{C}_0$	Shown in Table 2.2	[20]
Third order elastic constants	$\tilde{\mathbb{C}}_0$	Shown in Table 2.2	[21]
Taylor-Quinney constant	β	0.9	[9]
Specific heat of Mo at 20 °C	C_p	0.276 J/(g · K)	[22]
Constant in the flow rule	$\dot{\gamma}_0$	$10^9 \mathrm{s}^{-1}$	Fitted
Constant in Cowper-Symonds strain hardening	D	$10^6 \mathrm{s}^{-1}$	Fitted
Strain rate sensitivity	p	2	[16]
For {110}<111> slip systems			
Hardening rate	h^i_k	1000 MPa	[9]
Initial yield stress	g^i_k	870 MPa	[18]
For {112}<111> slip systems			
Hardening rate	h^i_k	1000 MPa	[9]
Initial yield stress	g^i_k	690 MPa	[18]
Saturation yield stress[1]	g^s_k	$2g^i_k$	(Fitted)
Hardening matrix	$\mathbf{Q}$	Provided in Lee *et al.* [9]	
Constant in temperature dependence	G'_T	270 MPa/K	Fitted

[1]Saturation yield stress was initially set to $2g^i_k$. As discussed later in Section 6.4, the effect of hardening turned out to be insignificant. Thus, no further effort was made to adjust the value of the saturation yield stress.

In each FEM simulation, the velocity profile at Mo sample - Lif window interface was recorded at every time step. Also, the shear strain and the velocity profile inside Mo sample were recorded at 5 different locations. The distances from the front surface to the 5 locations are 1 μm, 0.2 mm, 0.8 mm, 1.4 mm, 2.0 mm (back surface), respectively.

Local coordinate system in Mo single crystal

In order to represent the Mo single crystal samples along [100], [111], and [110] orientations, the corresponding rotation matrices were calculated. Each row of the rotation matrix was input to Abaqus to define the local coordinate system.

As shown in Fig. 6.4, the global coordinate system was defined such that the direction of shock loading was in z-direction. For the simulation along the [110] orientation, the vector $\hat{\boldsymbol{e}}_z = [001]$ in the global coordinate should correspond to one of the vectors in [110] family in the local coordinate.

Let $\mathbf{R}$ be the rotation matrix. Then, for example,

$$\frac{1}{\sqrt{2}}\begin{bmatrix} 0 \\ 1 \\ -1 \end{bmatrix} = \mathbf{R}\begin{bmatrix} 0 \\ 0 \\ 1 \end{bmatrix}. \tag{6.35}$$

The corresponding rotation matrix is,

$$\mathbf{R} = \begin{bmatrix} 1 & 0 & 0 \\ 0 & \frac{1}{\sqrt{2}} & \frac{1}{\sqrt{2}} \\ 0 & \frac{1}{\sqrt{2}} & -\frac{1}{\sqrt{2}} \end{bmatrix}. \tag{6.36}$$

Each row of matrix $\mathbf{R}$ corresponds to each basis vector in the local coordinate. Then, $\frac{1}{\sqrt{2}}[01\bar{1}]$ in the local coordinate corresponds to $\hat{\boldsymbol{e}}_z = [001]$ in the global coordinate.

For simulation along [111] orientation, following the same argument above, the rotation matrix is,

$$\mathbf{R} = \begin{bmatrix} \frac{1}{\sqrt{6}} & -\frac{1}{\sqrt{2}} & \frac{1}{\sqrt{3}} \\ \frac{1}{\sqrt{6}} & \frac{1}{\sqrt{2}} & \frac{1}{\sqrt{3}} \\ -\frac{2}{\sqrt{6}} & 0 & \frac{1}{\sqrt{3}} \end{bmatrix}. \tag{6.37}$$

Then, $\frac{1}{\sqrt{3}}[111]$ in the local coordinate corresponds to $\hat{\boldsymbol{e}}_z = [001]$ in the global coordinate.

The implementation of the elastic part of the material model and the local coordinate systems in Mo single crystal were checked with a uniaxial tension test. A $5 \times 5 \times 50$

Table 6.3: Results of the uniaxial tension test simulations

Orientation	Longitudinal Stress [MPa]		Error
	Simulated	Theoretical Value	
[100]	760.5	762.1	0.20%
[111]	571.0	565.2	1.0%
[110]	602.3	604.2	0.30%

mm bar of Mo single crystal was defined together with local orientation, and the bar was subjected to extension of 0.1 mm. The theoretical value of the longitudinal stress was calculated based on the second order elastic constants, and was compared with the simulated value. The results are summarized in Table 6.3.

6.4 Effect of Hardening

Before moving onto the results of simulation along each orientation at 23 GPa and 67 GPa impact stresses, this section discusses the effect of hardening described in Section 6.2 on the simulated velocity profiles. The figures below compare the results of FEM simulations with hardening and without hardening. Each figure shows the result of 23 GPa and 67 GPa impact stress simulation along the [100] orientation, respectively.

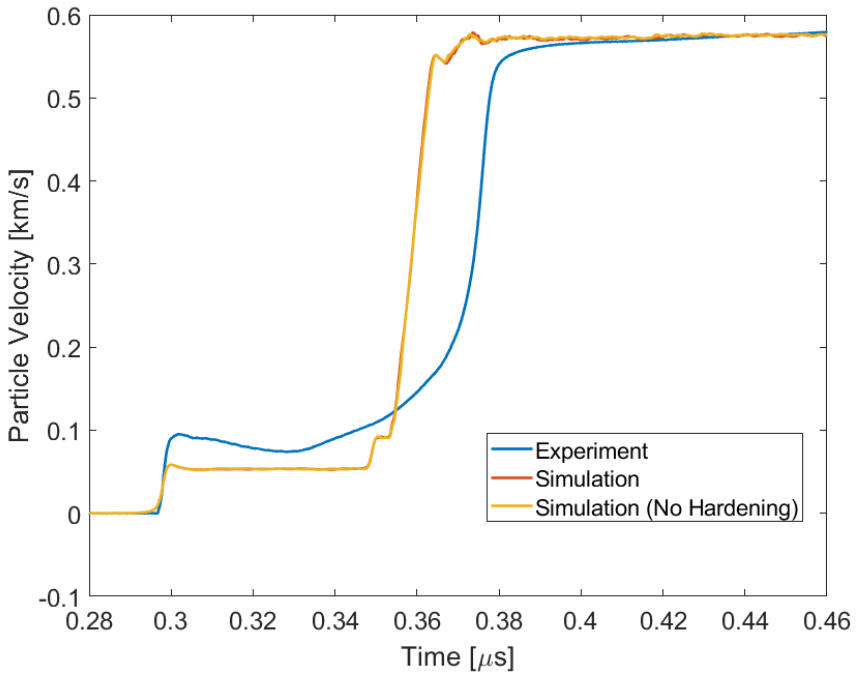

Figure 6.5: Effect of hardening on simulated velocity profile in 23 GPa impact stress simulation along [100] orientation.

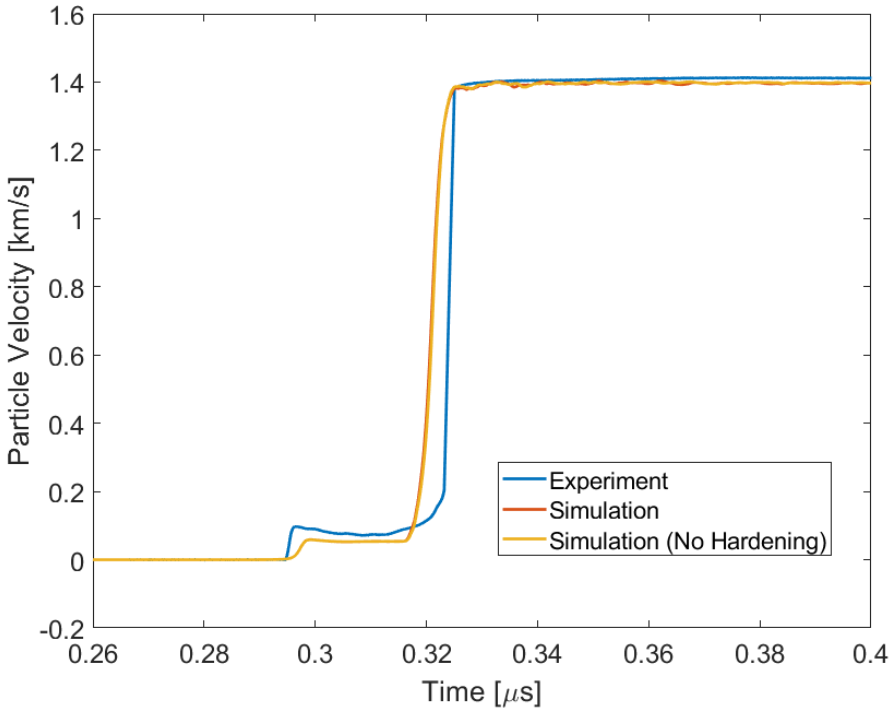

Figure 6.6: Effect of hardening on simulated velocity profile in 67 GPa impact stress simulation along [100] orientation.

In Figs. 6.5 and 6.6, the difference in the simulated velocity profiles were not significant when the hardening was considered.

Figures 6.7 and 6.8 compare the evolution of shear strain in those simulations. Shear strain at 5 locations in Mo single crystals are shown in those figures. One can see that the evolution of shear strain in those two simulations are almost identical and not affected by the level of hardening.

One can thus conclude that the effect of work hardening is not significant. In the remainder of this chapter, the work hardening described in Section 6.2 was not incorporated in the simulations.

6.5 Velocity Profiles

The results from the simulations are compared with the corresponding experiments in Figs. 6.9 - 6.11 for 23 GPa impact stress, and in Figs. 6.12 - 6.14 for 67 GPa impact stress. The effect of twinning-antitwinning asymmetry [10, 11] was not considered in the simulations in this section. In each figure, three plots are shown. The blue line corresponds to the experimental profile. The red line corresponds to

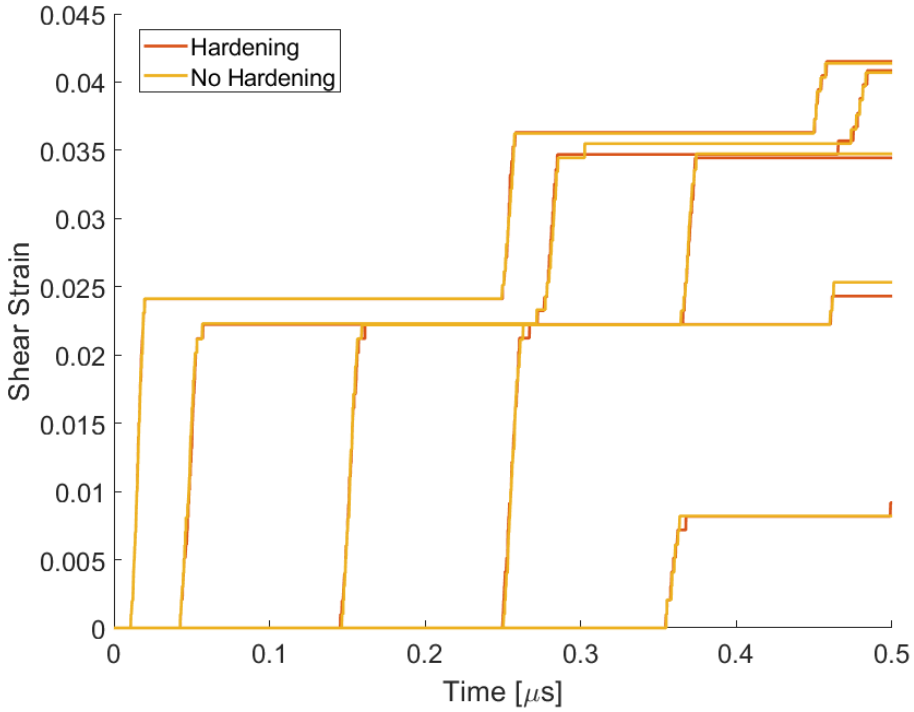

Figure 6.7: Effect of hardening on evolution of shear strain in 23 GPa impact stress simulation along [100] orientation.

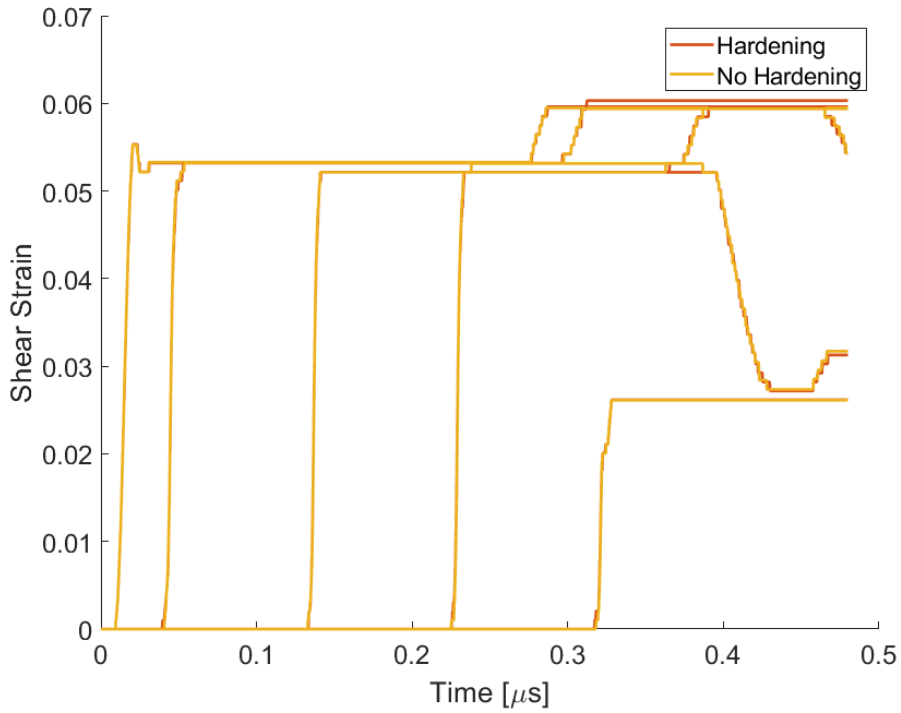

Figure 6.8: Effect of hardening on evolution of shear strain in 67 GPa impact stress simulation along [100] orientation.

the result of simulation where all of the 24 slip systems in Table 6.1 are considered. The yellow line corresponds to the result of simulation where only the {110}<111> slip systems are considered.

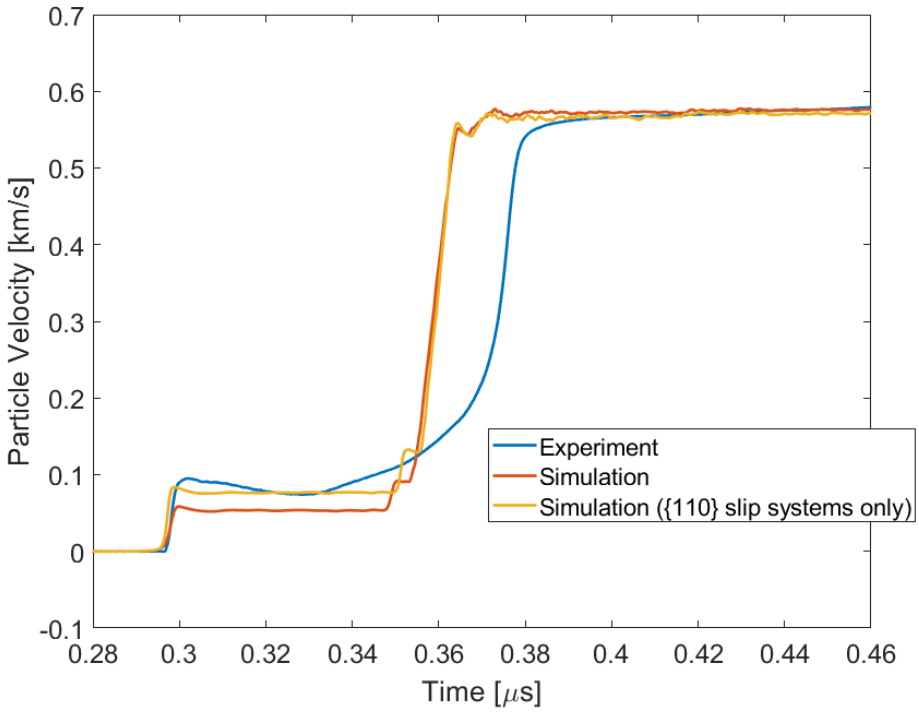

Figure 6.9: Simulated and experimental velocity profiles for 23 GPa impact stress along [100] orientation.

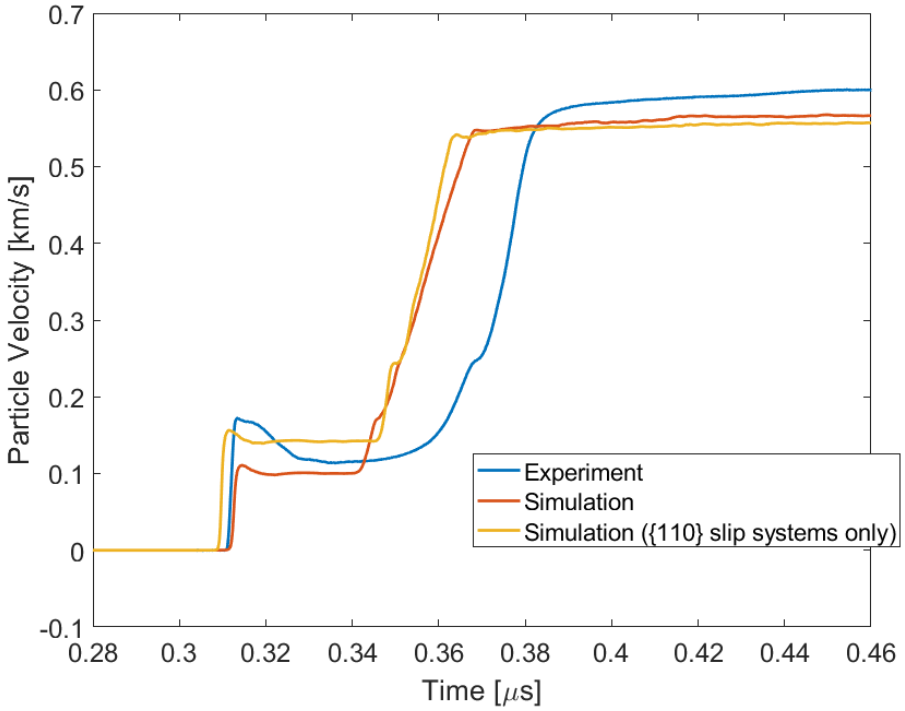

Figure 6.10: Simulated and experimental velocity profiles for 23 GPa impact stress along [111] orientation.

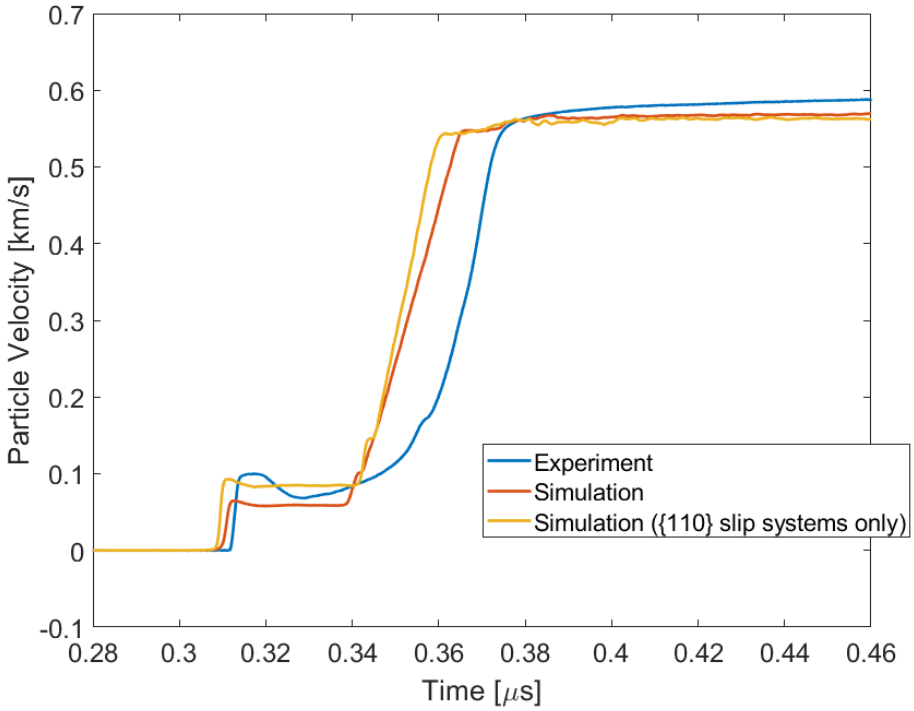

Figure 6.11: Simulated and experimental velocity profiles for 23 GPa impact stress along [110] orientation.

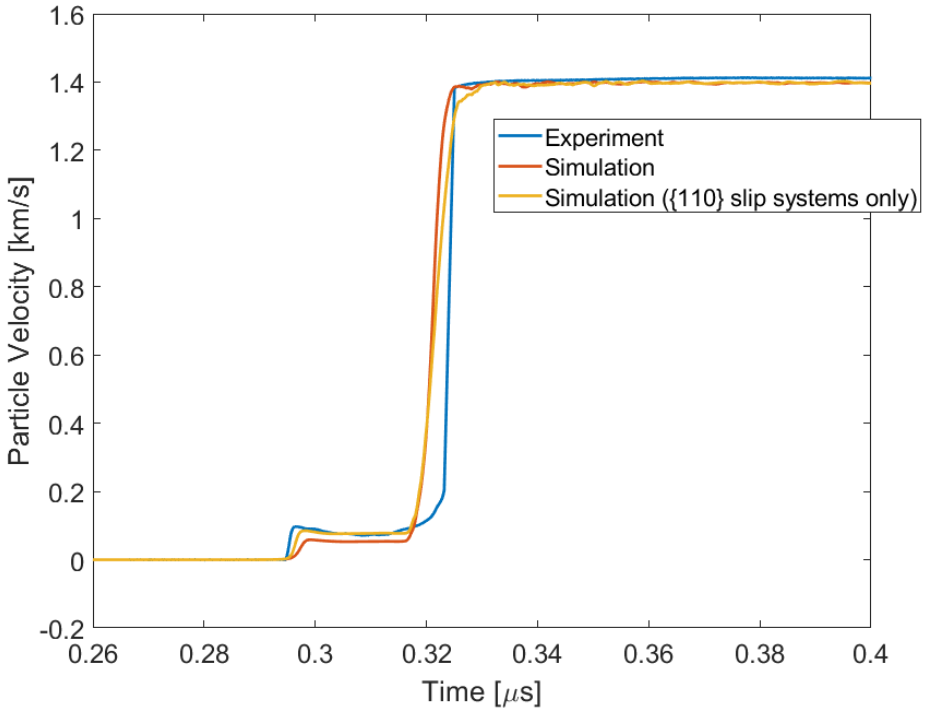

Figure 6.12: Simulated and experimental velocity profiles for 67 GPa impact stress along [100] orientation.

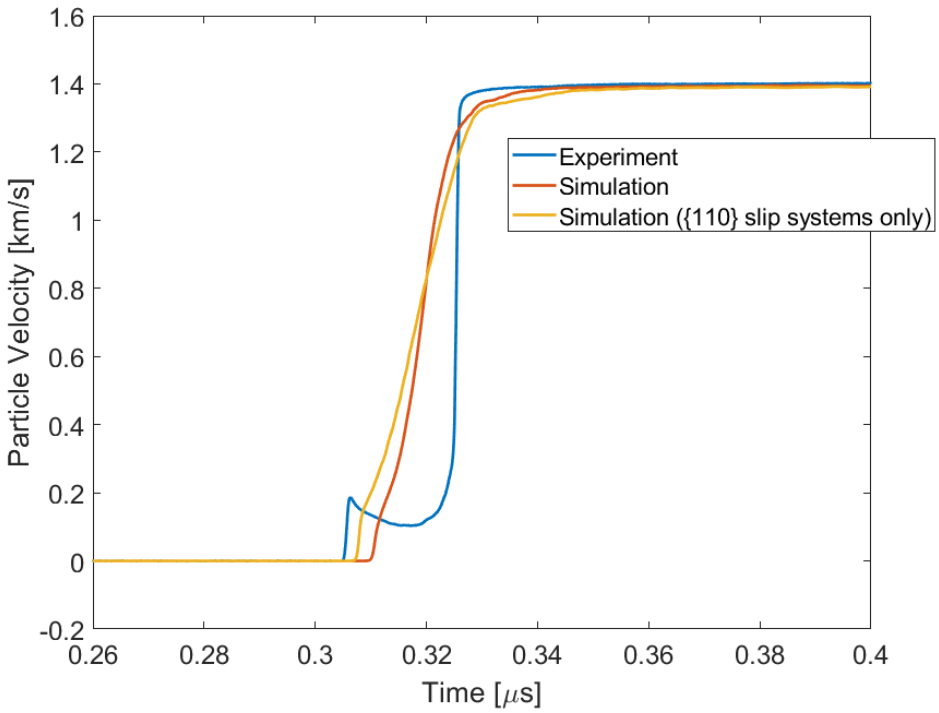

Figure 6.13: Simulated and experimental velocity profiles for 67 GPa impact stress along [111] orientation.

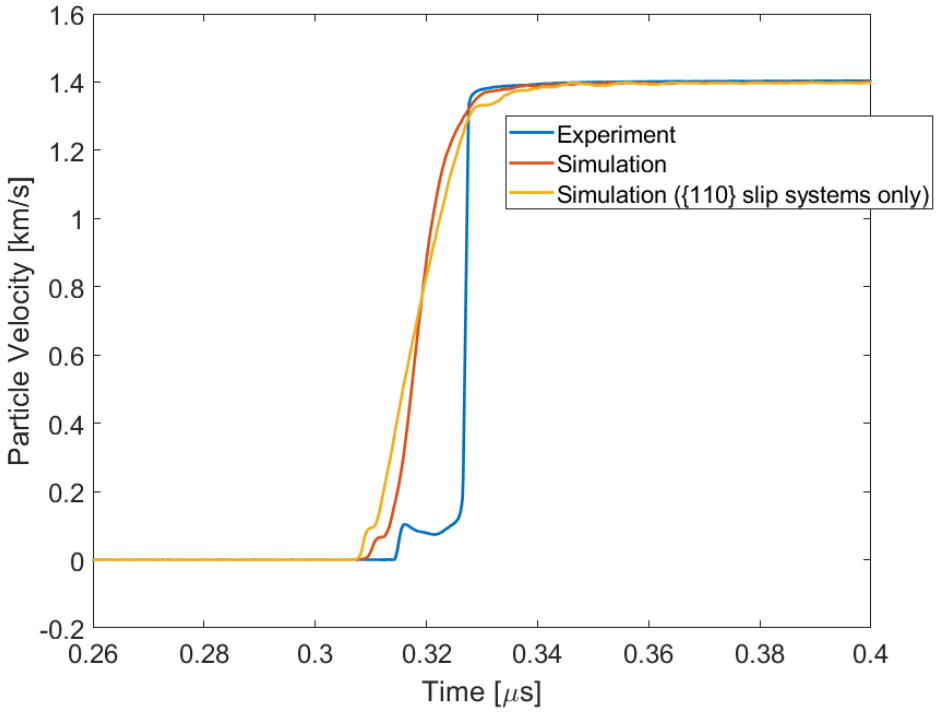

Figure 6.14: Simulated and experimental velocity profiles for 67 GPa impact stress along [110] orientation.

In Figs. 6.9 - 6.14, one can see that the plastic shock wave velocity was overestimated. In the 67 GPa impact stress simulation along [111] orientation (Fig. 6.13), the time separation between two shock waves was underestimated, and the elastic limit was not well-defined. In that case, the approach in Mandal *et al.* [23, 24] was used: the portions above and below the knee were fitted with separate straight lines, and the particle velocity at the intersection of those two fitted lines were taken as the elastic limit.

Even though the simulated velocity profiles exhibited relaxation behind the elastic limit, the velocity profile between the elastic shock wave and the plastic shock wave was not captured adequately. It is noted that, between two shock waves, a dip in the velocity was observed in the experiments. However, the simulated velocity profiles showed constant velocity after the relaxation immediately following the elastic shock wave, except for simulations along [110] and [111] orientations at 67 GPa impact stress.

In terms of the difference between two types of simulations, one can see that the behavior at the elastic limit (Mo sample - LiF window interface) was captured better

in the simulations by considering only the {110}<111> slip systems.

The shock velocities and the particle velocity at the elastic limit and the peak state are summarized in Table 6.4. This table also shows the measurement from the corresponding experiment for comparison.

Table 6.4 shows that the particle velocity at the elastic limit (measured or recorded at the Mo sample - LiF window interface) was captured better in the simulations with only {110}<111> slip systems. The error was within $\sim 10\%$ except for the 67 GPa impact simulation along the [111] orientation in which the elastic limit was not well defined. Anisotropy of the elastic limit in terms of the particle velocity - as mentioned in Chapter 4 - was adequately captured. The (Lagrangian) plastic shock velocity was overestimated at most by $\sim 4\%$.

Table 6.4: Simulated and experimentally measured shock velocities and particle velocities

Loading Direction	Nominal Impact Stress [GPa]		Elastic Limit		Peak State	
			Elastic Shock Velocity [km/s]	Particle Velocity [km/s]	Plastic Shock Velocity [km/s]	Particle Velocity [km/s]
[100]	23	Experiment A1	6.79±0.17	0.0954±0.001	5.38±0.11	0.588±0.006
		Simulation	6.76	0.0584	5.57	0.577
		Simulation {110}	6.76	0.0838	5.56	0.573
	67	Experiment A3	6.82±0.14	0.0975±0.001	6.20±0.12	1.41±0.02
		Simulation	6.76	0.0585	6.23	1.40
		Simulation {110}	6.78	0.0851	6.22	1.40
[111]	23	Experiment B1	6.52±0.15	0.172±0.002	5.39±0.10	0.602±0.007
		Simulation	6.41	0.111	5.61	0.568
		Simulation {110}	6.47	0.156	5.62	0.558
	67	Experiment B3	6.59±0.13	0.187±0.002	6.17±0.12	1.40±0.02
		Simulation	6.45	0.111	6.26	1.39
		Simulation {110}	6.51	0.136	6.27	1.39
[110]	23	Experiment C1	6.48±0.15	0.0999±0.001	5.51±0.11	0.592±0.006
		Simulation	6.45	0.0647	5.66	0.567
		Simulation {110}	6.47	0.0928	5.68	0.560
	67	Experiment C2	6.42±0.13	0.104±0.002	6.17±0.12	1.41±0.02
		Simulation	6.47	0.0660	6.27	1.40
		Simulation {110}	6.49	0.0940	6.27	1.40

Simulation: Results from FEM simulations with all 24 slip systems
Simulation {110}: Results from FEM simulations only with {110}<111> slip systems

6.6 Evolution of Shear Strain

The activated slip systems in the simulations depended on the loading orientation. Table 6.5 summarizes the activated slip systems in the simulations along each orientation. We note that the activated slip systems did not depend on the impact stress. In Table 6.5, slip systems which had the same amplitude of shear strain are put in parentheses. We note that the {110}<111> slip systems have odd indices and the {112}<111> slip systems have even indices as defined in Table 6.1.

Table 6.5: Activated slip systems in shock compressed molybdenum

Orientation	All slip systems are considered	Only with {110}<111> slip systems
[100]	{6,8,18,20(Antitwinning)}	{1,5,7,9,13,17,19,21}
[111]	{10,18,24(Twinning)}	{9,11,13,17,19,23}
[110]	{4,10(Twinning)}, {16,22(Antiwinning)}	{3,5,9,11},{15,17,21,23}

As shown in Table 6.5, the number of activated slip systems were multiples of 4,3, and 2 for simulations along [100], [111], and [110] orientations. This agrees with the symmetry that BCC single crystals have around those axes (shown in Table 2.1), which is reasonable.

Simulations with all 24 slip systems

The evolution of shear strain and the simulated velocity profile inside Mo sample recorded at 5 different locations are shown in Figs. 6.15 - 6.17 for the case of 23 GPa impact stress simulations where all 24 slip systems are considered. The simulated particle velocity is shown in blue line and the amplitude of shear strain is shown in orange and yellow.

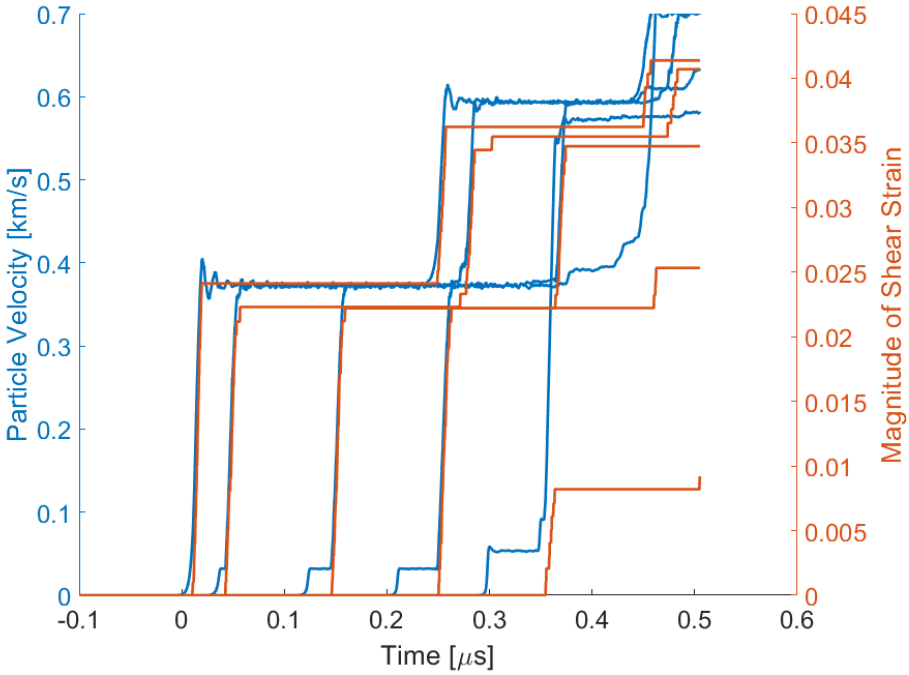

Figure 6.15: Evolution of shear strain and the particle velocity in Mo single crystal in 23 GPa impact simulation along [100] orientation.

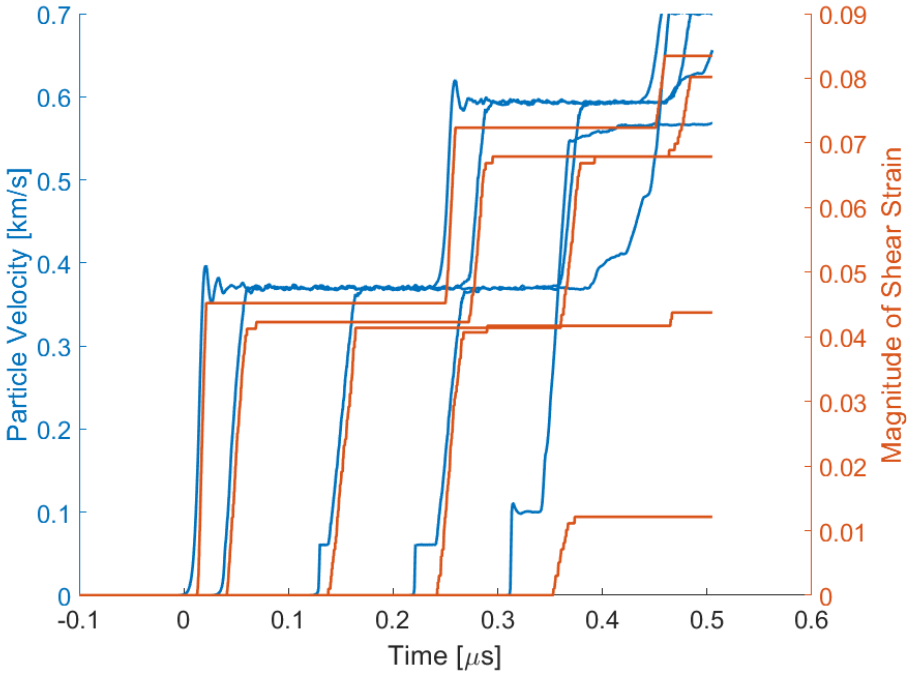

Figure 6.16: Evolution of shear strain and the particle velocity in Mo single crystal in 23 GPa impact simulation along [111] orientation.

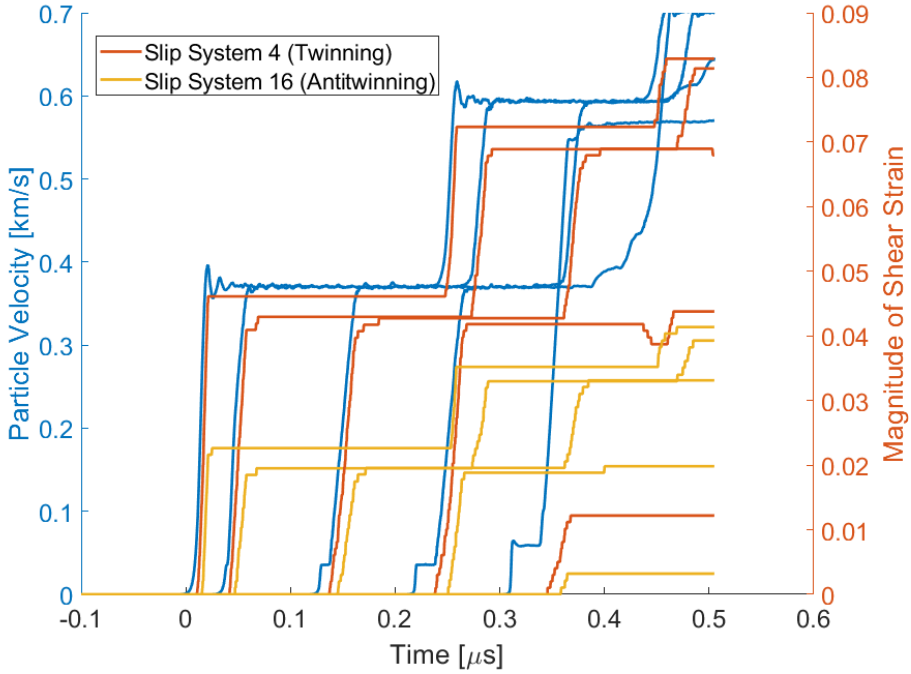

Figure 6.17: Evolution of shear strain and the particle velocity in Mo single crystal in 23 GPa impact simulation along [110] orientation.

Figures 6.15 - 6.17 show that the elastic limit inside Mo single crystals corresponds to the first activation of slip systems. For the left most set of plots in each figure (corresponding to 1 μm from the front surface), the time that the particle velocity reaches the elastic limit corresponds to the first increment of shear. That indicates that the plastic deformation is governed by the deformation on the slip systems. In each simulation along each orientation, the elastic wave propagates faster than the trailing plastic wave, and the time separation between two waves increases as the waves propagate into the Mo single crystal.

As seen in Table 6.5 and Fig. 6.17, in the simulation along the [110] orientation, the amplitudes of slip were different on the slip systems activated in the twinning sense and on the slip systems activated in the antitwinning sense. However, despite the difference in the amplitude of shear strain, the evolution of shear strain on the two sets of slip systems are similar. The time at which the shear strain reaches maximum on these systems are nearly identical. The difference in the time at which these slip systems are activated is attributed to the difference in the ratio of longitudinal stress and the shear strain (analogous to the Schmid factor [8]) calculated using Eq. 6.7 for those two groups of slip systems.

Simulations only with {110}<111> slip systems

Along the [100] and [111] orientations, in simulations where only {110}<111> slip systems were considered, the evolution of shear strain on {110}<111> slip systems was similar to that on {112}<111> slip systems shown in Figs. 6.15 and 6.16. Along the [110] orientation, the evolution of shear strain on slip systems {3,5,9,11} was similar to the evolution on slip systems {4,10} in Fig. 6.17. The evolution of shear strain on slip systems {15,17,21,23} was similar to the evolution on slip systems {16,22} in Fig. 6.17. For all of the cases, the amount of shear on {110}<111> slip systems were 47 to 55% of the corresponding {112}<111> slip systems.

6.7 Discussion

Activated slip systems

As shown in Figs. 6.9 - 6.14 and Table 6.4, the simulation with only the {110}<111> slip systems reproduced the behavior at the elastic limit well. When all of the slip systems were considered, {112}<111> slip systems were activated. The simulated elastic shock velocity was almost identical to the simulation above, but the simulated particle velocity at the elastic limit was only 59 - 65% of the experimental results. This implies that the {110}<111> slip systems were responsible for the deformation at the elastic limit. This is consistent with the results of the analysis in Section 5.3.

The view that the {110}<111> slip systems controls the deformation already implies that the effect of twinning-antitwinning asymmetry in {112}<111> slip systems is not important. However, another type of simulation was carried out to focus on the effect of twinning-antitwinning asymmetry in {112}<111> silp system.

Effect of twinning-antitwinning asymmetry

As shown in Table 6.5, in the simulations along the [100] and [111] orientations, the {112}<111> slip systems activated only either in twinning sense or antitwinning sense. In contrast, the {112}<111> slip systems activated both in twinning and antitwinning along [110] orientation. This result is consistent with what was reported by Mandal [24]. This implies that the twinning-antitwinning asymmetry is not important in the simulations along the [100] or [111] orientations. The twinning-antitwinning asymmetry potentially plays a role in the simulation along [110] orientation.

Another simulation explicitly incorporating twinning-antitwinning asymmetry was carried out. As mentioned in Section 2.3, Guiu [10] found that the ratio of critical RSS for the hard and soft {112}<111> systems was around 1.5. Hence, in this

simulation, the initial yield stress (Table 6.2) for the {112}<111> slip systems activated in antitwinning sense was set to 690 MPa $\times$ 1.5 = 1035 MPa.

The result of the simulation incorporating twinning-antitwinning asymmetry is compared with the simulation where all 24 slip systems are considered. The simulated velocity profiles are shown in Figs. 6.18 and 6.19.

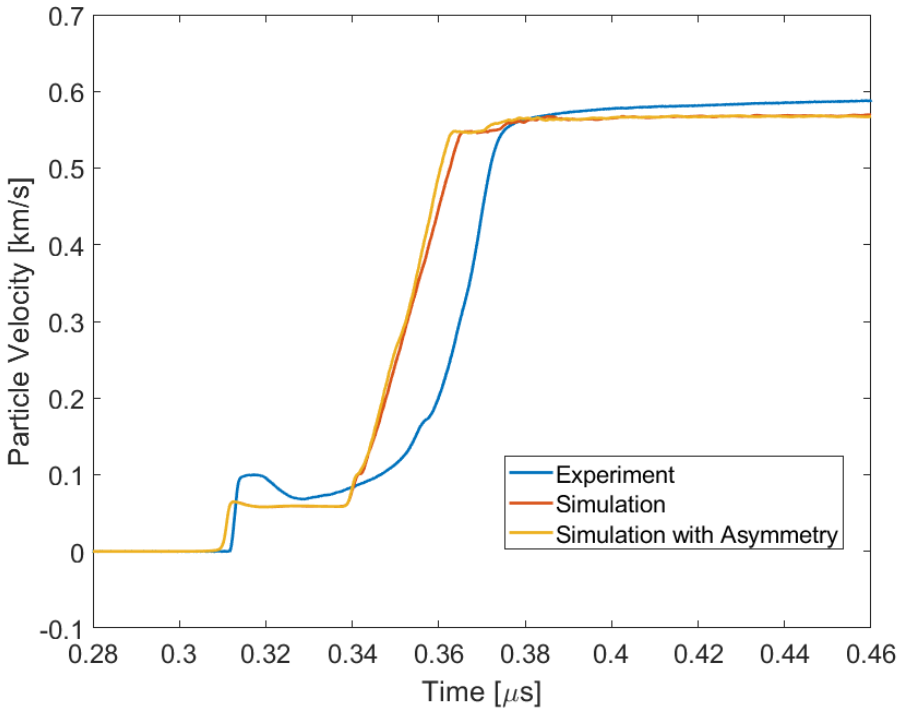

Figure 6.18: Effect of twinning-antitwinning symmetry in 23 GPa impact stress simulation along [110] orientation.

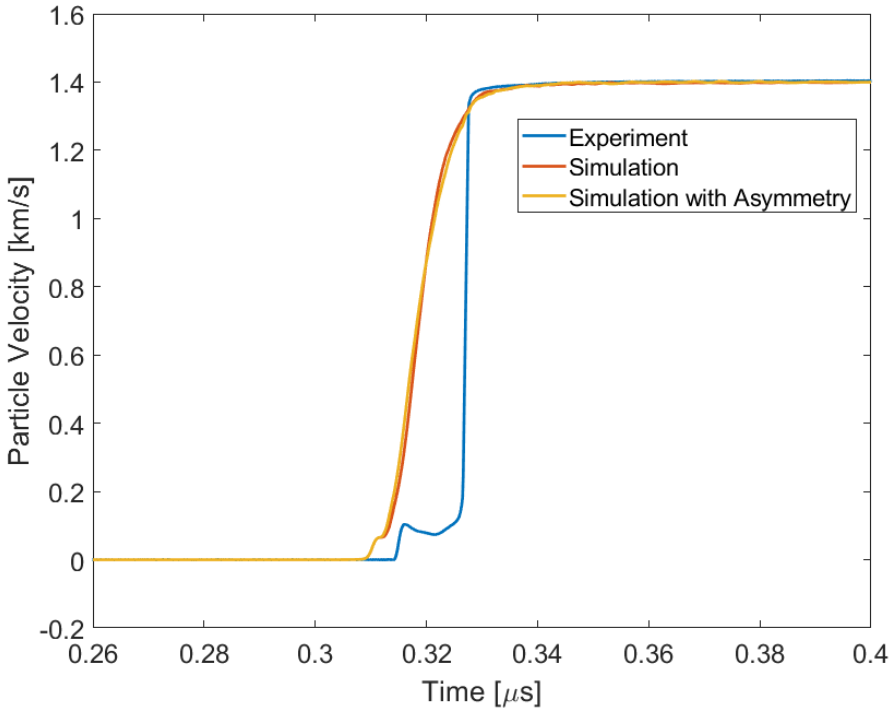

Figure 6.19: Effect of twinning-antitwinning symmetry in 67 GPa impact stress simulation along [110] orientation.

As shown in Figs. 6.18 and 6.19, the twinning-antitwinning symmetry had no effect on the simulated velocity profile until the elastic limit. There were slight differences in the simulated velocity profiles during the rise of the plastic shock wave, but the difference was not significant.

From this observation, one can conclude that the effect from the twinning-antitwinning symmetry is not significant in shock compressed Mo single crystals. As mentioned before, the simulated velocity profiles imply that the {110}<111> slip systems were responsible for the deformation at the elastic limit. This is consistent with the argument on the twinning-antitwinning symmetry.

Overestimation of plastic shock wave velocity

As mentioned in Section 6.5, the plastic shock velocity was overestimated in all of the simulations and are currently unable to explain the cause. Due to the overestimation of the plastic shock wave velocity, the time separation between elastic shock wave and plastic shock wave was underestimated. The elastic limit in 67 GPa impact simulation along the [111] orientation was not well-defined due to this effect. Also,

this hindered simulations where the impact stress was 90 GPa and higher. At those impact stresses, simulated velocity profile did not show the two-wave structure, and the overdriven shock wave was simulated by an error, due to the overestimation of plastic shock velocity. This effect requires further investigation.

Disagreement in the velocity profiles

The simulated velocity profiles did not capture the measured velocity profiles between elastic and plastic shock waves. This corresponds to the time when attenuation of the elastic shock wave occurs. The attenuation is controlled by interplay between the stress gradient and the plastic deformation rate behind the shock in addition to the material properties [25]. In our current model, the effect from the stress/strain gradient was not incorporated. The disagreement between the experiment and simulation may be attributed to the effect of stress/strain gradient.

6.8 Summary

A crystal plasticity model was implemented and simulations of shock compressed Mo single crystals were carried out. The significant findings from the numerical modeling are summarized below.

- The evolution of shear strain during the simulation supports that the elastic-plastic deformation is controlled by shear deformation on the slip plane.
- The error in the particle velocity at the elastic limit between the simulation and the experiment was smaller when considering only the {110}<111> slip systems in the simulation. This implies that the onset of plastic deformation of shock compressed Mo single crystals is governed by {110}<111> slip systems.
- Even when the effect of twinning-antitwinning was explicitly considered in the simulation, the effect was not significant.
- The plastic shock wave velocity was overestimated at most by $\sim 4\%$. However, this affects the simulation at higher impact stresses, which needs further investigation.
- The velocity profiles between elastic and plastic shock waves were not captured adequately. Dip in the particle velocity behind the elastic shock wave observed in experiments was not reproduced.

References

[1] Dassault Systemés. *Abaqus 2016 Documentation.* `ivt-abaqusdoc.ivt.ntnu.no:2080/v2016/`. [Online; accessed 2019 December 14].

[2] Dassault Systemés. *Abaqus User Subroutines Reference Guide.* `http://ivt-abaqusdoc.ivt.ntnu.no:2080/v2016/books/sub/default.htm`. [Online; accessed 2019 December 14].

[3] G. I. Taylor and C. F. Elam. "The distortion of iron crystals." In: *Proceedings of the Royal Society of London. Series A, Containing Papers of a Mathematical and Physical Character* 112.761 (1926), p. 337.

[4] G. I. Taylor. "Plastic strain in metals." In: *Journal of the Institute of Metals* 62 (1938), p. 307.

[5] R. Hill. "Generalized constitutive relations for incremental deformation of metal crystals by multislip." In: *Journal of the Mechanics and Physics of Solids* 14.2 (1966), p. 95.

[6] D. Peirce, R. J. Asaro, and A. Needleman. "An analysis of nonuniform and localized deformation in ductile single crystals." In: *Acta Metallurgica* 30.6 (1982), p. 1087.

[7] R. J. Asaro and J. R. Rice. "Strain localization in ductile single crystals." In: *Journal of the Mechanics and Physics of Solids* 25.5 (1977), p. 309.

[8] V. A. Lubarda. *Elastoplasticity Theory.* CRC press, 2001.

[9] Y. J. Lee, G. Subhash, and G. Ravichandran. "Constitutive modeling of textured body-centered-cubic (bcc) polycrystals." In: *International Journal of Plasticity* 15.6 (1999), p. 625.

[10] F. Guiu. "Slip asymmetry in molybdenum single crystals deformed in direct shear." In: *Scripta Metallurgica* 3.7 (1969), p. 449.

[11] V. Vítek. "Theory of the core structures of dislocations in body-centered-cubic metals." In: *Crystal Lattice Defects* 5 (1974), p. 1.

[12] R. Hill. "On constitutive macro-variables for heterogeneous solids at finite strain." In: *Proceedings of the Royal Society of London. A. Mathematical and Physical Sciences* 326.1565 (1972), p. 131.

[13] N. K. Bourne. *Physics - Viewpoint: Unexpected Twins.* `physics.aps.org/articles/v9/19`. [Online; accessed 2019 December 24].

[14] X. Y. Su, T. X. Yu, and S. R. Reid. "Inertia-sensitive impact energy-absorbing structures part II: Effect of strain rate." In: *International Journal of Impact Engineering* 16.4 (1995), p. 673.

[15] D. Forni, B. Chiaia, and E. Cadoni. "Strain rate behaviour in tension of S355 steel: Base for progressive collapse analysis." In: *Engineering Structures* 119 (2016), p. 164.

[16] A. Molinari and G. Ravichandran. “Fundamental structure of steady plastic shock waves in metals.” In: *Journal of Applied Physics* 95.4 (2004), p. 1718.

[17] J. W. Swegle and D. E. Grady. “Shock viscosity and the prediction of shock wave rise times.” In: *Journal of Applied Physics* 58.2 (1985), p. 692.

[18] L. Hollang, D. Brunner, and A. Seeger. “Work hardening and flow stress of ultrapure molybdenum single crystals.” In: *Materials Science and Engineering: A* 319 (2001), p. 233.

[19] D. J. Steinberg, S. G. Cochran, and M. W. Guinan. “A constitutive model for metals applicable at high-strain rate.” In: *Journal of Applied Physics* 51.3 (1980), p. 1498.

[20] D. L. Davidson and F. R. Brotzen. “Elastic Constants of Molybdenum-Rich Rhenium Alloys in the Temperature Range -190 °C to +100 °C.” In: *Journal of Applied Physics* 39.12 (1968), p. 5768.

[21] F. F. Voronov, V. M. Prokhorov, E. L. Gromnitskaya, and G. G. Il’ina. “Second- and Third-Order Elasticity Moduli of a Molybdenum Single Crystal.” In: *Phys. Met. Metallogr.* 45.6 (1978), p. 123.

[22] ESPI Metals. *Molybdenum.* `https://www.espimetals.com/index.php/technical-data/108-Molybdenum`. [Online; accessed 2020 January 2].

[23] A. Mandal and Y. M. Gupta. “Elastic-plastic deformation of molybdenum single crystals shocked along [100].” In: *Journal of Applied Physics* 121.4 (2017), p. 045903.

[24] A. Mandal. “Elastic-Plastic Deformation of Molybdenum Single Crystals Shocked to 12.5 GPa.” PhD thesis. Washington State University, School of Mechanical and Materials Engineering, 2016.

[25] L. Davison. *Fundamentals of shock wave propagation in solids.* Springer Science & Business Media, 2008.

Chapter 7

CONCLUSIONS AND FUTURE WORK

7.1 Summary

In the present work, the elastic-plastic deformation of Mo single crystals shock compressed to high stresses along three different orientations was investigated. Specifically, the objectives were to examine the role of deformation mechanisms and the effect of anisotropy on the elastic limit and the peak state. The present work has covered stresses that were significantly higher than the elastic limit, and examined the impact stress dependence manifested at the elastic limit and the peak state in the high stress range. These phenomena had not been considered in the previous shock studies on BCC single crystals. To achieve the overall objective, a combination of experiments and numerical simulations were conducted. For the experimental part, plate impact experiments were conducted to examine Mo single crystals under shock compression at varying impact stresses along [100], [111], and [110] orientations. For the numerical part, finite element method (FEM) simulations that directly accounts for shear strain on slip systems were performed.

In the plate impact experiments, the shock velocities and the velocity profile were measured using interferometry (VISAR [1, 2]). The experiments revealed clear anisotropic effects at the elastic limit in terms of the measured particle velocity. The measured particle velocity corresponding to the elastic limit at the Mo sample - LiF window interface was significantly higher along [111] orientation than the other orientations. Also, the effect of anisotropy manifested in the wave structure. A two-wave structure - an elastic shock wave trailed by a plastic shock wave - was observed up to 110 GPa impact stress along the [100] and [111] orientations. Along the [110] orientation, the two-wave structure was observed only up to 90 GPa impact stress. Along all three orientations, the measured particle velocity at the elastic limit increased with increasing impact stress. The dependence on the impact stress was significantly larger along the [111] orientation compared to the other orientations. In contrast to the elastic limit, the effect of anisotropy did not manifest at the peak state. The difference between the three orientations in terms of measured values at the peak state were within experimental uncertainties.

Based on the measured quantities, the in-material quantities at the elastic limit and

the peak state were calculated. Longitudinal stress at the elastic limit (elastic wave amplitude) increased with the elastic impact stress, and the elastic wave amplitude was larger along the [111] orientation than the other orientations. Compared to the shock studies at lower impact stresses by Mandal *et al.* [3–5], the elastic wave amplitudes showed an increase. In the elastic wave amplitude - elastic impact stress plot (Fig. 5.4), the results from their studies did not match well with the extrapolations from the present results. The difference was most pronounced for the [111] orientation. There is no satisfactory explanation for the rapid increase at present. To better understand the effect of anisotropy at the elastic limit and to gain insight into the slip systems governing elasic-plastic deformation in Mo single crystals, resolved shear stresses (RSS) on the {110}<111> slip systems and the {112}<111> slip systems were calculated based on the elastic wave amplitude. The difference between the calculated RSS and the corresponding Peierls stress [6] was smaller on the {110}<111> slip system. This suggested the activation of {110}<111> slip systems at the elastic limit.

At the peak state, Hugoniot relations were calculated based on the in-material quantities. The $U_s - u_p$ and the $P - v$ plots were compared between the three orientations as well as polycrystalline Mo [7]. In contrast to the anisotropic behavior at the elastic limit, the Hugoniot relations between three crystal orientations were within experimental uncertainties, and they agreed reasonably well with the Hugoniot relations for polycrystalline Mo [7]. The method to calculate the peak stress was analyzed, which showed that in the case of two-wave structures, the contribution from the elastic limit was considerably smaller than the contribution from the plastic shock velocity and the particle velocity at the peak state. The orientation-independence of the peak state was also observed in previous shock studies on Al single crystals [8] and Cu single crystals [9] (FCC structure) under high stresses.

In addition to the plate impact experiments, finite element method (FEM) simulations using Abaqus Explicit [10] were carried out. As the material model, a crystal plasticity model [11–14] was implemented using Abaqus VUMAT subroutine [15]. The results of simulations suggested that the effect of work hardening was not a significant factor in the behavior of shock compressed Mo single crystals. In the present work, two types of simulations were conducted: considering all of the {110}<111> and the {112}<111> slip systems, and considering only the {110}<111> slip systems. By comparing the results, the simulations suggested that the onset of plastic deformation at the elastic limit of shock compressed Mo single

crystals was governed by the {110}<111> slip systems. This was in agreement with the analysis of RSS in the present study.

Overall, the present study provided the first experimental measurements for Mo single crystals under shock compression to high stresses. The results on the impact stress dependence of the elastic wave amplitude of BCC single crystals were presented. Also, the peak state and the Hugoniot relations in BCC single crystals under a wide range of impact stress were discussed.

7.2 Future Work

Directions for future work are outlined below.

Jump in elastic wave amplitude

In Fig. 5.4, the linear fit was superposed onto the calculated elastic wave amplitudes along each orientation, but the results at the lower stress [3–5] did not match well with the extrapolations from the present results. The cause for this discrepancy was not determined from the present study. We note that the experimental configuration in the present work and the work by Mandal *et al.* [3–5] were different. The differences are summarized below.

- The experiments of Mandal *et al.* [3–5] used different materials for target components: 7075-aluminum projectile, α-axis sapphire buffer and c-axis sapphire window.
- Their plate impact experiments used a different facility. Since the projectile velocity was lower in their experiments, a 4 inch gas gun was used.

Hence, by making measurement with their experimental configuration at 23GPa impact stress, assuming c-sapphire window stays transparent at that stress, one can determine if there is an effect from the difference in the experimental configuration. Using the current configuration, one might encounter some issues as the shock wave propagating in Al buffer can be two-wave structure at lower stresses. If the difference in the experimental configuration does not affect the results, additional plate impact experiments in the range of 10 - 20 GPa might shed light on non-linear impact stress dependence of the elastic limit.

Sound speed measurement

In the present study, the peak state in Mo single crystals was found to be orientation-independent. However, as discussed in Section 5.8, this does not necessarily mean that the peak state is isotropic. As mentioned in Section 2.5, Choudhuri *et al.* [8] reported that the longitudinal sound speed in the shocked Al exhibited anisotropic behavior. This implies that the Al single crystal maintained the crystal structure under extreme compression. As a next step to the experimental efforts in shock compressed BCC single crystals, sound speed measurements in the peak state can elucidate the crystal structure, which is not reflected in the velocity profiles.

Microscopic measurement using X-rays

In this study, the difference between the calculated RSS at the elastic limit and the corresponding Peierls stress [6] suggested the activation of {110}<111> slip systems. The results from the FEM simulation agreed with this argument. Now that information on the continuum response from the macroscopic measurements are available, in-situ X-ray measurements as in the case of magnesium single crystals [16] can provide further information about the deformation mechanisms. Experiments on Mo might encounter difficulties in terms of the penetration distance of X-rays, but the microscopic information would be beneficial in validating a model to describe the shock induced elastic-plastic deformation.

Numerical Modeling

As mentioned in Section 6.7, the plastic shock velocity in Mo single crystals was overestimated in the FEM simulations. The cause was not determined at present, but the simulations at higher stresses were hindered by this phenomena. Since the third order elastic constants contribute to the plastic shock velocity, modifying the temperature dependence of these constants may improve the simulation capability. Regarding the disagreement in the velocity profiles between experiments and simulation, implementing the effect from the stress/strain gradient may help to reproduce the dip behind the elastic limit. Since there is only one material point in an element in the present simulation, stress gradient can be calculated by accessing multiple elements.

In addition to the verification of the crystal plasticity model with the uniaxial tension test, it will be advantageous to verify with other cases. For this purpose, data on the evolution of slip from the in-situ X-ray measurements can help in calibrating the material model. Also, by simulating one element subjected to compression under

uniaxial strain condition, one can compare simulated RSS and calculated value from the orientation of the loading and slip systems. Having an accurate model for the behavior in terms of crystal plasticity can contribute to the shock studies on a wide range of crystal structures due to its wide applicability.

References

[1] L. M. Barker and R. E. Hollenbach. "Laser interferometer for measuring high velocities of any reflecting surface." In: *Journal of Applied Physics* 43.11 (1972), p. 4669.

[2] L. M. Barker and K. W. Schuler. "Correction to the velocity-per-fringe relationship for the VISAR interferometer." In: *Journal of Applied Physics* 45.8 (1974), p. 3692.

[3] A. Mandal and Y. M. Gupta. "Elastic-plastic deformation of molybdenum single crystals shocked along [100]." In: *Journal of Applied Physics* 121.4 (2017), p. 045903.

[4] A. Mandal and Y. M. Gupta. "Elastic-plastic deformation of molybdenum single crystals shocked to 12.5 GPa: Crystal anisotropy effects." In: *Journal of Applied Physics* 125.5 (2019), p. 055903.

[5] A. Mandal. "Elastic-Plastic Deformation of Molybdenum Single Crystals Shocked to 12.5 GPa." PhD thesis. Washington State University, School of Mechanical and Materials Engineering, 2016.

[6] L. Hollang, D. Brunner, and A. Seeger. "Work hardening and flow stress of ultrapure molybdenum single crystals." In: *Materials Science and Engineering: A* 319 (2001), p. 233.

[7] R. S. Hixson and J. N. Fritz. "Shock compression of tungsten and molybdenum." In: *Journal of Applied Physics* 71.4 (1992), p. 1721.

[8] D. Choudhuri and Y. M. Gupta. "Shock compression of aluminum single crystals to 70 GPa: Role of crystalline anisotropy." In: *Journal of Applied Physics* 114.15 (2013), p. 153504.

[9] R. Chau, J. Stölken, P. Asoka-Kumar, M. Kumar, and N. C. Holmes. "Shock Hugoniot of single crystal copper." In: *Journal of Applied Physics* 107.2 (2010), p. 023506.

[10] Dassault Systemés. *Abaqus 2016 Documentation.* `ivt-abaqusdoc.ivt.ntnu.no:2080/v2016/`. [Online; accessed 2019 December 14].

[11] Y. J. Lee, G. Subhash, and G. Ravichandran. "Constitutive modeling of textured body-centered-cubic (bcc) polycrystals." In: *International Journal of Plasticity* 15.6 (1999), p. 625.

[12] R. J. Asaro and J. R. Rice. “Strain localization in ductile single crystals.” In: *Journal of the Mechanics and Physics of Solids* 25.5 (1977), p. 309.

[13] D. Peirce, R. J. Asaro, and A. Needleman. “An analysis of nonuniform and localized deformation in ductile single crystals.” In: *Acta Metallurgica* 30.6 (1982), p. 1087.

[14] V. A. Lubarda. *Elastoplasticity Theory.* CRC press, 2001.

[15] Dassault Systemés. *Abaqus User Subroutines Reference Guide.* `http://ivt-abaqusdoc.ivt.ntnu.no:2080/v2016/books/sub/default.htm`. [Online; accessed 2019 December 14].

[16] S. J. Turneaure, P. Renganathan, J. M. Winey, and Y. M. Gupta. “Twinning and dislocation evolution during shock compression and release of single crystals: real-time x-ray diffraction.” In: *Physical Review Letters* 120.26 (2018), p. 265503.

BIBLIOGRAPHY

[1] C. N. Reid. *Deformation geometry for materials scientists: international series on materials science and technology.* Vol. 11. Elsevier, 2016.

[2] Y. M. Gupta. *Wave Propagation Seminar (Physics 592) Lecture Notes.* Washington State University (2017).

[3] L. Davison. *Fundamentals of shock wave propagation in solids.* Springer Science & Business Media, 2008.